
Electronic Thesis and Dissertation Repository

11-8-2021 3:30 PM

Laser Desorption/Ionization Mass Spectrometry Imaging of Small Molecules and Neurotransmitters in Rodent Brains Assisted with Zinc Oxide Nanoparticles: Method Development and Applications in Neurobiology

Chaochao Chen, *The University of Western Ontario*

Supervisor: Ken Yeung, *The University of Western Ontario*

A thesis submitted in partial fulfillment of the requirements for the Doctor of Philosophy degree in Chemistry

© Chaochao Chen 2021

Follow this and additional works at: <https://ir.lib.uwo.ca/etd>

Recommended Citation

Chen, Chaochao, "Laser Desorption/Ionization Mass Spectrometry Imaging of Small Molecules and Neurotransmitters in Rodent Brains Assisted with Zinc Oxide Nanoparticles: Method Development and Applications in Neurobiology" (2021). *Electronic Thesis and Dissertation Repository*. 8242.
<https://ir.lib.uwo.ca/etd/8242>

This Dissertation/Thesis is brought to you for free and open access by Scholarship@Western. It has been accepted for inclusion in Electronic Thesis and Dissertation Repository by an authorized administrator of Scholarship@Western. For more information, please contact wlsadmin@uwo.ca.

Abstract

Mass spectrometry imaging (MSI) has emerged as a promising technique in providing small molecule compositions and two-dimensional or three-dimensional ion images showing the spatial distributions and relative abundances of small molecules in biological tissues. Among the ionization techniques compatible with MSI, matrix-assisted laser desorption ionization (MALDI) has been the most widely used ionization method. The careful selection of matrices in MALDI MSI allows the detection and imaging of specific compounds from complex biological samples. A major limitation to the detection of small molecules by MALDI-time-of-flight (TOF) MSI is the interference of matrix-derived peaks from commonly used organic matrices. Inorganic nanostructured materials such as silicon, carbon, metals, and metal oxides, have been explored as matrices to assist the laser desorption/ionization (LDI) mass spectrometry (MS) analysis of small molecules because of their low background signals, but their applications for imaging of small molecules in biological tissues remain limited.

In this thesis, the application of zinc oxide (ZnO) nanoparticles (NP) for LDI MS imaging of small molecules was investigated as a superior alternative to TiO₂ NP, one of the known NP that can effectively assist LDI MS imaging of small molecules. Compared to TiO₂ NP, ZnO NP have been found to deliver similar or better results in the imaging of small molecules in the rodent brain tissues. In addition, due to its dissolution in acidic pH, the regular acid washes in the automatic sprayer, which is used to deposit ZnO NP dispersion, were effective in minimizing clogging and maintaining fairly high reproducibility. Moreover, imaging of rodent brain tissues with superior spatial resolution was achieved.

MALDI MSI was next applied to visualize the distributions and analyze the relative abundances of γ -aminobutyric acid (GABA) and glutamate, the primary inhibitory and excitatory neurotransmitters in the central nervous system (CNS), in various well-defined brain regions between the drug-treated and vehicle-treated rats. The effects of two drugs, nicotine and Δ -9-tetrahydrocannabinol (Δ -9-THC), were studied separately on the neurotransmitter levels in the rat brains. Chronic exposure to nicotine and Δ -9-THC during adolescence respectively, has been found to modulate the total GABA and glutamate levels in multiple brain regions in the adolescent rat brains in the short term and in the adult rat brains in the long term differently. The results acquired by MALDI MSI provide us with a more direct comparison between the preclinical studies from animal models and clinical studies using magnetic resonance spectroscopy (MRS).

Keywords

MALDI, mass spectrometry imaging, MSI, inorganic matrix, ZnO nanoparticles, low molecular weight molecules, small molecules, metabolites, neurotransmitters, rodent brains, untargeted analysis, relative quantitation, neurotransmitter abundance, Δ -9-THC, nicotine, chronic exposure during adolescence, short-term effects, long-term effects.

Summary for Lay Audience

Molecular imaging techniques such as positron emission tomography (PET) and fluorescence imaging have been used to aid the clinical diagnosis of brain cancers for many years by reflecting the activities of patients' brains at molecular levels. However, these techniques require radioactive and fluorescent agents to target specific compounds in the brain. The use of mass spectrometry imaging (MSI) has emerged as a promising technique in providing the molecular compositions and localization information of multiple compounds in post-mortem tissues without needing to target specific compounds.

Zinc oxide (ZnO) nanoparticles (NP) assisted the detection and imaging of metabolites and small neurotransmitters in rodent brain tissues using laser desorption ionization (LDI) MSI. This method was then used to assess the drug effects on neurotransmitter abundances in rat brains following drug treatments. Two drugs, nicotine, the cause of compulsive tobacco smoking, and Δ -9-tetrahydrocannabinol (Δ -9-THC, THC), the primary psychoactive component of marijuana, were studied separately.

LDI MSI assisted with ZnO NP was applied to examine the localizations and levels of γ -aminobutyric acid (GABA) and glutamate, the main inhibitory and excitatory neurotransmitters in the central nervous system (CNS). Sub-regions of the prefrontal cortex (PFC), nucleus accumbens (NAc), and hippocampus (HPC), which are related to executive functioning, reward processing, and memory, respectively, were studied to answer the functions of the specific sub-regions. Chronic exposure to nicotine and Δ -9-THC during adolescence respectively, has been shown to alter the total GABA and glutamate levels in

multiple brain regions in both adolescent and adult rat brains, indicating chronic adolescent drug exposure affects both adolescent and adult rat brains differently. In addition, we are able to correlate some of the results from animal models to what has been found in clinical populations.

Co-Authorship Statement

Chapters 2 contains published materials in the following journal:

1. Chaochao Chen, Steven R. Laviolette, Shawn N. Whitehead, Justin B. Renaud, and Ken K.-C. Yeung. Imaging of Neurotransmitters and Small Molecules in Brain Tissues Using Laser Desorption/Ionization Mass Spectrometry Assisted with Zinc Oxide Nanoparticles. *Journal of the American Society for Mass Spectrometry* **2021**, 32 (4), 1065-1079.

All the data presented in the article was collected by the author. The author also prepared the first draft of the manuscript. Article 1 was edited by Dr. Ken K.-C. Yeung, proofread by Drs. Steven R. Laviolette, Shawn N. Whitehead, and Justin B. Renaud. The rodent brain retrieval protocols were provided by Drs. Steven R. Laviolette and Shawn N. Whitehead. LC-MS experiments were conducted by Dr. Justin B. Renaud for small molecule identification.

Acknowledgements

I would primarily like to express my gratitude to my supervisor, Dr. Ken Yeung, for his invaluable patience, support, and guidance over the past years. This work would not be possible without his insightful discussions and thoughtful advice. His encouragement and continuous suggestions have been instrumental in the completion of my thesis. I would also like to give a special thanks to Dr. Steven Laviolette, our research collaborator, for providing the opportunities for me to carry out neuroscience projects. Chapters 3 and 4 will not be in this thesis without those opportunities. Thanks also go to Dr. Shawn Whitehead for providing brain samples in Chapter 2 and all delightful discussions.

This work could not have been undertaken without the funding and facilities provided by Western University. I also appreciate the financial support received from Western University and my supervisor. I would like to express my appreciation to my thesis supervisor, Dr. Blacquiere Johanna, for her suggestions on the writing of my first-year report, my committee members, Dr. James Choy and Dr. Lars Konermann, for their time and feedback on my research progress. My appreciation also extends to my examiners, Dr. James Choy, Dr. Yolanda Hedberg, Dr. Demian Ifa, and Dr. Brad Urquhart.

A special thank you goes to Kristina Jurcic, who has been incredibly supportive and helpful with questions I brought to her relating to instrumentation. During my studies, I have always enjoyed talking through ideas and problems with her and learning from her. Her knowledge and advice has always been helpful, and many of our discussions have been critical along this journey.

I would like to thank several staffs and student colleagues. Dr. Marta De Felice and Mr. Roger Hudson have been incredibly passionate and fun collaborators to work with. They have always been patient and supportive, and willing to answer questions related to their electrophysiology and animal behaviour studies. Our exciting work together has made me even more passionate about neurobiology research. Thank you to Dr. Justin Renaud for running LC–MS samples, showing me statistical analysis, and all the suggestions on experimental designs. Thanks go to Michael Lam and Aseruchi Chindah for their help with the quantitation data analysis. Thank you also goes to Natasha DesRochers and Jacob Walsh for taking the time to walk me through the software for LC–MS data analysis.

Thanks also go to the past and present members of Yeung Group, especially Jasmine Wang, Hanadi Ibrahim, Megan Kelman, Aaron Harris, Shirley Fan, Tianyu Qi, Samantha Lynn Cousineau, and Juan Pablo Galindo Lazo. It has been extremely encouraging working in such a welcoming lab with a group of supportive and caring people. Thanks also go to the group members of Drs. Steve Laviolette and Shawn Whitehead, Tony Jung and Wendy Wang.

I owe a huge thank you to my friends at Western University, Shan, Mengnan, Jiatang, and Mi, and my friends in London, Leia, Joey, Mingtong, Siyu, Joshua, and John, for all the help and encouragement. A special thank you goes to Joshua and John for proofreading this thesis. Finally, I would like to express my appreciation to my parents, Guiqin Chen and Li Wang, and my brother, Chaohua Chen, for their unconditional love, encouragement, and support. This would not have been possible without you all.

Table of Contents

Abstract.....	ii
Summary for Lay Audience.....	iv
Co-Authorship Statement	vi
Acknowledgements	vii
List of Tables	xvi
List of Figures.....	xvii
List of Equations	xxi
List of Symbols and Abbreviations	xxii
List of Appendices.....	xxviii
Chapter 1: Introduction of Small Molecule Analysis by Mass Spectrometry.....	1
1.1 Overview of Small Molecules in the Brain.....	2
1.1.1 Metabolites in the Brain.....	2
1.1.2 Neurotransmitters in the Brain.....	3
1.2 Small Molecule Extraction Techniques from Brains.....	6
1.2.1 Liquid-liquid Extraction.....	6
1.2.2 Solid-phase Extraction	6
1.2.3 Microdialysis.....	7
1.2.4 Ultrafiltration	8
1.2.5 Solid-phase Microextraction.....	9
1.3 Small Molecule Analyses	10

1.3.1	Indirect Analyses of Neurotransmitters	10
1.3.1.1	Positron Emission Tomography.....	10
1.3.1.2	Autoradiography	11
1.3.1.3	Electrophysiology	11
1.3.2	Direct Analyses of Small Molecules.....	12
1.3.2.1	Nuclear Magnetic Resonance	13
1.3.2.2	Mass Spectrometry (MS).....	14
1.4	Ionization Techniques in Mass Spectrometry Imaging (MSI).....	16
1.4.1	Secondary Ion Mass Spectrometry	16
1.4.2	Desorption Electrospray Ionization	17
1.4.3	Laser Ablation Electrospray Ionization	18
1.4.4	Matrix-assisted Laser Desorption Ionization (MALDI).....	18
1.5	MALDI MSI	21
1.5.1	Tissue Preparations.....	21
1.5.2	Matrix Selection.....	23
1.5.3	Matrix Deposition.....	24
1.5.4	Spatial Resolution and Sensitivity	25
1.6	Mass Analyzers in MSI.....	27
1.6.1	Resolving Power and Mass Accuracy.....	27
1.6.2	Orbitrap Analyzer	28
1.6.3	Fourier-transform Ion Cyclotron Resonance Analyzer.....	30
1.6.4	Time-of-flight (TOF) Analyzer.....	32
1.6.4.1	Principles of TOF Analyzer.....	32

1.6.4.2	Applications of TOF Analyzer.....	34
1.7	MS Detector	36
1.8	Thesis Overview	37
1.9	References.....	39

Chapter 2: Imaging of Neurotransmitters and Small Molecules in Brain Tissues

Using Laser Desorption/Ionization Mass Spectrometry Assisted with ZnO

Nanoparticles.....	47
2.1	Introduction..... 48
2.2	Experimental Section..... 53
2.2.1	Chemicals and Supplies 53
2.2.2	Preparations of Solutions 53
2.2.3	Scanning Electron Microscope Visualization of Dried NP 55
2.2.4	Preparation of Brain Tissue Sections and Matrix Depositions 55
2.2.5	MALDI MS Analysis and Data Processing..... 56
2.2.6	Sample Preparations for Liquid Chromatography–Mass Spectrometry (LC–MS) 57
2.2.7	LC–MS Analysis and Data Processing..... 58
2.2.8	Metabolite Identification..... 59
2.3	Results and Discussion 60
2.3.1	Background Signals in ZnO NP-assisted LDI MS Analysis 60
2.3.2	Comparison for LMWM Analysis Using ZnO NP, TiO ₂ NP, DHB, and CHCA as Matrices 60
2.3.3	Quantitative Analysis in ZnO NP-assisted LDI MS..... 61

2.3.4	Stability of NP Dispersion Against Aggregation.....	62
2.3.5	ZnO NP-assisted LDI MSI for Investigation of Mouse and Rat Brain Tissues	66
2.3.6	Comparison for Imaging of LMWM in Mouse Brain Tissues Using ZnO NP and TiO ₂ NP.....	72
2.3.7	Comparison of NP-assisted LDI MSI with Other Imaging Studies.....	73
2.3.8	Effects of NP Aggregation on Spatial Resolutions.....	80
2.3.9	Repeatability of ZnO NP-assisted LDI MSI.....	83
2.3.10	Effect of Salts in ZnO NP-assisted LDI MSI.....	85
2.4	Conclusion	88
2.5	References.....	89

Chapter 3: Relative Quantitation of Neurotransmitters in Brains from Adolescent and Adult Rats Subjected to Chronic Adolescent Nicotine Exposure Using Laser Desorption/Ionization Mass Spectrometry Imaging Assisted with ZnO

Nanoparticles.....	96	
3.1	Introduction.....	97
3.2	Experimental Section.....	106
3.2.1	Chemicals and Supplies	106
3.2.2	Animals and housing.....	106
3.2.3	Drug Preparation and Administration.....	107
3.2.4	Sample Preparations for MSI.....	107
3.2.5	MALDI MSI Analysis and Data Processing.....	108
3.2.6	Statistical Analysis.....	110

3.2.7	Sample Preparations for LC–MS	110
3.2.8	LC–MS Analysis and Data Processing	111
3.3	Results and Discussion	113
3.3.1	Identification and Spatial Distribution of Neurotransmitters in the Rat Brain Sections	113
3.3.2	Relative Quantitation of Neurotransmitters between the Nicotine-treated and Vehicle-treated Rat Brains	119
3.3.2.1	Relative Quantitation of Neurotransmitters in the Brains from Adolescent Rats Subjected to Chronic Adolescent Nicotine Exposure	121
3.3.2.2	Relative Quantitation of Neurotransmitters in the Brains from Adult Rats Subjected to Chronic Adolescent Nicotine Exposure	127
3.3.2.3	Comparison of Relative Quantitation of Neurotransmitters in the Brains from Adolescent and Adult Rats Subjected to Chronic Adolescent Nicotine Exposure	131
3.3.3	Comparison with Literature	133
3.3.3.1	Clinical Studies	133
3.3.3.2	Preclinical Studies Using Animal Models	133
3.4	Conclusion	135
3.5	Reference	136

Chapter 4: Investigation of Effects of Chronic Adolescent Δ-9- Tetrahydrocannabinol Exposure on Neurotransmitter Abundance in Adolescent and Adult Rat Brains Using Laser Desorption/Ionization Mass Spectrometry Imaging Assisted with ZnO Nanoparticles	140
--	------------

4.1	Introduction.....	141
4.2	Experimental Section.....	148
4.2.1	Chemicals and Supplies.....	148
4.2.2	Animals and housing.....	148
4.2.3	Drug Preparation and Administration.....	149
4.2.4	Sample Preparations for MSI.....	149
4.2.5	MALDI MSI Analysis and Data Processing.....	150
4.2.6	Statistical Analysis.....	152
4.3	Results and Discussion.....	153
4.3.1	Identification and Spatial Distribution of Neurotransmitters in the Rat Brain Sections.....	153
4.3.2	Relative Quantitation of Neurotransmitters between the THC-treated and Vehicle-treated Rat Brains.....	157
4.3.3	Effects of Chronic Adolescent THC Exposure on the Neurotransmitter Abundance in the Adolescent Rat Brains.....	158
4.3.4	Effects of Chronic Adolescent THC Exposure on the Neurotransmitter Abundance in the Adult Rat Brains.....	162
4.3.5	Comparison of Effects of Chronic Adolescent THC Exposure in the Adolescent and Adult Rat Brains.....	166
4.3.6	Comparison with Literature.....	168
4.3.6.1	Clinical Studies.....	168
4.3.6.2	Preclinical Studies Using Animal Models.....	168
4.4	Conclusion.....	171

4.5	Reference	172
Chapter 5: Conclusions & Future Work		176
5.1	Conclusions and Future Work	177
5.2	References.....	181
Appendix I – Chapter 2 Supplementary		183
Appendix II – Copyright Permission		196
Curriculum Vitae		197

List of Tables

Table 2.1. Information of Ions with MW below 500 Da Detected in the Sagittal Sections of Mouse and Rat Brains with ZnO NP-assisted LDI MSI. 68

Table 2.2. List of Small Molecules Detected in Mouse Coronal Brain Sections in the Positive-ion Mode Using ZnO NP- and TiO₂ NP-assisted LDI MSI (Bregma -2.46mm; Paxinos and Watson Atlas). 74

Table 3.1. The Averaged Peak Area Ratios (Fold Changes) of [GABA + K]⁺ at *m/z* 142.03, [Glutamate + K]⁺ at *m/z* 186.02, and the Signal at *m/z* 192.04, Their 95% CIs, and P-values from the Student T-test in Various ROI between the Nicotine-treated and Vehicle-treated Adolescent Rat Brains (n = 10) Are Presented. The Fold Change ± 95% CI Is Bolded When It Is Significantly Different than 1. P-value Is Bolded When It Is Less Than 0.05. 124

Table 3.2. The Averaged Peak Area Ratios (Fold Changes) of [GABA + K]⁺ at *m/z* 142.03, [Glutamate + K]⁺ at *m/z* 186.02, and the Signal at *m/z* 192.04, Their 95% CIs, and P-values from the Student T-test in Various Brain ROI between the Nicotine-treated and Vehicle-treated Adult Rat Brains (n = 8, PrL, IL, NAcC, NAcSh, and DS; n = 7, VS) Are Presented. The Fold Change ± 95% CI Is Bolded When It Is Significantly Different than 1. P-value Is Bolded When It Is Less Than 0.05. 129

Table 4.1. The Averaged Peak Area Ratios (Fold Changes) of [GABA + K]⁺ at *m/z* 142.03, [Glutamate + K]⁺ at *m/z* 186.02, and the Signal at *m/z* 192.04, Their 95% CIs, and P-values from the Student T-test between the THC-treated and Vehicle-treated Adolescent Rat Brains in Various ROI (n = 10, PrL, IL, NAcC, and NAcSh; n = 6, DS and VS; n = 4, VTA and SN) Are Presented. The Fold Change ± 95% CI Is Bolded When It Is Significantly Different than 1. P-value Is Bolded When It Is Less Than 0.05. 161

Table 4.2. The Averaged Peak Area Ratios (Fold Changes) of [GABA + K]⁺ at *m/z* 142.03, [Glutamate + K]⁺ at *m/z* 186.02, and the Signal at *m/z* 192.04, Their 95% CIs, and P-values from the Student T-test between the THC-treated and Vehicle-treated Adult Rat Brains in Various ROI (n = 8) Are Presented. The Fold Change ± 95% CI Is Bolded When It Is Significantly Different than 1. P-value Is Bolded When It Is Less Than 0.05. 165

List of Figures

- Figure 1.1.** Schematic diagram shows the neurotransmission between the presynaptic and postsynaptic neurons. Figure created using BioRender (<https://biorender.com/>)..... 5
- Figure 1.2.** Major proposed models for MALDI ionization (A = analyte, M = matrix, X⁻ = counterion)..... 20
- Figure 1.3.** Overview of the sample preparation and analysis process for MALDI MSI. 22
- Figure 1.4.** Schematic diagram of Orbitrap mass analyzer..... 29
- Figure 1.5.** Schematic diagram of FT-ICR mass analyzer..... 31
- Figure 1.6.** Schematic diagram of (a) linear mode and (b) reflectron mode of MALDI TOF mass analyzer..... 35
- Figure 2.1.** Positive-ion mass spectra of a mixture of γ -aminobutyric acid (**GABA**, 75.0 ng; [M + H]⁺, *m/z* 104.07; [M + Na]⁺, *m/z* 126.05; [M + K]⁺, *m/z* 142.03), **myo-inositol** (37.5 ng; [M + H]⁺, *m/z* 181.07; [M + Na]⁺, *m/z* 203.05; [M + K]⁺, *m/z* 219.03), **spermine** (37.5 ng; [M + H]⁺, *m/z* 203.22; [M + Na]⁺, *m/z* 225.21; [M + K]⁺, *m/z* 241.19), **palmitic acid** (375 ng; [M + Na]⁺, *m/z* 279.23; [M + K]⁺, *m/z* 295.20), and **cholesterol** (375 ng; [M + Na]⁺, *m/z* 409.34; [M + K]⁺, *m/z* 425.32) with (a) ZnO NP, (b) TiO₂ NP, (c) DHB, and (d) CHCA in the mass region 120–500 on an ITO glass slide. 63
- Figure 2.2.** Calibration curve of GABA-d6 signals measured by ZnO NP-assisted LDI MS. Inlay shows the linear range of the calibration curve. The GABA-d6 concentration refers to that of the standard solution spiked on rat brain tissue sections. Error bars show +/- the standard deviation from 9 replicate measurements..... 64
- Figure 2.3.** SEM (scanning electron microscope) images of (A, B) ZnO and (C, D) TiO₂ NP, with different magnifications. Suspensions were prepared in 1:1 mixture of acetonitrile and water, deposited on silicon and dried in ambient conditions. 65
- Figure 2.4.** Ion images of the sagittal section of a mouse brain acquired with ZnO NP-assisted LDI MSI at a raster size of 70 μ m..... 70
- Figure 2.5.** Ion images of coronal sections of a rat brain acquired with ZnO NP-assisted LDI MSI (top to bottom: Bregma +3.00 mm, +2.04 mm, and -6.00 mm; Paxinos and Watson Atlas; raster size of 80 μ m)..... 71
- Figure 2.6.** Lists of molecules detected from a mouse brain with either TiO₂ or ZnO NP-assisted LDI MSI (AA, amino acids; NT, neurotransmitters; SL, sterol lipids; FA, fatty acids; OA, organic acids)..... 77

Figure 2.7. Averaged mass spectra from all pixels acquired on mouse coronal brain hemisphere sections with either (a) ZnO NP- or (b) TiO ₂ NP-assisted LDI MSI at a raster step size of 70 μm.	78
Figure 2.8. Ion images of mouse coronal brain hemisphere sections collected with ZnO NP or TiO ₂ NP at a raster step size of 70 μm.....	79
Figure 2.9. Ion images of the hippocampal region of a mouse brain acquired with ZnO NP-assisted LDI MSI at different raster step sizes.....	82
Figure 2.10. Average peak areas of signals at <i>m/z</i> 142.03, 186.02, 192.04, 219.03, and 409.34 with standard deviation error bars calculated using data obtained from (a) four adjacent tissue sections collected from the same rat brain on one slide as intra-slide replicates and (b) four adjacent tissue sections from the same rat brain on multiple slides and matrix deposited separately as inter-slide replicates. The relative standard deviations of replicates acquired are labeled on the corresponding bar graphs.	84
Figure 2.11. Peak height intensity ratios of the sodiated and potassiated ions from two adjacent mouse brain tissue sections without (control) and with the application of 5 mM potassium acetate (KOAc) (a) or 5 mM sodium acetate (NaOAc) (b) by automated sprayer. M represent the molecular weight. The figure inset shows the isotope patterns of [M + K] ⁺ at <i>m/z</i> 156.88 without and with the application of 5 mM potassium acetate.	87
Figure 3.1. A simplified diagram of the main connections to and from the PFC (prefrontal cortex), NAc (nucleus accumbens), basal forebrain, thalamus, dHPC (dorsal hippocampus), vHPC (ventral hippocampus), and VTA (ventral tegmental area), in a sagittal section of a rodent brain. GABAergic, glutamatergic, dopaminergic, and cholinergic projections are in red, blue, green, and brown, respectively. Figure created using BioRender (https://biorender.com/).	101
Figure 3.2. Schematic diagram shows the neurons in the (a) PFC, (b) NAc, and (c) VTA. The green and orange dots represent α7 and α4β2 subunits of nAChRs (nicotinic acetylcholine receptors), respectively. Figure created using BioRender (https://biorender.com/).	104
Figure 3.3. MS/MS spectra of (a) [GABA + K] ⁺ at <i>m/z</i> 142.03, (b) [glutamate + K] ⁺ at <i>m/z</i> 186.02, and (c) the signal at <i>m/z</i> 192.04 acquired from the rat brain sections with ZnO NP-assisted laser desorption ionization mass spectrometry imaging (LDI MSI).	116
Figure 3.4. Ion images of vehicle-treated (left) or nicotine-treated (right) tissue sections from the adolescent rat brains acquired with ZnO NP-assisted LDI MSI, (a) [GABA + K] ⁺ at <i>m/z</i> 142.03, (b) [glutamate + K] ⁺ at <i>m/z</i> 186.02, and (c) the signal at <i>m/z</i> 192.04 and (d) schematic diagrams showing the ROI (PrL (prelimbic cortex), IL (infralimbic cortex), NAcC (nucleus accumbens core), NAcSh (nucleus accumbens shell), DS (dorsal subiculum), and VS (ventral subiculum)) are presented (top to bottom: Bregma +3.00 mm,	

PFC; +2.04 mm, NAc; -6.00 mm, HPC; Paxinos and Watson Atlas; raster size of 80 μm).
..... 117

Figure 3.5. Ion images of **vehicle-treated (left)** or **nicotine-treated (right)** tissue sections from the adult rat brains acquired with ZnO NP-assisted LDI MSI, **(a) [GABA + K]⁺** at m/z 142.03, **(b) [glutamate + K]⁺** at m/z 186.02, and **(c) the signal at m/z 192.04** and **(d)** schematic diagrams showing the ROI (PrL, IL, NAcC, NAcSh, DS, and VS) are presented (top to bottom: Bregma +3.00 mm, PFC; +2.04 mm, NAc; -6.00 mm, HPC; Paxinos and Watson Atlas; raster size of 80 μm). 118

Figure 3.6. Schematic diagram shows the procedures for relative quantitation of neurotransmitters between the **drug-treated** and **vehicle-treated** brains. 120

Figure 3.7. The peak area ratios of (a) [GABA + K]⁺ at m/z 142.03, (b) [glutamate + K]⁺ at m/z 186.02, and (c) the signal at m/z 192.04 in various brain regions between the nicotine-treated and vehicle-treated brains from the adolescent rats (n = 10). The arithmetic mean and a 95% CI of nicotine/vehicle peak area ratios are displayed as a bar. Asterisks indicate the brain regions that featured significant differences using the peak area ratios between the nicotine-treated and vehicle-treated adolescent rat brains in the Student t-test (*p < 0.05). 125

Figure 3.8. The peak areas of [GABA + K]⁺ at m/z 142.03 in various brain regions from the nicotine-treated and vehicle-treated adolescent rat brains (n = 10). Asterisks indicate the brain regions that featured significant differences between the nicotine-treated and vehicle-treated adolescent rat brains in the Student t-test (*p < 0.05). 126

Figure 3.9. The peak area ratios of (a) [GABA + K]⁺ at m/z 142.03, (b) [glutamate + K]⁺ at m/z 186.02, and (c) the signal at m/z 192.04 in various brain regions between the nicotine-treated and vehicle-treated adult rat brains (n = 8, PrL, IL, NAcC, NAcSh, and DS; n = 7, VS). The arithmetic mean and a 95% CI of nicotine/vehicle peak area ratios are displayed as a bar. Asterisks indicate the brain regions that featured significant differences using the peak area ratios between the nicotine-treated and vehicle-treated adult rat brains in the Student t-test (*p < 0.05). 130

Figure 3.10. Comparison of the averaged signal ratios of **(a) [GABA + K]⁺** at m/z 142.03, **(b) [glutamate + K]⁺** at m/z 186.02, and **(c) the signal at m/z 192.04** in various ROI between the nicotine-treated and vehicle-treated brains from the adolescent and adult rats (n = 10, adolescent; n = 8, PrL, IL, NAcC, NAcSh, and DS; n = 7, VS; adult). The averaged arithmetic mean of nicotine/vehicle peak area ratios is displayed as a bar. Each error bar represents a 95% CI of nicotine/vehicle peak area ratios. Asterisks indicate the brain regions that featured significant differences using the peak area ratios between the nicotine-treated and vehicle-treated rat brains in the Student t-test (*p < 0.05). 132

Figure 4.1. A simplified diagram of the main connections to and from the PFC (prefrontal cortex), NAc (nucleus accumbens), thalamus, dHPC (dorsal hippocampus), vHPC (ventral hippocampus), Amyg (amygdala), and VTA (ventral tegmental area), in a sagittal section

of a rodent brain. GABAergic, glutamatergic, and dopaminergic projections are in red, blue, and green, respectively. Figure created using BioRender (<https://biorender.com/>).

143

Figure 4.2. Ion images of **vehicle-** (left) or **THC-treated** (right) tissue sections from the adolescent rat brains acquired with ZnO NP-assisted laser desorption ionization mass spectrometry imaging (LDI MSI), **(a) [GABA + K]⁺** at *m/z* 142.03, **(b) [glutamate + K]⁺** at *m/z* 186.02, and **(c) the signal at *m/z* 192.04** and **(d)** schematic diagrams showing the ROI (PrL, IL, NAcC, NAcSh, DS, VS, VTA, and SN) are presented (top to bottom: Bregma +3.00 mm, PFC; +2.04 mm, NAc; -6.00 mm, HPC; Paxinos and Watson Atlas; raster size of 80 μ m). 155

Figure 4.3. Ion images of **vehicle-treated** (left) or **THC-treated** (right) tissue sections from the adult rat brains acquired with ZnO NP-assisted LDI MSI. **(a) [GABA + K]⁺** at *m/z* 142.03, **(b) [glutamate + K]⁺** at *m/z* 186.02, and **(c) the signal at *m/z* 192.04** and **(d)** schematic diagrams showing the ROI (PrL, IL, NAcC, NAcSh, DS, VS, VTA, and SN) are presented (top to bottom: Bregma +3.00 mm, PFC; +2.04 mm, NAc; -6.00 mm, HPC; Paxinos and Watson Atlas; raster size of 80 μ m). 156

Figure 4.4. The peak area ratios of **(a) [GABA + K]⁺** at *m/z* 142.03, **(b) [glutamate + K]⁺** at *m/z* 186.02, and **(c) the signal at *m/z* 192.04** between the THC-treated and vehicle-treated adolescent rat brains in various regions (n = 10, PrL, IL, NAcC, and NAcSh; n = 6, DS and VS; n = 4, VTA and SN). The arithmetic mean and 95% CI of THC/vehicle peak area ratios are displayed as a bar. Asterisks indicate the brain regions that featured significant differences using the peak area ratios between the THC-treated and vehicle-treated adolescent rat brains in the Student t-test (*p < 0.05). 160

Figure 4.5. The peak area ratios of **(a) [GABA + K]⁺** at *m/z* 142.03, **(b) [glutamate + K]⁺** at *m/z* 186.02, and **(c) the signal at *m/z* 192.04** between the THC-treated and vehicle-treated adult rat brains in various regions (n = 8). The arithmetic mean and 95% CI of THC/vehicle peak area ratios are displayed as a bar. Asterisks indicate the brain regions that featured significant differences using the peak area ratios between the THC-treated and vehicle-treated adult rat brains in the Student t-test (*p < 0.05). 164

Figure 4.6. Comparison of the averaged signal ratios of **(a) [GABA + K]⁺** at *m/z* 142.03, **(b) [glutamate + K]⁺** at *m/z* 186.02, and **(c) the signal at *m/z* 192.04** between the THC-treated and vehicle-treated brains in various brain ROI in the adolescent and adult rats (n = 10, PrL, IL, NAcC, and NAcSh; n = 6, DS and VS; n = 4, VTA and SN; adolescent rat brains; n = 8, adult rat brains). The averaged arithmetic mean of THC/vehicle peak area ratios is displayed as a bar. Each error bar represents a 95% CI of THC/vehicle peak area ratios. Asterisks indicate the brain regions that featured significant difference using the peak area ratios between the THC-treated and vehicle-treated rat brains in the Student t-test (*p < 0.05). 167

List of Equations

		Page
$R = \frac{m/z}{\Delta(m/z)}$	Eq. 1.1	27
$zeV = \frac{1}{2}mv^2$	Eq. 1.2	32
$v = \sqrt{\frac{2zeV}{m}}$	Eq. 1.3	32
$t = \frac{1}{v} = \frac{1}{\sqrt{\frac{2zeV}{m}}} = \frac{1}{\sqrt{2eV}}\sqrt{\frac{m}{z}}$	Eq. 1.4	32
$\frac{m}{z} = t^2 \left(\frac{2eV}{l^2} \right)$	Eq. 1.5	32

List of Symbols and Abbreviations

α	alpha
β	beta
γ	gamma
Δ	delta
Δ -9-THC	Δ -9-tetrahydrocannabinol
$\Delta(m/z)$	the width of a peak at 50% of the peak height
μL	microlitre (1 μL = 10^{-6} L)
μm	micrometre (1 μm = 10^{-6} m)
2-AG	2-arachidonoyl glycerol
9-AA	9-aminoacridine
AA	amino acids
ACC	anterior cingulate cortex
ACh	acetylcholine
ACN	acetonitrile
AEA	anandamide
AGC	automatic gain control
Akt	protein kinase B
AMPA	α -amino-3-hydroxy-5-methyl-4-isoxazolepropionic acid
Amyg	amygdala
ARG	autoradiography
ASMS	American Society for Mass Spectrometry
ATP	adenosine triphosphate
BG	basal ganglia
BNDM	1,1'-binaphthyl-2,2'-diamine
C18	molecules contain 18 carbon atoms
C8	molecules contain 8 carbon atoms
CB1Rs	cannabinoid type 1 receptors
CBRs	cannabinoid receptors
CE	capillary electrophoresis

CHCA	α -cyano-4-hydroxycinnamic acid
CHCl ₃	chloroform
CI	confidence interval
cm	centimetre (1 cm = 10 ⁻² m)
CNS	central nervous system
D1R	dopamine type 1 receptors
Da	Dalton, 1 Da = 1 u (atomic mass unit) = 1 g/mol
DAN	1,5-diaminonaphthalene
DDA	data-dependent acquisition
DE	delayed extraction
DESI	desorption electrospray ionization
DHB	2,5-dihydroxybenzoic acid
dHPC	dorsal hippocampus
DMPC	1,2-dimyristoyl-sn-glycero-3-phosphocholine
DPH	1,6-diphenyl-1,3,5-hexatriene
DS	dorsal subiculum
e	electron charge, 1 e = 1.6 x 10 ⁻¹⁹ Coulomb
eCB	endocannabinoid
EI	electron impact
EM	electron multiplier
EP	electrophysiology
ERK	extracellular signal-regulated kinase
ESI	electrospray ionization
FA	fatty acids
fMRI	functional magnetic resonance imaging
FMP-10	methylated 4-(anthracen-9-yl)-2-fluoro-1-alkylpyridin-1-ium
FT-ICR	Fourier-transform ion cyclotron resonance
g	gravitational acceleration, g = 9.81 m/s ²
GABA	γ -aminobutyric acid
GABA-d6	4-aminobutyric acid-2,2,3,3,4,4-d6
GAD-67	glutamic acid decarboxylase-67

GC	gas chromatography
GC–MS	gas chromatography coupled to mass spectrometry
GluA1	subunit of α -amino-3-hydroxy-5-methyl-4-isoxazolepropionic acid subtype of glutamate receptors
GluA2	subunit of α -amino-3-hydroxy-5-methyl-4-isoxazolepropionic acid subtype of glutamate receptors
GluN2B	subunit of N-methyl-D-aspartate subtype of glutamate receptors
GPC	G-protein-coupled
GSK-3	glycogen synthase kinase-3
HILIC	hydrophilic interaction liquid chromatography
HPC	hippocampus
HPLC	high performance liquid chromatography
i.p.	intraperitoneal injection
IL	infralimbic cortex
IM	ion mobility
ISP	isopropyl
IT	injection time
ITO	indium-tin oxide
K ⁺	potassium ion
kDa	kilodalton
KEGG	Kyoto Encyclopedia of Genes and Genomes
kg	kilogram
KOAc	potassium acetate
kV	kilovolt
l	the length of a flight tube
LAESI	laser ablation electrospray ionization
LC	liquid chromatography
LC–MS	liquid chromatography coupled to mass spectrometry
LDI	laser desorption/ionization
LLE	liquid-liquid extraction
LMWM	low molecular weight molecules

LTQ	linear quadruple ion trap
m	the mass of an ion
M ⁺	molecular ion
<i>m/z</i>	mass-to-charge ratio
MALDI	matrix-assisted laser desorption ionization
ME	microchip electrophoresis
MeOH	methanol
mg	milligram (1 mg = 10 ⁻³ g)
mGluR2	metabotropic glutamate receptor 2
min	minute
mL	millilitre (1 mL = 10 ⁻³ L)
mM	millimolar (1 mM = 10 ⁻³ M)
mm	millimetre (1 mm = 10 ⁻³ m)
mPFC	medial prefrontal cortex
MRI	magnetic resonance imaging
MRS	magnetic resonance spectroscopy
MRSI	magnetic resonance spectroscopy imaging
MS	mass spectrometry
MS/MS	tandem mass spectrometry
MSI	mass spectrometry imaging
MW	molecular weight
MΩ·cm	megohm-centimetre
n	sample size
Na ⁺	sodium ion
NAA	N-acetylaspartate
NAc	nucleus accumbens
NAcC	nucleus accumbens core
nAChRs	nicotinic acetylcholine receptors
NAcSh	nucleus accumbens shell
NALDI	nanostructure-assisted laser desorption/ionization
NaOAc	sodium acetate

NCE	normalized collision energy
Nd:YAG	neodymium-doped yttrium aluminum garnet
NEDC	N-(1-naphthyl) ethylenediamine dihydrochloride
ng	nanogram (1 ng = 10 ⁻⁹ g)
nm	nanometer (1 nm = 10 ⁻⁹ m)
NMDA	N-methyl-D-aspartate
NMR	nuclear magnetic resonance
NP	nanoparticle
NT	neurotransmitters
OA	organic acids
p	p-values in the Student t-test
p70S6K	ribosomal protein S6 kinase beta-1
PBS	phosphate-buffered saline
PEG 400	polypropylene glycol 400
PET	positron emission tomography
PFC	prefrontal cortex
pg/mm ²	picogram per square millimetre (1 pg = 10 ⁻¹² g)
pH	power of hydrogen
PNA	N-phenyl-2-naphthylamine
PND	postnatal day
ppm	parts per million
PrL	prelimbic cortex
psi	pounds per square inch
R	resolution
R ²	the square of the correlation coefficient
RF	radio frequency
RNA	ribonucleic acid
ROI	regions of interest
RPLC	reversed-phase liquid chromatography
RRHD	rapid resolution high definition
S/N	signal-to-noise ratio

SEM	scanning electron microscope
SIMS	secondary ion mass spectrometry
SL	sterol lipids
SN	substantia nigra
SPE	solid-phase extraction
SPME	solid-phase microextraction
t	time
TFA	trifluoroacetic acid
THC	Δ -9-tetrahydrocannabinol
TOF	time-of-flight
TOF-TOF	tandem time-of-flight
UV	ultraviolet
V	applied voltage
v	velocity
vHPC	ventral hippocampus
vol	volume
VS	ventral subiculum
VTA	ventral tegmental area
wt	weight
z	net charge of an ion

List of Appendices

Appendix I – Chapter 2 Supplementary.....	183
Appendix II – Copyright Permission	196

Chapter 1: Introduction of Small Molecule Analysis by Mass Spectrometry

1.1 Overview of Small Molecules in the Brain

Small molecules are chemical compounds with a molecular weight of less than 1000 Da [1]. The majority of drugs, drug metabolites, metabolites, and major neurotransmitters are small molecules.

1.1.1 Metabolites in the Brain

Metabolites are the intermediate and end products of complex cellular activities. A large number of small molecules from multiple categories, such as amino acids, alkaloids, fatty acids, carbohydrates, nucleosides, organic acids, lipids, and peptides, are metabolites. Metabolites play essential roles in energy production and storage, signalling, sensing, and apoptosis in the brain [2-6]. The generation of adenosine triphosphate (ATP) from glucose provides energy in the brain. Metabolites are also signalling molecules and control a wide range of biological processes. Sensing neurons or sensors, either enzymes or metabolite-bound proteins, receive the metabolite information and transform the chemical signals into cell signalling [4, 5]. Metabolites are released from apoptotic cells as messengers to actively modulate the neighbouring cells [6].

Metabolites often represent the response to the environment and upstream molecular species such as genes, transcripts, and enzymes [7]. Therefore, metabolite profiling can be applied to understand the effects of drugs on the central nervous system (CNS) and to distinguish different stages of disease. Alterations in metabolites in the CNS, such as amino acids, fatty acids, nucleosides, and carbohydrates, have been reported in brain cancer [8] and CNS disorders [9, 10]. For example, N-acetylaspartate (NAA) is synthesized in the

mitochondria of neurons under normal conditions. A decline in NAA level is usually considered a marker of neuronal dysfunction or death [9, 10]. Normal cells use fatty acid oxidation and glucose oxidation to produce ATP, while glucose is converted to lactate in cancer cells, and increased lactate production is observed [8].

1.1.2 Neurotransmitters in the Brain

Neurotransmitters transmit signals across a synapse from one neuron to another, allowing them to communicate with each other. As shown in Figure 1.1, when a neuron is stimulated, the vesicles storing the neurotransmitters merge with the cell membrane and release the neurotransmitters into the synapse, a tiny gap between neurons. Neurotransmitters then move across the synapse and attach to the receptors on the other neuron, transmitting the signal [11]. At a synapse, the neuron sending the neurotransmitters is called the presynaptic neuron, and the one receiving the neurotransmitters is called the postsynaptic neuron. Common neurotransmitters include acetylcholine (ACh), γ -aminobutyric acid (GABA), glutamate, dopamine, serotonin, norepinephrine, and histamine. Depending on the type of neurotransmitters, the signals can be transmitted or blocked. For instance, GABA is the primary inhibitory neurotransmitter, which decreases the likelihood of neurons firing a signal, so the signal is more likely to be stopped. Similarly, serotonin acts as an inhibitory neurotransmitter in the CNS. Glutamate is the principal excitatory neurotransmitter, making the neuron more likely to fire a signal and to pass the signal to the next neuron. Dopamine can have both excitatory and inhibitory effects depending on the types of receptors [12]. The neurotransmitter activity is terminated by the inactivation of neurotransmitters by reuptake into the presynaptic neuron, breakdown in

the synapse, or diffusion into the surrounding medium [13]. For example, ACh is hydrolyzed into acetate and choline by acetylcholine esterase enzyme in the synapse, while serotonin is taken up into the presynaptic neuron via the serotonin transporter for recycling [11].

Multiple neurological disorders have been linked to abnormalities of neurotransmitter systems [14-16]. Parkinson's disease is resulted from the death of dopaminergic neurons in the substantia nigra [16]. Excessive glutamate signalling is involved in neurodegenerative diseases such as Alzheimer's and Parkinson's disease [14]. In neuropsychiatric disorders like schizophrenia, increased glutamatergic neurotransmission has also been reported [15].

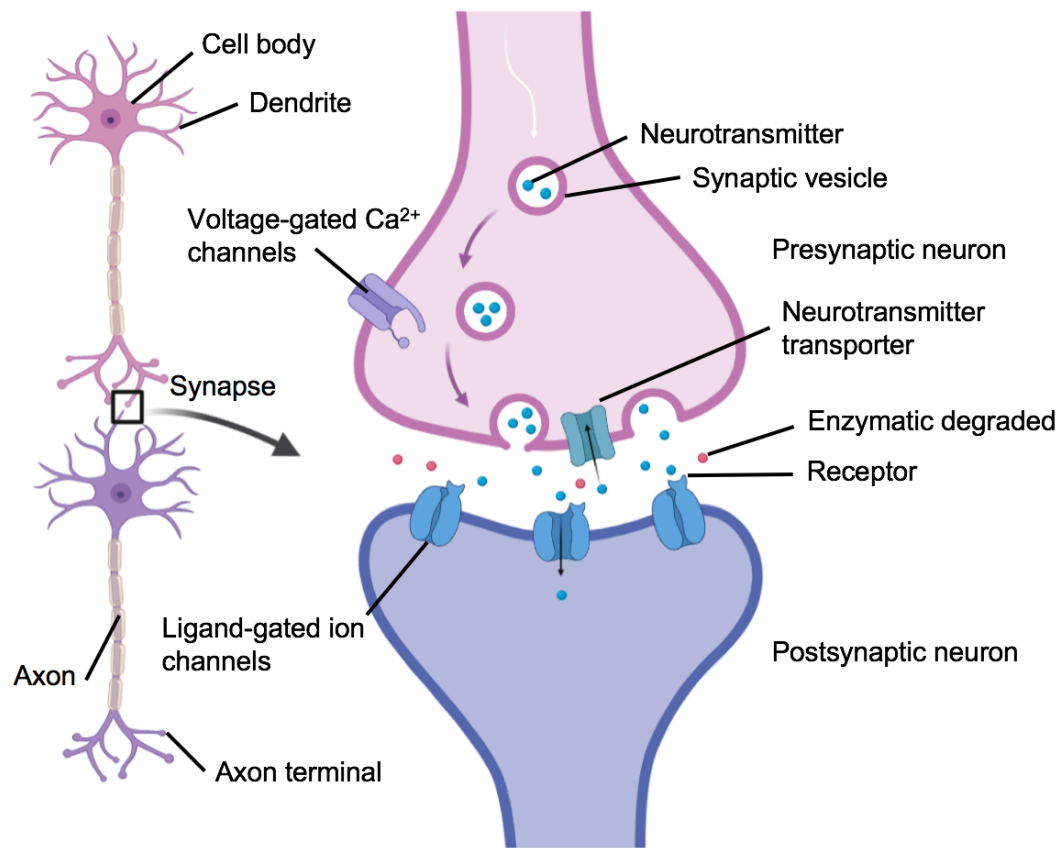


Figure 1.1. Schematic diagram shows the neurotransmission between the presynaptic and postsynaptic neurons. Figure created using BioRender (<https://biorender.com/>).

1.2 Small Molecule Extraction Techniques from Brains

The components of brain tissues are complex and contain cells, proteins, lipids, salts, endogenous small molecules, etc. Therefore, the extraction of small molecules is vital to separate them from interfering compounds. Small molecules can be extracted from post-mortem brain tissues using liquid-liquid extraction (LLE) and solid-phase extraction (SPE). In contrast, microdialysis, ultrafiltration, and solid-phase microextraction (SPME) have been mainly applied to *in vivo* small molecule collections from live animals because of their minimally invasive feature. Efficient and reproducible extraction of target molecules in complex biological samples with high sensitivity is always desired [17].

1.2.1 Liquid-liquid Extraction

LLE is the easiest method to extract analytes from brain tissue homogenates and can be followed by direct analysis of the resulting extract [18]. It involves the extraction of analytes from one solution to another immiscible liquid. Analytes are extracted into the solvent with similar polarity based on the “like dissolves like” principle. It offers moderate recovery and selectivity but consumes large volumes of organic solvents [19]. In addition, manual operations are time-consuming and labor-intensive, although automation is possible with 96-well plates.

1.2.2 Solid-phase Extraction

SPE uses solid adsorption media to adsorb, separate, and enrich the target compounds from brain tissue homogenates. It is currently one of the most widely used methods in the extraction of small molecules. The principle of SPE is similar to that of chromatographic

separation techniques, which is based on diverse affinities of analytes and interfering compounds onto the solid stationary phase. When the analytes of interest are retained on the stationary phase, analytes are then eluted from the stationary phase with a proper eluent. When undesired compounds are retained on the stationary phase, the mobile phase containing the analytes is collected and can be used directly for subsequent analysis. By applying solid phases made of different materials, selective extraction of various target compounds can be achieved [20]. Compared to traditional LLE, SPE has the advantages of less solvent consumption, higher recovery and sensitivity, and better selectivity and reproducibility.

1.2.3 Microdialysis

Microdialysis is employed to sample free chemicals from the extracellular fluid of brain tissues of live animals. The technique is minimally invasive using probes of approximately 200 to 500 μm in diameter [21]. Before the experiment, the probe is implanted in the region of interest and connected to two thin cannulae. The perfusate, which has similar ionic strength and composition to the extracellular fluid, flows into and out of the probed region with the aid of an external pump. The probe is made of a hollow-fibre semi-permeable membrane with a specific molecular weight cutoff between 1 to 100 kDa. The sampling process is based on the diffusion of chemicals from the extracellular fluid into a microdialysis probe. The microdialysis probe creates a concentration gradient between the extracellular fluid in the brain region and the perfusate. Because of the concentration gradient, molecules in the extracellular fluid that are not present in the perfusate diffuse across the membrane into the collected solution, the dialysate [21]. Due to the filtering

property of the semi-permeable membrane, tissue components, blood cells and other large-molecule impurities are blocked in the tissue side of the membrane. Depending on the flow rate of perfusate, properties of analytes and probe membrane, etc., the relative recovery in microdialysis is typically less than 40% [22].

Although microdialysis has been extensively applied for small molecule collection such as metabolites and drugs [23, 24], large molecular weight compounds have become possible due to the availability of large molecular weight cutoff membranes [25]. The primary application of microdialysis has been in neuroscience research [26], but it has also been extensively used for pharmaceutical applications, such as pharmacokinetic and metabolism studies of drugs in tissues [27].

1.2.4 Ultrafiltration

Similar to microdialysis, ultrafiltration is also an *in vivo* sampling technique that can directly extract chemicals from the brain tissues of live animals [28]. The setup of ultrafiltration is similar to that of microdialysis except that the sampling probe is connected to a vacutainer or a peristaltic pump. Analytes are drawn from the extracellular fluid to the sampling probe through the semi-permeable membrane pores under the driving force of negative pressure on the collecting side of the membrane [29]. Therefore, ultrafiltration offers a more straightforward reflection of analyte concentration in the extracellular fluid when compared to microdialysis. However, a very limited volume can be extracted using ultrafiltration before inducing severe damage to the test animal.

1.2.5 Solid-phase Microextraction

SPME integrates sampling, isolation, and enrichment of free molecules in the liquid samples or gas-phase samples in one solvent-free step [30, 31]. The extracted amount of analytes is small and almost negligible compared to the quantity of analytes in the sample. In SPME, a porous fibre coated with extraction phase is immersed into the sample to extract analytes of interest. Based on the adsorption equilibrium of the analytes between the sample and the extraction phase, analytes are adsorbed onto the surface of the coating material. The analytes on the sample probe can be vaporized directly for analysis or washed off with a small volume of solvent, which results in a sample solution that can be analyzed directly. SPME has attracted more attention in its application to *in vivo* small molecule collection from live animals by using minimally invasive probes with small diameters [32]. Depending on the coating materials, SPME probes can be used to capture specific analytes using high-selectivity coatings in a high-efficiency manner, which allows the analysis of trace analytes [33]. Moreover, *in vivo* SPME is complementary to microdialysis; e.g., SPME with probes made of hydrocarbon materials is preferred when extracting semi-hydrophilic and hydrophobic compounds, while microdialysis is preferred for hydrophilic compound extraction [34].

1.3 Small Molecule Analyses

1.3.1 Indirect Analyses of Neurotransmitters

Positron emission tomography (PET) and autoradiography (ARG) have been used to measure the release of neurotransmitters from neurons indirectly by detecting the changes in radioactive ligand binding, while electrophysiology (EP) tools examine the electrical activities of neurons to indirectly reveal the neurotransmitter release.

1.3.1.1 Positron Emission Tomography

A radioactive tracer, usually an isotope with a short half-life such as ^{11}C , ^{13}N , and ^{18}F , is used in PET. As the isotope decays, a positron is emitted. When the positron encounters an electron, two gamma photons are produced in opposite directions (the process is referred to as annihilation). The signal is recorded when two gamma photons in opposite directions reach the detector simultaneously [35]. Some of the positron-emitting radioisotopes used for PET studies have extremely short half-lives; e.g., the half-life of ^{15}O is 2 minutes, so they must be synthesized on-site using a cyclotron.

PET is a non-invasive imaging technique that can reveal the metabolism of molecules and indirectly measure neurotransmitter release [36]. However, the spatial resolution in the millimetre level is low when compared to other imaging techniques. The neurotransmitter measurement is based on the competition between the radioactive ligands and endogenous neurotransmitter binding to its receptors [37, 38]. The neurotransmitter release is indicated by a decrease in radioactive ligand binding to the receptors.

1.3.1.2 Autoradiography

ARG uses radioactive tracers such as ^{32}P , ^{35}S , ^3H , ^{14}C , and ^{125}I . Biological samples are coated with a thick photographic emulsion layer containing silver halide and left in the dark while the radioisotope decays. Each decay causes the precipitation of silver in the emulsion. The distribution of radiation derived from the radioactive substance is indicated by the position of developed silver particles [39]. Similarly, the release of endogenous neurotransmitters is estimated indirectly from the changes in neurotransmitter receptor binding with radioactive ligand [40]. Moreover, *in vivo* autoradiography using laboratory animals has been widely used in metabolic studies, disease monitoring, and new drug development [41]. The spatial resolution of ARG can reach below 20 μm [42].

1.3.1.3 Electrophysiology

Neurons communicate via electrical and chemical signals. Chemical signals, conducted by neurotransmitters, transmit signals across a synapse between two neurons. Electrical signals, on the other hand, are carried along neurons. Differences in the concentration of ions between the intracellular and extracellular sides of the cell membrane as well as the types of ion channels create a membrane potential, the electrical signal. EP explores the electrical activities of neurons. In an EP experiment, a microelectrode is introduced into a live animal's brain and detects the electrical activity generated from the neurons adjacent to the electrode tip. The signals are then transmitted to an amplifier, an oscilloscope, and a computer. Based on the electrode location relative to the cell, *in vivo* electrophysiological recordings can be grouped into extracellular recordings from the extracellular environment near a cell, intracellular recordings from the inside of a cell, and patch-clamp recordings

from the membrane of a cell [43]. When a neuron is stimulated, the ion flow through ion channels in the cell membrane causes membrane potential change. When the membrane potential is strong enough, electrical signals travel down the axon (the process is called the firing of a neuron) and eventually trigger the release of neurotransmitters. Since the firing of neurons is associated with the release of neurotransmitters, the electrical activities of neurons can be recorded to indirectly reveal the release of neurotransmitters.

However, it is difficult to electrophysiologically identify neurons. Additional identification from molecular markers such as proteins and ribonucleic acid (RNA) [44] is required. Depending on the neuron populations and how active the neurons are in the brain regions, EP experiments can take a long time to record enough electrical activities of neurons. EP has been applied to examine the activities of neurons such as GABAergic and dopaminergic neurons in live animal brains [45, 46].

1.3.2 Direct Analyses of Small Molecules

Targeted analyses of small molecules have been achieved using electrochemical [47-49] and optical sensing [50-52] techniques. Untargeted analyses of small molecules allow for a detailed assessment of all small molecules extracted from a sample. However, it is impossible to obtain the information of all small molecules at once, as many factors affect the small molecule recovery, depending on the functional group of the small molecules and extraction methods. In addition, molecules may be present in samples at low abundances that are below the limit of detection of current instrumentation. Moreover, there are still unknown small molecules that are not covered in the current databases. Mass spectrometry

(MS) and nuclear magnetic resonance (NMR) spectroscopy [53] are two main analytical techniques used in both targeted and untargeted analyses of small molecules from complex biological samples. Untargeted analyses are most effective when implemented in a high-resolution mass spectrometer to facilitate structural characterization of the small molecules. Moreover, both techniques can be used for qualitative and quantitative analyses of small molecules.

1.3.2.1 Nuclear Magnetic Resonance

NMR detects signals from excited nuclei in a magnetic field. Because a particular nucleus in different molecules experiences different chemical environments due to surrounding electrons, it experiences slightly different practical applied fields and resonates at slightly different frequencies. The resonant frequency of the nucleus, or chemical shift relative to a standard, allows the identification of compounds containing the given nucleus. The sensitivity of NMR depends on the number of nuclear spins being observed, the natural abundance of the nucleus, magnetic field strength, etc. [54]. Although the sensitivity of NMR is lower compared to MS, the non-destructive nature of NMR makes it the preferred tool for *in vivo* studies [53]. NMR spectroscopy has been extensively applied to clinical studies using nuclei such as ^1H and ^{31}P by acquiring signals from a volume of sample in the target region [55]. However, limited by its sensitivity, the application of NMR spectroscopy has been limited to detect a small group of highly abundant molecules, e.g., glucose, lactate, NAA, myo-inositol, creatine, choline, glutamate, glutamine, etc. [56]. In addition, magnetic resonance spectroscopy imaging (MRSI) provides molecule spatial information by dividing a large volume within the region of interest into several smaller

voxels and measuring multiple small voxels simultaneously. Its application in *in vivo* studies is still limited due to the lower sensitivity from smaller voxels.

1.3.2.2 Mass Spectrometry (MS)

MS measures the mass-to-charge ratios (m/z) and abundances of gas-phase ions to determine and quantify the molecules from a sample. The accurate masses of molecules and characteristic fragments allow the identification of molecules. It is playing an increasingly dominant role in large-scale small molecule analyses due to its high sensitivity, high resolution, high throughput, good mass accuracy, and wide dynamic range [57, 58].

The direct coupling of separation devices with MS makes it superior for targeted analyses of small molecules from complex biological samples. Gas chromatography (GC), liquid chromatography (LC), capillary electrophoresis (CE), and ion mobility (IM) are currently used separation methods prior to MS acquisition [57, 59, 60]. Among them, GC and LC coupled to MS (GC–MS and LC–MS) are the most widely used. Compared to LC–MS, GC–MS is highly reproducible and produces repeatable fragmentation. It is preferred for the analysis of volatile compounds, and derivatization is required for non-volatile compounds. LC–MS has become a dominating analytical technique in small molecule analyses as it has a wider coverage without the need of derivatization. The traditional reversed-phase liquid chromatography (RPLC) using C8 or C18 nonpolar stationary phase is used for the separation of nonpolar to slightly polar compounds, whereas the hydrophilic interaction liquid chromatography (HILIC) with a polar stationary phase is the choice for highly polar to slightly polar compounds. Currently, electron impact (EI) is the ionization

method of choice for GC–MS analysis, and electrospray ionization (ESI) is the favourite ionization technique for LC–MS analysis of small molecules. Different ionization methods facilitate the detection of different molecules, so more small molecules could be covered by MS compared to NMR.

Mass spectrometry imaging (MSI), on the other hand, offers the investigations of the spatial distribution of a large number of small molecules within a variety of tissue samples. In MSI, MS data is acquired at spatially resolved locations within a biological sample. In contrast to PET and autoradiography, specific labelling is not required. Because molecular information from multiple compounds is collected from each location, the spatial information of multiple analytes is obtained in one MSI experiment. MSI of small molecules has been mostly applied in biomarker discovery and pharmaceutical research [61-64]. Although desorption electrospray ionization (DESI) MSI may be useful for analyzing tissue samples during surgery [65, 66], most MSI applications are limited to *in situ* studies because MSI is invasive and destructive.

1.4 Ionization Techniques in Mass Spectrometry Imaging (MSI)

Ionization happens in the ion source, where gas-phase ions are generated. Ionization techniques often used in MSI are DESI, secondary ion mass spectrometry (SIMS), matrix-assisted laser desorption/ionization (MALDI), laser ablation electrospray ionization (LAESI), etc. The concept of MSI was introduced over 50 years ago using SIMS [67, 68]. The widespread application of MSI was realized after the introduction of MALDI MSI in 1994 by Spengler during the ASMS Conference and its extensive development by Caprioli [69]. The ionization methods can be grouped by two major properties. The first one is based on the energy applied to the analytes and whether the target molecules remain intact (soft ionization) or fragment into pieces (hard ionization). MALDI and DESI are soft ionization techniques, so few or no fragments are generated during ionization, and the molecular ions can be easily observed. The second is based on whether ionization occurs within the vacuum chamber of the mass spectrometer or outside the instrument at atmospheric pressure. SIMS and MALDI occur in the vacuum, while DESI and LAESI are conducted at atmospheric pressure.

1.4.1 Secondary Ion Mass Spectrometry

SIMS utilizes high-energy primary ions striking the sample surface to induce the release of secondary analyte ions from the surface. It provides the highest spatial resolution, with it being less than 100 nm [70], for cellular or subcellular small molecule analyses. Because of the extensive surface fragmentation, it is mostly used for analyses of elements and small molecules with a mass range of less than 1000 Da.

1.4.2 Desorption Electrospray Ionization

The application of ESI in MS was initiated for biomolecular analysis by John Fenn [71]. DESI, the extension of ESI to a surface analysis technique, was introduced in 2004 by the Cooks group [72]. DESI is performed by applying charged solvent droplets onto the sample surface for extraction of surface molecules, which are directed into the atmospheric inlet of a conventional mass spectrometer [73]. A high voltage (positive or negative based on the nature of the analytes) is applied to the electrospray emitter. With the presence of high-pressure nitrogen surrounding the solvent, charged spray droplets are generated. Droplets are directed onto the sample surface, where they create a thin liquid layer that dissolves and extracts surface molecules. Secondary charged droplets containing the dissolved analytes are subsequently produced by the continuing impact of primary charged droplets. The secondary droplets proceed through an electrospray-type mechanism to form gaseous ions and are drawn into the MS inlet [74-76]. The angle of spray, the tip to surface distance, the position of the MS inlet, the solvent composition, the solvent flow rate, the applied voltage, and nebulizing gas pressure largely affect the detection efficiency and diffusion of molecules. In the positive ion mode, ions are formed from neutral small molecules by protonation or other cation attachment, while ions are formed by deprotonation in the negative mode.

DESI is the youngest MSI approach, allowing ambient surface sampling with minimal sample pretreatment, while the spatial resolution is lower than SIMS and MALDI. Limited by the size of electrospray impact, the spatial resolution of DESI is around 50 μm . With the application of nano-DESI, the spatial resolution can reach below 20 μm [77].

1.4.3 Laser Ablation Electrospray Ionization

More recently, LAESI, a combination of sample irradiation by mid-infrared laser ablation and ESI, was developed by the Vertes group [78]. In LAESI, the natural water content of cells and tissues is utilized as the matrix. The plume produced after laser ablation is incorporated into the droplets from electrospray above the sample surface for subsequent ionization.

Similar to DESI, LAESI requires minimal sample preparations. However, since water is used as the matrix to absorb the mid-infrared laser energy to generate the gas plume, low water content samples like hair cannot be ablated for further ionization [79]. In addition, the diameter of ablation crater has been decreased to ca. 30 μm after focusing the laser.

1.4.4 Matrix-assisted Laser Desorption Ionization (MALDI)

MALDI was first introduced in 1988 by two independent groups: Tanaka [80] and Karas [81]. With MALDI, analytes are co-crystallized with a matrix. A pulsed laser beam is then irradiated onto the sample surface, and the matrix is ablated, generating a gas plume with matrix and analyte ions. Usually, one proton or cation can be attached to or removed from small molecules, producing primarily singly charged ions. Positively or negatively charged ions can be extracted based on the voltage polarity between the sample plate and the extraction grid. In positive MALDI, ions are formed from small neutral molecules by protonation or other cation attachments. The charge is usually provided by the addition of a proton to yield $[\text{M} + \text{H}]^+$ ions. Besides, alkali metal cations (particularly sodium and potassium) can be added to analytes to form $[\text{M} + \text{Na}]^+$ and $[\text{M} + \text{K}]^+$ ions, respectively.

As shown in Figure 1.2, several ionization mechanisms have been reported to interpret the ion formation during the MALDI process [82-87]. It is proposed that the production of analyte ions involves two steps; the first is the generation of matrix ions within the matrix-analyte crystals by laser irradiation; the second step is the charge transferred from matrix ions to the neutral analytes.

To date, MALDI is the most broadly used ionization technique for MSI due to its high mass range coverage, a wide variety of analyte detection, and superior spatial resolution of less than 10 μm [60, 88, 89]. It allows the analysis of a wide range of molecules, including small molecules (drugs, lipids, and endogenous metabolites) and large molecules (peptides and proteins), with molecular weights ranging from hundreds of Da to beyond 100 kDa.

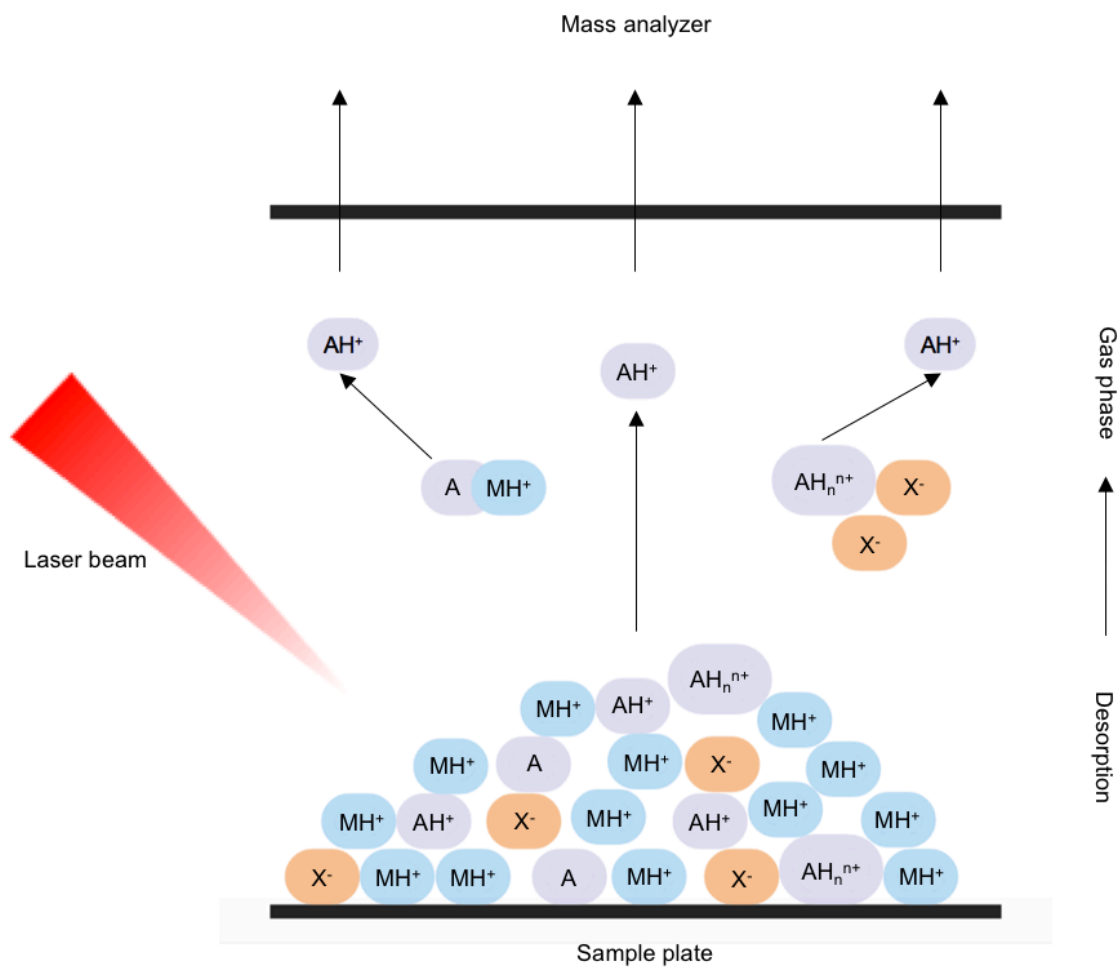


Figure 1.2. Major proposed models for MALDI ionization (A = analyte, M = matrix, X⁻ = counterion).

1.5 MALDI MSI

An overview of the typical MALDI MSI workflow is given in Figure 1.3. It involves sectioning and mounting a thin tissue section (10–20 μm) onto a conductive substrate. The sample then is covered with a homogenous matrix layer, which absorbs the energy from a pulsed laser beam and transfers the energy to surrounding analytes. Before MS analysis, m/z range, laser intensity, and shots/spot are optimized, and the region of interest (ROI) and raster size are selected. Once determined, the laser pulses ablate each spot along with the spatial coordination, collecting one mass spectrum per spot, until the designated ROI is scanned. The spatial distribution of ions is visualized by plotting the intensity detected at each spot.

1.5.1 Tissue Preparations

Tissue preparation represents a critical step for the imaging of small analytes. First, tissues of interest are harvested from the specimen and immediately frozen. The most commonly used method to preserve tissue is to snap-freeze the sample by exposing it to cryogenics such as dry ice and liquid nitrogen and storing it at -80°C until use. Snap-freeze minimizes the development of large ice crystals and avoids damage to the tissue. Generally, tissue is loosely wrapped in aluminum foil, gently placed in the cryogenic solution, and allowed to slowly freeze before it is fully immersed in the liquid nitrogen or buried in dry ice to prevent tissue fracture and deformation.

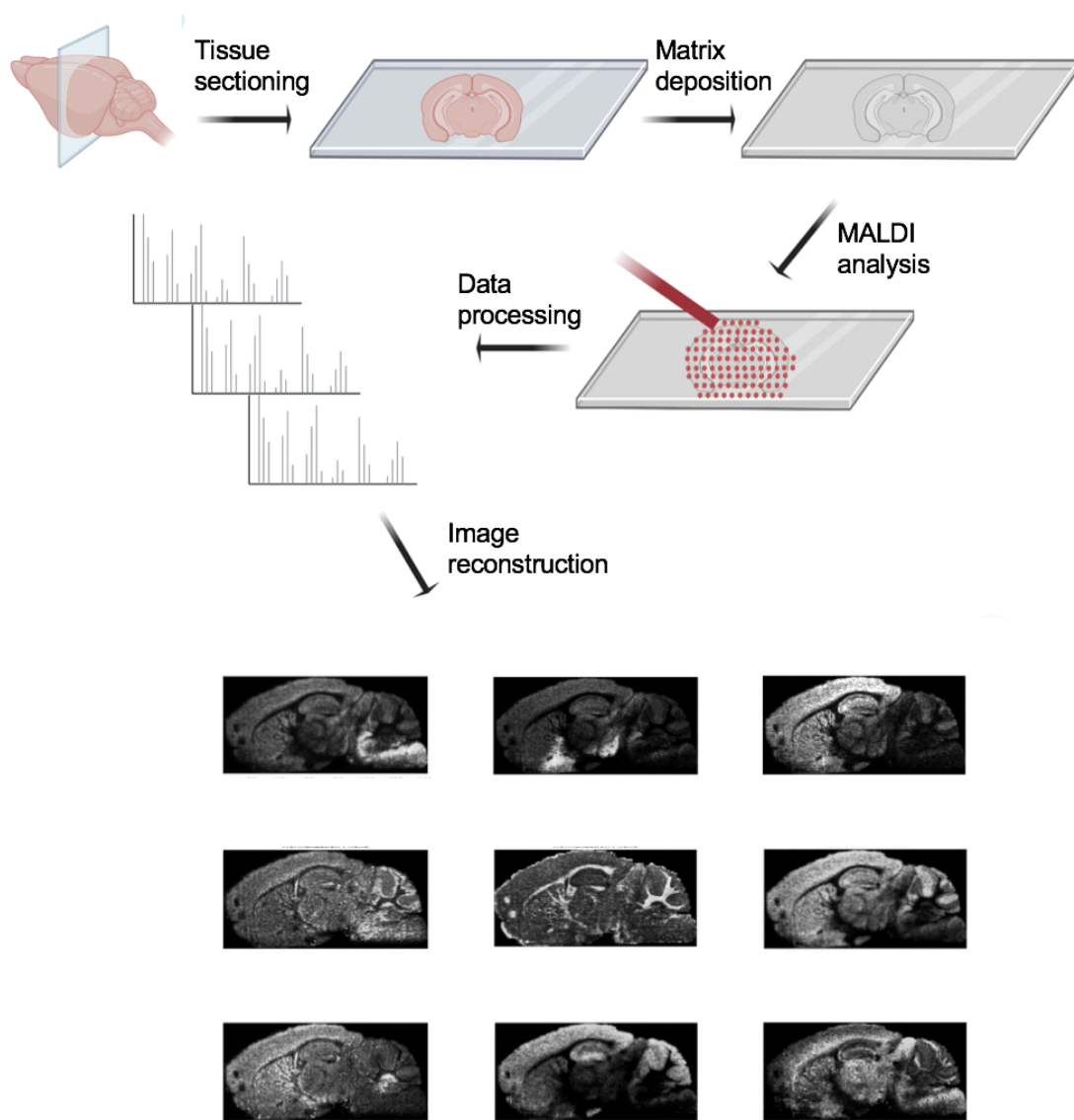


Figure 1.3. Overview of the sample preparation and analysis process for MALDI MSI.

Tissue sections can be thaw-mounted onto a substrate surface simply by placing the tissue section on the surface that has been cooled to the same temperature as the tissue section and then by slowly warming the surface underneath. Alternatively, the tissue section can be flip-mounted by inverting a warm slide and pressing the warm slide on the cold tissue section until the tissue section adheres to the surface of the warm slide. It has been shown that the duration of warming at room temperature during sectioning on a sub-minute time scale can cause degradation [90]. Therefore, when mounting multiple tissue sections in this approach, the time of mounted sections being kept at room temperature can result in signal variations.

A conductive substrate is required to support the application of an electric field to accelerate the ions in the source of MALDI MS. Stainless steel plates or metal targets and indium-tin oxide (ITO)-coated glass slides are used. An advantage of using ITO-coated glass slides is that additional microscopic analyses like histology staining are possible before or after MALDI MSI due to the transparency of glass slides.

1.5.2 Matrix Selection

Different matrices are applied in MALDI MSI to allow the imaging of various compounds. The selection of the matrix depends on the mass range and chemical properties of the analytes. For the imaging of small molecules, strong matrix-related peaks from organic matrices could interface with the analyte peaks when using a low-resolving power instrument. For example, the molecular weights of common organic matrices for the imaging of small molecules are in the range of 150–250 g/mol, such as 2, 4-

dihydroxybenzoic acid (DHB), α -cyano-4-hydroxycinnamic acid (CHCA), 9-aminoacridine (9-AA) at 154, 189, and 194, respectively. With multitudes of matrix-derived peaks generated at m/z values higher than 250 Da from adducts, multimers, and matrix clusters during the laser desorption ionization process [91, 92], the analyte signals with similar m/z cannot be differentiated from matrix-derived peaks. Moreover, the ionization efficiency of analytes is lowered because they compete with matrix ions. The facts above make it difficult to select a matrix for MALDI MSI due to the complexity of biological samples. Inorganic materials based on carbon, silicon, metal, and metal oxides favour the detection of small molecules because of their cleaner matrix backgrounds and have been developed extensively in recent years. A comprehensive review of applications of inorganic materials as matrices in MALDI imaging of small molecules will be presented in Chapter 2.

1.5.3 Matrix Deposition

Matrix deposition is another crucial step in sample preparations for MALDI MSI. It plays an important role in the quality of MS images, particularly the high spatial resolution images. The matrix needs to be uniformly applied on tissue samples with small crystal sizes and to appropriately extract analytes without introducing molecule spatial diffusion. During the matrix deposition, molecules from the surface of samples are incorporated into the matrix crystals. Three widely used methods in matrix deposition are conducted by airbrush, automated sprayer, and sublimation apparatus. Deposition by use of airbrush has been widely used in matrix deposition for MALDI imaging since it is simple, cheap, and relatively fast. The drawbacks of airbrush application are that it is extremely user-

dependent and not always reproducible. Automatic sprayer systems have been developed to deposit the matrix in a robotically controlled manner, helping to make the sample preparation more reproducible. By controlling the temperature of the matrix spraying nozzle, the solvent flow rate, and the velocity of the nozzle, a uniform matrix layer is deposited with minimal analyte diffusion and effective extraction. Sublimation produces an even matrix layer with very fine matrix crystals, which is the best for high-resolution imaging. However, because it is a dry deposition method, sometimes the extraction of analytes is not enough.

1.5.4 Spatial Resolution and Sensitivity

The matrix crystal size and matrix uniformity, along with other instrumental parameters, such as the laser raster step size and laser beam diameter, are factors limiting the spatial resolution of MS images [93]. The size of crystals largely depends on the matrix, matrix concentration, deposition methods, solvent, and incubation time [93]. Matrix crystals must be smaller than the laser raster step size or an inaccurate representation of the spatial distribution will be acquired.

Imaging at spatial resolutions below the beam diameter has been reported using an oversampling method, where pixels are overlapped with one another, and the sample is exhausted at each pixel in the analysis process before moving onto the next pixel [94]. A signal is only detected from the sample in the non-overlapping region. As the minimum laser raster step size is often smaller than the laser beam size, oversampling can provide significant spatial resolution improvements. In addition, several groups have pushed the

resolution of commercial instruments from 5–20 μm to sub-micrometre scale by reducing the laser beam size [95-97].

Although fine features of small tissue regions can be molecularly characterized at high spatial resolutions, the acquisition time and data size increase. Moreover, at high spatial resolutions, a smaller tissue area is ablated, and fewer number of ions are produced. However, post-ionization has been applied to improve the ionization sensitivity of molecules from small tissue areas [97]. It is not always beneficial to image tissue sections at spatial resolutions that are not necessary.

1.6 Mass Analyzers in MSI

The mass analyzer is used to separate gas-phase ions based on their m/z ratios. Commonly used analyzers in MSI include time-of-flight (TOF), Orbitrap, and Fourier-transform ion cyclotron resonance (FT-ICR). The selection of the mass analyzer for MSI usually involves consideration of speed, sensitivity, mass resolving power, and mass range required for targeted analyses with no one mass analyzer optimal for all situations.

1.6.1 Resolving Power and Mass Accuracy

It is essential to include mass resolving power information when discussing the performance of mass spectrometers. The resolving power is the measure of the ability of the mass analyzer to distinguish two adjacent ions differing in the m/z by a small increment, characterized by resolution. Resolving power later has been defined as the measure of the ability to provide a specified value of mass resolution. The resolution (R) for a single peak can be measured with Eq. 1.1, where m/z is the peak position, and $\Delta(m/z)$ is the width of the peak at 50% of the peak height. The narrower the peak is, the higher the resolution is. Resolving power becomes increasingly important when performing untargeted analyses and characterizing molecules with near-identical masses.

$$R = \frac{m/z}{\Delta(m/z)} \quad (\text{Eq. 1.1})$$

Mass accuracy in MS refers to the m/z measurement error, which is the difference between the theoretical m/z and the measured m/z of a target ion, divided by the theoretical m/z of the ion and is usually quoted in parts per million (ppm). The increases in mass accuracy of

an analyzer come as a result of its increased resolving power and increase the confidence level when it comes to molecule identification based on the m/z of peaks.

1.6.2 Orbitrap Analyzer

An Orbitrap analyzer consists of a spindle-like central electrode and a pair of bell-shaped outer electrodes, as shown in Figure 1.4. The ions rotate around the central electrode while moving back and forth along the central electrode (harmonic oscillation). The m/z values are determined by measuring the harmonic oscillation frequency of ions in an electrostatic field along a spindle-like electrode, where m/z is proportional to the square root of the electric field strength and the harmonic oscillation frequency [98]. An ion is detected as it approaches a metal surface and induces charges on the surface, and an electric current is induced as the ion moves towards and away from the metal surface [99].

Orbitrap analyzers exhibit high resolution with 1–5 ppm mass accuracy. However, the mass range of Orbitrap instruments is limited to approximately m/z 4000 since higher m/z compounds are difficult to retain during the orbital rotation. Besides, the Orbitrap analyzer requires a long analysis time. The Orbitrap analyzer can be interfaced to a linear quadrupole ion trap (LTQ) as the mass filter to enable additional structural confirmations of analytes.

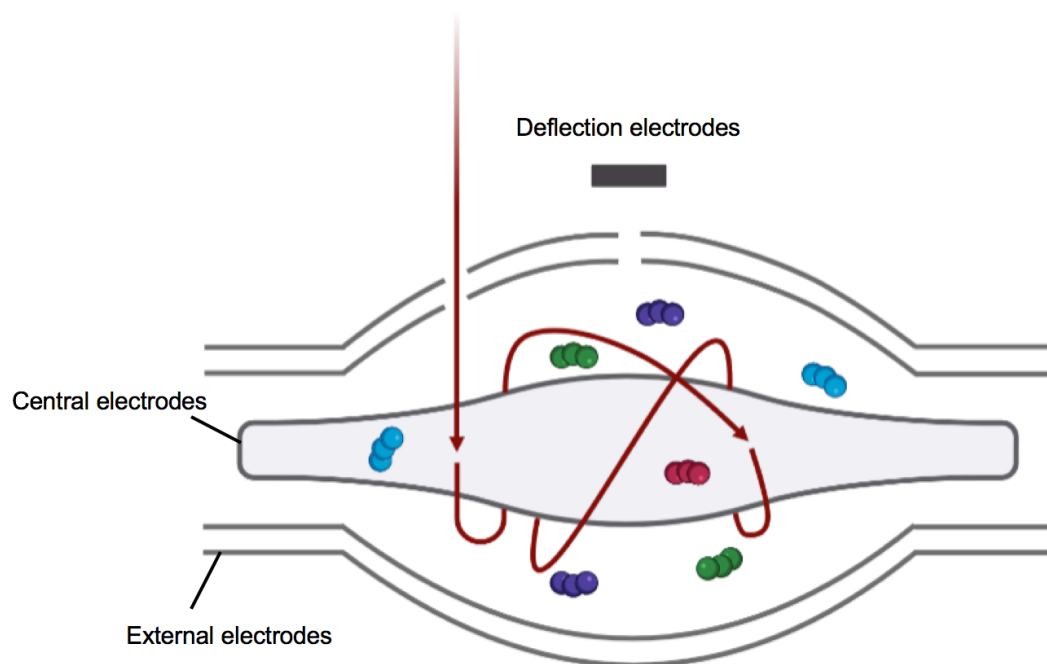


Figure 1.4. Schematic diagram of Orbitrap mass analyzer.

1.6.3 Fourier-transform Ion Cyclotron Resonance Analyzer

An FT-ICR mass analyzer consists of two trapping electrodes, two excitation electrodes, and two detection electrodes, as shown in Figure 1.5. Ions are excited and move between the two detection electrodes, inducing an alternating current called image current. The m/z of ions is dependent on the cyclotron frequency and strength of the magnetic field, which is kept constant for FT-ICR [100]. Ions with varying m/z values move simultaneously with different frequencies and induce image currents with different frequencies, while the number of ions determines the amplitude of the induced image current. The total image current from ions of varying m/z values is recorded as a function of time and then interpreted using Fourier transform analysis to provide m/z values and intensities.

The FT-ICR mass analyzer offers high resolving power and high mass accuracy, which is reported to have mass errors of less than 1 ppm. Like the Orbitrap, the FT-ICR instrument also suffers from a long analysis time, but it has a higher upper mass limit compared to Orbitrap. Commercial FT-ICR instruments also come equipped with other mass analyzers like quadrupole for the mass selection.

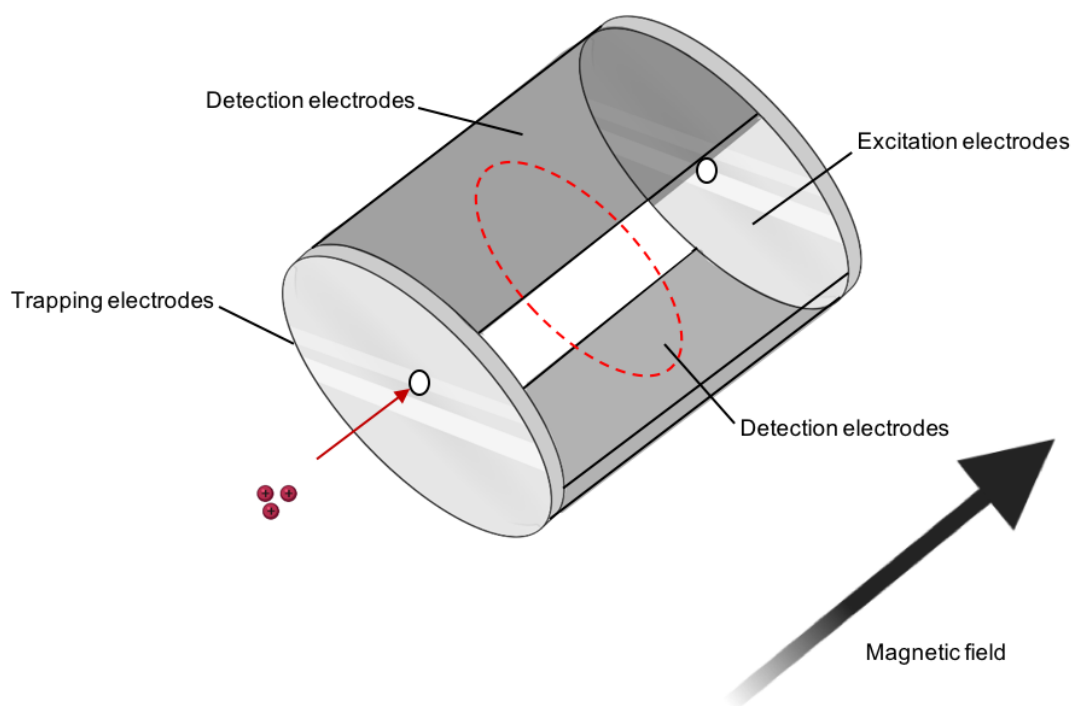


Figure 1.5. Schematic diagram of FT-ICR mass analyzer.

1.6.4 Time-of-flight (TOF) Analyzer

1.6.4.1 Principles of TOF Analyzer

TOF analyzer utilizes an electric field to accelerate ions with the same charge through the same potential energy, which is converted to kinetic energy (Eq. 1.2), and measures the time each ion takes to travel through a fixed length of a field-free flight tube to reach the detector. Ions with different m/z values have different velocities (Eq. 1.3); ions with higher m/z possess lower velocity in comparison to smaller m/z ions, and reach the detector at different times (Eq. 1.4). The m/z values of ions can also be determined based on Eq. 1.5.

$$zeV = \frac{1}{2}mv^2 \quad (\text{Eq. 1.2})$$

$$v = \sqrt{\frac{2zeV}{m}} \quad (\text{Eq. 1.3})$$

$$t = \frac{l}{v} = \frac{l}{\sqrt{\frac{2zeV}{m}}} = \frac{l}{\sqrt{2eV}} \sqrt{\frac{m}{z}} \quad (\text{Eq. 1.4})$$

$$\frac{m}{z} = t^2 \left(\frac{2eV}{l^2} \right) \quad (\text{Eq. 1.5})$$

Here, m and z represent the mass and charge of ions respectively; e is the electron charge; v and t represent the velocity of ions and time for ions to reach the detector respectively; V is the voltage applied; l is the length of the flight tube.

When TOF analyzer is used with MALDI, an ion plume is generated after the irradiation of a pulsed laser beam on the sample surface, and ions with the same m/z ratios may leave the surface with slightly different initial velocities, resulting in a slight difference in final

velocities after the acceleration of ions in the electric field. The time for those ions to travel through the field-free flight tube before reaching the detector is therefore slightly different, leading to peak broadening. Delayed extraction (DE) can be applied to compensate for the flight time shift of ions with the same m/z [101]. With DE, ions are allowed to travel some distance perpendicularly to the sample surface before applying an electric field for the acceleration of ions. As a result, ions with higher initial velocity will move further away from the sample surface compared with those with a lower initial velocity. After the delay, an electric field is applied between the sample plate and the extraction grid. Since the ions with higher initial velocity are closer to the extraction grid, they gain less potential energy compared with those with lower initial velocity and further from the extraction grid. Eventually, ions with the same m/z reach identical velocity before they enter the field-free flight tube.

The inclusion of a reflectron (Figure 1.6b), electrostatic ion mirrors, to which successively higher voltages are applied to reverse the flight direction of the ions, also compensates for the flight time shift of ions with the same m/z and improves the resolution [102]. Ions with higher velocities penetrate deeper into the ion mirrors, while ions with lower velocities penetrate less, and ions will be gradually repelled and finally reach the reflectron detector at the same time. The disadvantage of including a reflectron is the ion loss, so the operator can decide whether to compromise resolution or sensitivity.

1.6.4.2 Applications of TOF Analyzer

The majority of MSI experiments are conducted on TOF since TOF allows the analysis of a wide mass range of molecules with fast analysis time. For instance, MSI experiments that take hours to perform on a TOF instrument could take up to several days to perform on an Orbitrap instrument. Because of the pulsed operation mode of TOF, it works well with MALDI, where pulsed laser beams are irradiated onto the sample.

The combination of two TOF analyzers in a so-called TOF-TOF configuration allows the structural analysis with the TOF system. The first TOF analyzer is employed to select a precursor ion for fragmentation, and the second TOF analyzer is used for rapid fragment separation. Although the TOF analyzer offers rapid analysis and a wide mass range, it has limited mass measurement accuracy and mass resolving power for molecule identification, even with the application of DE and the inclusion of reflectron. TOF instruments can still be used for untargeted small molecule studies but may require additional and complementary analysis with a high mass accuracy and high-resolving power mass spectrometer.

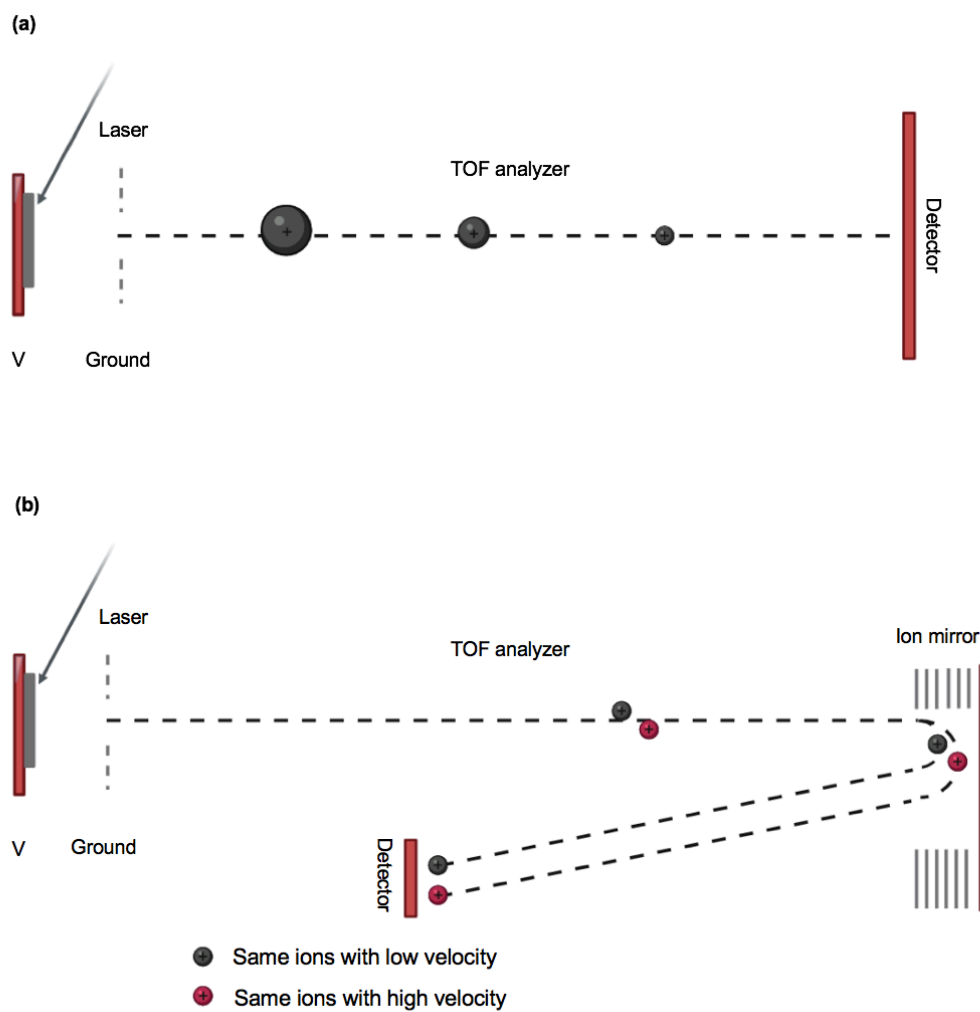


Figure 1.6. Schematic diagram of (a) linear mode and (b) reflectron mode of MALDI TOF mass analyzer.

1.7 MS Detector

The abundance of ions of each separated m/z is determined by the MS detector. Fourier-transform ion cyclotron resonance and Orbitrap analyzers themselves act as MS detectors. TOF analyzers require a detector. Commonly used MS detectors include Faraday cup, electron multiplier (EM), and photomultiplier [103]. After the ions arrive at the surface of the detector, a low ion current generated from the source through the analyzer to the detector is converted to an electric current and then amplified depending on the detector type. A subsequent electronic amplification is performed before the digitalization and processing of electrical signals for data storage [104]. The ideal MS detector should have the following characteristics: unity ion detection efficiency, low or no noise, high stability, simultaneous detection, wide mass-range response, mass-independent response, wide dynamic range, fast response, short recovery time, and high saturation level [103]. Regardless, no single detector meets all characteristics. The selection of detector is determined by the needs of the analyzer; e.g., TOF mass analyzers require rapid response, readout, and recovery, simultaneous ion detection, and a wide and dynamic mass range of detection.

1.8 Thesis Overview

The main goal of this thesis is to develop methods for the imaging of small molecules in rodent animal brains using MALDI MSI (Chapter 2). In addition to method development, this work also demonstrates the applications of MALDI MSI in neuroscience studies by examining the neurotransmitter levels in the rodent brains to reveal the chronic effects of two drugs on neurotransmitters (Chapter 3 and 4).

This thesis begins with an overview of small molecule roles in the brain and small molecule detection methods. Before the detection of small molecules, small molecules must be extracted to isolate them from the media. Commonly used methods for *in vitro* and *in vivo* small molecule extractions are reviewed. Among the analytical techniques for small molecule analyses, MSI is promising in covering a wide range of small molecules while preserving the spatial information of molecules with high sensitivity, high throughput, and high accuracy. Ionization techniques and mass analyzers that are compatible with MSI applications are then reviewed, followed by details regarding sample preparations in MALDI MSI.

A major limitation to the detection of small molecules by MALDI-TOF MSI is the interference of matrix-derived peaks from commonly used organic matrices. Chapter 2 focuses on the method development based on one inorganic nanomaterial, ZnO nanoparticles (NP), as the matrix for the imaging of low molecular weight molecules (LMWM) and neurotransmitters in rodent brain tissues. The optimized method yielded the highest number of analytes detected and the highest quality of image in comparison to

another widely used metal oxide nanomaterial, TiO₂ NP. LC–MS in conjunction with MALDI MSI MS/MS are used for the identification of small molecules.

Chapter 3 and 4 extends the application of MALDI MSI from qualitative analyses of small molecules to quantitative analyses using the methods developed in Chapter 2. MALDI MSI is used to visualize neurotransmitters in tissue sections from various parts of rat brains. Relative quantitation of GABA and glutamate in various brain regions between the drug-treated and vehicle-treated rats was achieved. The effects of nicotine and Δ -9-tetrahydrocannabinol (Δ -9-THC, THC), respectively, subjected to chronic exposure during adolescence on the neurotransmitter abundances in multiple brain regions in both adolescent and adult rats were studied. In combination with the results from our collaborator, a comprehensive understanding of how those two drugs affect the brain during its development from different levels will be reached. Compared to the EP experiments conducted by our collaborator, MALDI MSI offers the advantages of short analysis time and multiple brain region examinations at once. Furthermore, reanalyzing the data is always possible when new processing methods become available once the data is acquired and saved.

Chapter 5 presents the conclusions and future directions on surface modifications of nanoparticles and fabrications of nanomaterials with different morphologies to improve the detection sensitivity of small molecules. Future directions on quantitative MSI improvements through the application of isotope-labelled standards along with normalization against signals from isotope-labelled standards are also presented.

1.9 References

- (1) Svatoš, A. *Trends in biotechnology* **2010**, *28*, 425-434.
- (2) Mergenthaler, P.; Lindauer, U.; Dienel, G. A.; Meisel, A. *Trends in Neurosciences* **2013**, *36*, 587-597.
- (3) Falkowska, A.; Gutowska, I.; Goschorska, M.; Nowacki, P.; Chlubek, D.; Baranowska-Bosiacka, I. *International Journal of Molecular Sciences* **2015**, *16*, 25959-25981.
- (4) Levin, B. E.; Magnan, C.; Dunn-Meynell, A.; Le Foll, C. *Endocrinology* **2011**, *152*, 2552-2557.
- (5) Wang, Y. P.; Lei, Q. Y. *Signal Transduction and Targeted Therapy* **2018**, *3*.
- (6) Medina, C. B.; Mehrotra, P.; Arandjelovic, S.; Perrys, J. S. A.; Guo, Y.; Morioka, S.; Barron, B.; Walk, S. F.; Ghesquiere, B.; Lorenz, U.; Krupnick, A. S.; Ravichandran, K. S. *Nature* **2020**, *580*, 130-135.
- (7) Pinu, F. R.; Beale, D. J.; Paten, A. M.; Kouremenos, K.; Swarup, S.; Schirra, H. J.; Wishart, D. *Metabolites* **2019**, *9*.
- (8) Pandey, R.; Caflisch, L.; Lodi, A.; Brenner, A. J.; Tiziani, S. *Molecular Carcinogenesis* **2017**, *56*, 2355-2371.
- (9) Dumas, M. E.; Davidovic, L. *Journal of Neuroimmune Pharmacology* **2015**, *10*, 402-424.
- (10) Gonzalez-Riano, C.; Garcia, A.; Barbas, C. *Journal of Pharmaceutical and Biomedical Analysis* **2016**, *130*, 141-168.
- (11) Breed, M. D.; J. Moore. *Animal behavior*; Academic press, 2015.
- (12) Daroff, R. B.; Aminoff, M. J. *Encyclopedia of the neurological sciences*; Academic press, 2014.

- (13) Feher, J. J. *Quantitative human physiology: an introduction*; Academic press, 2017.
- (14) Lau, A.; Tymianski, M. *Pflugers Archiv-European Journal of Physiology* **2010**, *460*, 525-542.
- (15) Olloquequi, J.; Cornejo-Cordova, E.; Verdaguer, E.; Soriano, F. X.; Binvignat, O.; Auladell, C.; Camins, A. *Journal of Psychopharmacology* **2018**, *32*, 265-275.
- (16) Franco, R.; Reyes-Resina, I.; Navarro, G. *Biomedicines* **2021**, *9*.
- (17) Pinu, F. R.; Villas-Boas, S. G.; Aggio, R. *Metabolites* **2017**, *7*.
- (18) Li, P.; Bartlett, M. G. *Analytical Methods* **2014**, *6*, 6183-6207.
- (19) Drouin, N.; Rudaz, S.; Schappler, J. *Analyst* **2018**, *143*, 16-20.
- (20) Madikizela, L. M.; Ncube, S.; Chimuka, L. *Chromatographia* **2019**, *82*, 1171-1189.
- (21) Nandi, P.; Lunte, S. M. *Analytica Chimica Acta* **2009**, *651*, 1-14.
- (22) Chefer, V. I.; Thompson, A. C.; Zapata, A.; Shippenberg, T. S. *Current protocols in neuroscience* **2009**, *Chapter 7*, Unit7.1-Unit7.1.
- (23) Bongaerts, J.; De Bundel, D.; Mangelings, D.; Smolders, I.; Heyden, Y. V.; Van Eeckhaut, A. *Journal of Pharmaceutical and Biomedical Analysis* **2018**, *161*, 192-205.
- (24) Navailles, S.; Lagiere, M.; Contini, A.; De Deurwaerdere, P. *Acs Chemical Neuroscience* **2013**, *4*, 680-692.
- (25) Jadhav, S. B.; Khaowroongrueng, V.; Derendorf, H. *Journal of Pharmaceutical Sciences* **2016**, *105*, 3233-3242.
- (26) Lee, G. J.; Park, J. H.; Park, H. K. *Neurological Research* **2008**, *30*, 661-668.
- (27) Zhuang, L. N.; Xia, H. M.; Gu, Y.; Derendorf, H.; Li, Y. Z.; Liu, C. X. *Current Drug Metabolism* **2015**, *16*, 919-931.

- (28) Leegsma-Vogt, G.; Janle, E.; Ash, S. R.; Venema, K.; Korf, J. *Life Sciences* **2003**, *73*, 2005-2018.
- (29) Moscone, D.; Venema, K.; Korf, J. *Medical & Biological Engineering & Computing* **1996**, *34*, 290-294.
- (30) Zhang, Q. H.; Zhou, L. D.; Chen, H.; Wang, C. Z.; Xia, Z. N.; Yuan, C. S. *Trac-Trends in Analytical Chemistry* **2016**, *80*, 57-65.
- (31) Huang, S. M.; Chen, G. S.; Ye, N. R.; Kou, X. X.; Zhu, F.; Shen, J.; Ouyang, G. F. *Analytica Chimica Acta* **2019**, *1077*, 67-86.
- (32) Lendor, S.; Hassani, S. A.; Boyaci, E.; Singh, V.; Womelsdorf, T.; Pawliszyn, J. *Analytical Chemistry* **2019**, *91*, 4896-4905.
- (33) Prasad, B. B.; Srivastava, A.; Tiwari, M. P. *Journal of Chromatography A* **2013**, *1283*, 9-19.
- (34) Cudjoe, E.; Bojko, B.; de Lannoy, I.; Saldivia, V.; Pawliszyn, J. *Angewandte Chemie-International Edition* **2013**, *52*, 12124-12126.
- (35) Daghighian, F.; Sumida, R.; Phelps, M.E. *Journal of nuclear medicine technology* **1990**, *18*, 5-13.
- (36) Ghosh, K. K.; Padmanabhan, P.; Yang, C. T.; Mishra, S.; Halldin, C.; Gulyas, B. *Ejnmri Research* **2020**, *10*.
- (37) Vollenweider, F. X.; Vontobel, P.; Hell, D.; Leenders, K. L. *Neuropsychopharmacology* **1999**, *20*, 424-433.
- (38) Drevets, W. C.; Price, J. C.; Kupfer, D. J.; Kinahan, P. E.; Lopresti, B.; Holt, D.; Mathis, C. *Neuropsychopharmacology* **1999**, *21*, 694-709.

- (39) Solon, E. G.; Schweitzer, A.; Stoeckli, M.; Prideaux, B. *Aaps Journal* **2010**, *12*, 11-26.
- (40) Sato, S.; Chiba, T.; Nishiyama, S.; Kakiuchi, T.; Tsukada, H.; Hatano, T.; Fukuda, T.; Yasoshima, Y.; Kai, N.; Kobayashi, K.; Mizuno, Y.; Tanaka, K.; Hattori, N. *Journal of Neuroscience Research* **2006**, *84*, 1350-1357.
- (41) Solon, E. G. *Cell and Tissue Research* **2015**, *360*, 87-107.
- (42) Burnett, B. *Health Physics* **2004**, *86*, 540-541.
- (43) Carter, M.; Shieh, J. C. *Guide to research techniques in neuroscience*; Academic press, 2015.
- (44) Zeng, H. K.; Sanes, J. R. *Nature Reviews Neuroscience* **2017**, *18*, 530-546.
- (45) Renard, J.; Szkudlarek, H. J.; Kramar, C. P.; Jobson, C. E. L.; Moura, K.; Rushlow, W. J.; Laviolette, S. R. *Scientific Reports* **2017**, *7*.
- (46) Renard, J.; Rosen, L. G.; Loureiro, M.; De Oliveira, C.; Schmid, S.; Rushlow, W. J.; Laviolette, S. R. *Cerebral Cortex* **2017**, *27*, 1297-1310.
- (47) Si, Y.; Lee, H. J. *Current Opinion in Electrochemistry* **2020**, *22*, 234-243.
- (48) Farzin, L.; Shamsipur, M.; Samandari, L.; Sheibani, S. *Microchimica Acta* **2018**, *185*.
- (49) Ou, Y. G.; Buchanan, A. M.; Witt, C. E.; Hashemi, P. *Analytical Methods* **2019**, *11*, 2738-2755.
- (50) Hackshaw, K. V.; Miller, J. S.; Aykas, D. P.; Rodriguez-Saona, L. *Molecules* **2020**, *25*.
- (51) Constantinou, A.; Polizzi, K. M. *Biochemical Society Transactions* **2013**, *41*, 1146-1151.
- (52) Sun, M. X.; Su, Y. Y.; Lv, Y. *Luminescence* **2020**, *35*, 978-988.

- (53) Emwas, A. H.; Roy, R.; McKay, R. T.; Tenori, L.; Saccenti, E.; Gowda, G. A. N.; Raftery, D.; Alahmari, F.; Jaremko, L.; Jaremko, M.; Wishart, D. S. *Metabolites* **2019**, *9*.
- (54) Lee, J. H.; Okuno, Y.; Cavagnero, S. *Journal of Magnetic Resonance* **2014**, *241*, 18-31.
- (55) Faghihi, R.; Zeinali-Rafsanjani, B.; Mosleh-Shirazi, M. A.; Saeedi-Moghadam, M.; Lotfi, M.; Jalli, R.; Irvani, V. *Journal of Medical Imaging and Radiation Sciences* **2017**, *48*, 233-253.
- (56) Ivanisevic, J.; Siuzdak, G. *Journal of Neuroimmune Pharmacology* **2015**, *10*, 391-395.
- (57) Gowda, G. A. N.; Djukovic, D. *Methods in molecular biology (Clifton, N.J.)* **2014**, *1198*, 3-12.
- (58) Liu, X. Y.; Zhou, L. N.; Shi, X. Z.; Xu, G. W. *Trac-Trends in Analytical Chemistry* **2019**, *121*.
- (59) Zhang, X. W.; Li, Q. H.; Xu, Z. D.; Dou, J. J. *Rsc Advances* **2020**, *10*, 3092-3104.
- (60) Ren, J. L.; Zhang, A. H.; Kong, L.; Wang, X. J. *Rsc Advances* **2018**, *8*, 22335-22350.
- (61) Zhao, Y. S.; Li, C. *Current Drug Metabolism* **2015**, *16*, 807-815.
- (62) Ye, H.; Gemperline, E.; Li, L. J. *Clinica Chimica Acta* **2013**, *420*, 11-22.
- (63) Swales, J. G.; Hamm, G.; Clench, M. R.; Goodwin, R. J. A. *International Journal of Mass Spectrometry* **2019**, *437*, 99-112.
- (64) Lalowski, M.; Magni, F.; Mainini, V.; Monogioudi, E.; Gotsopoulos, A.; Soliymani, R.; Chinello, C.; Baumann, M. *Nephrology Dialysis Transplantation* **2013**, *28*, 1648-1656.
- (65) Santagata, S.; Eberlin, L. S.; Norton, I.; Calligaris, D.; Feldman, D. R.; Ide, J. L.; Liu, X. H.; Wiley, J. S.; Vestal, M. L.; Ramkissoon, S. H.; Orringer, D. A.; Gill, K. K.; Dunn,

- I. F.; Dias-Santagata, D.; Ligon, K. L.; Jolesz, F. A.; Golby, A. J.; Cooks, R. G.; Agar, N. Y. R. *Proceedings of the National Academy of Sciences of the United States of America* **2014**, *111*, 11121-11126.
- (66) Ifa, D. R.; Eberlin, L. S. *Clinical Chemistry* **2016**, *62*, 111-123.
- (67) Liebl, H. *Journal of Applied Physics* **1967**, *38*, 5277-5283.
- (68) Castaing, R.; Slodzian, G. *Journal of Microscopie* **1962**, *1*, 1960.
- (69) Caprioli, R. M.; Farmer, T. B.; Gile, J. *Analytical Chemistry* **1997**, *69*, 4751-4760.
- (70) Gamble, L. J.; Anderton, C. R. *Microscopy today* **2016**, *24*, 24-31.
- (71) Fenn, J. B.; Mann, M.; Meng, C. K.; Wong, S. F.; Whitehouse, C. M. *Science* **1989**, *246*, 64-71.
- (72) Takats, Z.; Wiseman, J. M.; Gologan, B.; Cooks, R. G. *Science* **2004**, *306*, 471-473.
- (73) Cooks, R. G.; Ouyang, Z.; Takats, Z.; Wiseman, J. M. *Science* **2006**, *311*, 1566-1570.
- (74) Awad, H.; Khamis, M. M.; El-Aneed, A. *Applied Spectroscopy Reviews* **2015**, *50*, 158-175.
- (75) Kebarle, P.; Verkerk, U. H. *Mass Spectrometry Reviews* **2009**, *28*, 898-917.
- (76) Konermann, L.; Ahadi, E.; Rodriguez, A. D.; Vahidi, S. *Analytical Chemistry* **2013**, *85*, 2-9.
- (77) Parrot, D.; Papazian, S.; Foil, D.; Tasdemir, D. *Planta Medica* **2018**, *84*.
- (78) Nemes, P.; Vertes, A. *Analytical Chemistry* **2007**, *79*, 8098-8106.
- (79) Bartels, B.; Svatos, A. *Frontiers in Plant Science* **2015**, *6*.
- (80) Tanaka, K.; Waki, H.; Ido, Y.; Akita, S.; Yoshida, Y.; Yoshida, T.; Matsuo, T. *Rapid communications in mass spectrometry* **1988**, *2*, 151-153.
- (81) Karas, M.; Hillenkamp, F. *Analytical Chemistry* **1988**, *60*, 2299-2301.

- (82) Knochenmuss, R.; Zenobi, R. *Chemical Reviews* **2003**, *103*, 441-452.
- (83) Knochenmuss, R. *Analyst* **2006**, *131*, 966-986.
- (84) Zenobi, R.; Knochenmuss, R. *Mass Spectrometry Reviews* **1998**, *17*, 337-366.
- (85) Karas, M.; Gluckmann, M.; Schafer, J. *Journal of Mass Spectrometry* **2000**, *35*, 1-12.
- (86) Jaskolla, T. W.; Karas, M. *Journal of the American Society for Mass Spectrometry* **2011**, *22*, 976-988.
- (87) El-Aneed, A.; Cohen, A.; Banoub, J. *Applied Spectroscopy Reviews* **2009**, *44*, 210-230.
- (88) Palmer, A.; Trede, D.; Alexandrov, T. *Metabolomics* **2016**, *12*.
- (89) Bodzon-Kulakowska, A.; Suder, P. *Mass Spectrometry Reviews* **2016**, *35*, 147-169.
- (90) Goodwin, R. J. A.; Dungworth, J. C.; Cobb, S. R.; Pitt, A. R. *Proteomics* **2008**, *8*, 3801-3808.
- (91) Teearu, A.; Vahur, S.; Haljasorg, U.; Leito, I.; Haljasorg, T.; Toom, L. *Journal of Mass Spectrometry* **2014**, *49*, 970-979.
- (92) Smirnov, I. P.; Zhu, X.; Taylor, T.; Huang, Y.; Ross, P.; Papayanopoulos, I. A.; Martin, S. A.; Pappin, D. J. *Analytical Chemistry* **2004**, *76*, 2958-2965.
- (93) Kaletas, B. K.; van der Wiel, I. M.; Stauber, J.; Dekker, L. J.; Guzel, C.; Kros, J. M.; Luider, T. M.; Heeren, R. M. A. *Proteomics* **2009**, *9*, 2622-2633.
- (94) Spraggins, J. M.; Caprioli, R. *Journal of the American Society for Mass Spectrometry* **2011**, *22*, 1022-1031.
- (95) Kompauer, M.; Heiles, S.; Spengler, B. *Nature Methods* **2017**, *14*, 90-96.
- (96) Spivey, E. C.; McMillen, J. C.; Ryan, D. J.; Spraggins, J. M.; Caprioli, R. M. *Journal of Mass Spectrometry* **2019**, *54*, 366-370.

- (97) Niehaus, M.; Soltwisch, J.; Belov, M. E.; Dreisewerd, K. *Nature Methods* **2019**, *16*, 925-931.
- (98) Makarov, A. *Analytical Chemistry* **2000**, *72*, 1156-1162.
- (99) Marshall, A. G.; Hendrickson, C. L.; Jackson, G. S. *Mass Spectrometry Reviews* **1998**, *17*, 1-35.
- (100) Comisarow, M. B. *Hyperfine Interactions* **1993**, *81*, 171-178.
- (101) Barbacci, D. C.; Edmondson, R. D.; Russell, D. H. *International Journal of Mass Spectrometry* **1997**, *165*, 221-235.
- (102) Mamyrin, B. A.; Shmikk, D. V. *Zhurnal Eksperimentalnoi I Teoreticheskoi Fiziki* **1979**, *76*, 1500-1505.
- (103) Koppenaar, D. W.; Barinaga, C. J.; Denton, M. B.; Sperline, R. P.; Hieftje, G. M.; Schilling, G. D.; Andrade, F. J.; Barnes, J. H. *Analytical Chemistry* **2005**, *77*, 418A-427A.
- (104) Greaves, J.; Roboz, J. *Mass spectrometry for the novice*; CRC Press Boca Raton, FL, 2014.

Chapter 2: Imaging of Neurotransmitters and Small Molecules in Brain Tissues Using Laser Desorption/Ionization Mass Spectrometry Assisted with ZnO Nanoparticles

2.1 Introduction

Endogenous low molecular weight molecules (LMWM) in the brain play essential roles in biosynthesis, energy storage, signalling, and defence [1]. Abnormal levels of LMWM, such as amino acids, neurotransmitters, fatty acids, nucleotides, and sugars, were reported in brain cancer [2] and central nervous system disorders [3,4]. For example, studies showed a decrease in the levels of glutamate and γ -aminobutyric acid (GABA) and an increase in glycine in the mouse brains with familial Alzheimer's disease [5]. Decreases in dopamine levels were recorded in Parkinson's disease patients even before clinical symptoms [6]. A comprehensive detection and imaging of endogenous LMWM is therefore very important in the discoveries of biomarkers and therapeutic targets. The mass spectrometry imaging (MSI) technique is particularly ideal for this goal due to its capability in simultaneous identification and spatial imaging of a wide range of biomolecules in tissue sections without the need of contrast agents, dyes, and radioactive and fluorescent labels associated with conventional imaging techniques [7].

MSI can be performed using instruments equipped with desorption electrospray ionization (DESI) or matrix- or nanostructure-assisted laser desorption/ionization (MALDI or NALDI) [8]. DESI is advantageous in producing multiply-charged analyte ions, resulting in higher-quality tandem mass spectra for analyte identification. On the other hand, the focused laser pulses of LDI mass spectrometry (MS) can offer better spatial resolution than DESI. Furthermore, the strategic selection of matrices allows selectivity that can favour or optimize the detection of the analytes of interest [9].

A number of matrices have been reported to facilitate the detection and imaging of lipids, and they include 1,5-diaminonaphthalene (DAN) [10], quercetin [11], dithranol [12], curcumin [13], hydroxyflavones [14], and 3-aminophthalhydrazide (luminol) [15]. Other organic matrices, including 9-aminoacridine (9-AA) [16-19], N-(1-naphthyl) ethylenediamine dihydrochloride (NEDC) [20], N-phenyl-2-naphthylamine (PNA) [21], 1,6-diphenyl-1,3,5-hexatriene (DPH) [22], and 1,1'-binaphthyl-2,2'-diamine (BNDM) [23], have been applied to the imaging of organic acids, amino acids, fatty acids, and other metabolites. The most commonly used matrices α -cyano-4-hydroxycinnamic acid (CHCA) and 2,5-dihydroxybenzoic acid (DHB) have also been applied for the imaging of metabolites from biological tissues [24]. Nevertheless, it is generally more difficult to image analytes below m/z of *ca.* 1000 Da due to hindrance by the background signals of metastable clusters of the matrix molecules [25,26]. Recently, the use of a derivative of CHCA, 3,4-dimethoxycinnamic acid, was reported as a novel matrix with a reduced matrix background for improved imaging of LMWM [27]. The benefit was mostly observed for analytes between m/z 500 and 1000. The imaging of small molecules below 500 Da remains challenging, which include many important neurotransmitters such as glutamate, GABA, dopamine, acetylcholine, serotonin, histamine, epinephrine, and norepinephrine.

On-tissue chemical derivatization targeting predetermined functional groups has been reported to shift the molecular mass of metabolites to higher masses as well as to improve their ionization efficiency [28-34]. Disadvantages of this approach include the difficulty in preserving spatial resolution and/or the integrity of the tissue samples during the

application of the derivatization reagents, low product yields due to incomplete reactions, and system peaks caused by the derivatizing reagents and unwanted side reactions.

Alternatives to the organic matrices, inorganic materials, such as silicon, carbon, metals, and metal oxides, have been investigated as low background matrices for the LDI MSI of LMWM. Examples include the use of silicon nanopost arrays for the imaging of fatty acids and lipids [35] from the mouse brain, the use of carbon-based materials such as graphite for detecting a drug and its metabolites in kidney and liver as well as flavonoids in plants [36-38], and the use of graphene oxide for imaging fatty acids and lipids in mouse brain [39,40]. Interestingly, another application of carbon-based materials in MSI is to map and quantify the carbon-based nanomaterials absorbed in the mouse suborgans [41]. Reports on the use of metals and metal oxides to facilitate LDI MSI of LMWM include gold for metabolites in plants, fingerprints, and mouse brains [42-44]; platinum for metabolites in plants and printed ink [42,45]; silver for fatty acids in mouse retinal, olefins in mouse brains, metabolites in plants, fruits, and human kidney tissues [46-52]; Fe_3O_4 for the imaging of metabolites in zebrafish and plant tissues [53,54]; WO_3 [55] for the imaging of small molecules in plant tissues; and TiO_2 and functionalized TiO_2 for the imaging of metabolites in mouse brains and fingerprints [56-59]. Other inorganic materials like boron nitride nanosheets have also been applied to image metabolites from mouse brains [60].

Recently, Lee and co-workers published a comparison of 13 types of nanoparticles (NP) consisting of carbon-based materials, metals, and metal oxides as matrices for LDI MS (non-imaging) analyses of over 20 standards of small molecules [61]. ZnO was one of the

NP tested, and it resulted in relatively low signal intensities. The best performance was reported with metal oxide NP of Fe_3O_4 and TiO_2 . However, the authors also reported issues with the aggregation of NP in the suspension solvents for both the metal oxides and metals studied. Others also reported the aggregation of metal oxide NP and studied the influence by the suspension solvent, pH, and ionic strength [62,63]. Surface modification with ligands has also been reported to minimize NP aggregation and promote solvent compatibility [64,65], but the stabilizing ligand can often be detached and detected by LDI MS and thus limits the performance of the NP as a low background matrix [59].

Despite the previously reported issues [61], we believe the use of metal oxide NP for LDI MS imaging of small molecules remains an attractive option due to their inexpensive cost and wide availability through commercial sources. Similar to TiO_2 , ZnO exhibits strong absorption in the UV region. ZnO microparticles have been reported as the matrix for LDI MS detection of polar poly(ethylene glycol) 200 and nonpolar methyl stearate [66]. ZnO NP with cationizing agents were found to be useful in detecting low molecular weight organic compounds, such as verapamil hydrochloride, polypropylene glycol 400 (PEG 400), lipids including testosterone and 1,2-dimyristoyl-sn-glycero-3-phosphocholine (DMPC) [67], and small carbohydrates [68]. However, to the best of our knowledge, the application of ZnO NP for LDI MS imaging of LMWM has not been comprehensively evaluated and reported in the literature.

To deposit a homogeneous layer of NP, a dispersion of NP in volatile solvents is typically applied as an aerosol via automated or hand-held sprayers [56,60]. However, the

aforementioned NP aggregation issue can pose a risk of sprayer nozzle clogging. In our experience working with TiO₂ NP, nozzle clogging was often encountered with our automated sprayer during NP deposition. Therefore, we resorted to the use of a hand-held airbrush sprayer with a larger nozzle orifice size. For ZnO NP deposition, we were able to take advantage of the dissolution of ZnO in dilute acids, e.g., 0.1% trifluoroacetic acid (TFA), which can effectively remove and flush out any NP aggregates in the capillaries and nozzle of the sprayer instrument. In contrast, acidic environments promote aggregation of TiO₂ NP, and its dissolution requires concentrated sulfuric acid [69].

In this work, ZnO NP is explored as an alternative to TiO₂ NP for the LDI MS imaging of LMWM. A comprehensive study is presented on the use of ZnO NP in assisting the LDI MS imaging of LMWM in the mouse and rat brain tissue sections. In particular, the neurotransmitters and other LMWM (below 500 Da) detected in the tissue samples using either ZnO or TiO₂ NP were compared to illustrate the similarities and differences in specificity. The results will demonstrate that ZnO NP is an attractive and viable alternative to TiO₂ that offers similar or better performances but also resistance to sprayer nozzle clogging.

2.2 Experimental Section

2.2.1 Chemicals and Supplies

Palmitic acid, myo-inositol, γ -aminobutyric acid (GABA), 4-aminobutyric acid-2,2,3,3,4,4-d₆ (GABA-d₆), spermine, cholesterol, ammonium dihydrogen phosphate, ZnO NP aqueous dispersion (50%, wt) with the particle size less than 100 nm (product no. 721077), α -cyano-4-hydroxycinnamic acid (CHCA), potassium acetate (KOAc), and sodium acetate (NaOAc) were purchased from Sigma-Aldrich (St. Louis, MO). HPLC-grade solvent acetonitrile (ACN) and isopropyl (ISP) were purchased from VMR (Karlsruhe, Germany). Ethanol was purchased from Commercial Alcohols (Toronto, ON, Canada). Methanol (MeOH), TFA, and Optima grade water, ACN, and formic acid were purchased from Fisher Scientific (Waltham, MA). Chloroform was purchased from Merck Group (Darmstadt, Germany). Deionized water (18.2 M Ω ·cm) was purified by the Milli-Q Gradient A10 System (Darmstadt, Germany). Indium-tin oxide (ITO) coated glass slides were purchased from Hudson Surface Technology (Old Tappan, NJ). Rutile and anatase TiO₂ aqueous dispersions (15%, wt), with the particle size between 5–30 nm, were purchased from US Research Nanomaterials (Houston, TX). Based on preliminary experiments, rutile TiO₂ NP (product no. US7060) was found to produce higher signal-to-noise ratios (S/N) and peak resolutions with a cleaner background and thus was selected for this study (data not shown).

2.2.2 Preparations of Solutions

Solutions of GABA, GABA-d₆, myo-inositol, and spermine standards were prepared in deionized water, and solutions of palmitic acid and cholesterol were prepared in ethanol.

CHCA solution was prepared in 6.0 mM ammonium dihydrogen phosphate in ACN/H₂O/TFA (50/50/0.1%, vol) at a concentration of 5.5 mg/mL. DHB solution was prepared in ACN/H₂O/TFA (50/50/0.1%, vol) at a concentration of 20 mg/mL. ZnO NP and TiO₂ NP dispersions were prepared and stored in ACN/H₂O (50/50%, vol) at a concentration of 10 mg/mL. Prior to use, they were ultrasonicated for 5 min and diluted to the optimal concentrations of 1 and 0.5 mg/mL, respectively, for ZnO or TiO₂.

For all MALDI MS analyses of standards, a two-layer matrix deposition method was used. Specifically, 0.6 µL of one of the organic matrix solutions or NP dispersions was placed onto an ITO-coated glass slide and was left to dry at room temperature. A second layer of analyte solution, 0.6 µL of 0.05 mg/mL of GABA, myo-inositol, or 0.6 µL of 0.5 mg/mL of palmitic acid, was deposited on top of the dried matrix or NP. When the analyte standards were analyzed as a mixture, it was deposited at a volume of 0.75 µL, consisting of 75 ng of GABA, 37.5 ng of myo-inositol, 37.5 ng of spermine, 375 ng of palmitic acid, and 375 ng of cholesterol.

For quantitative calibration using GABA-d6, solutions were prepared in deionized water at various concentrations: 2, 5, 10, 20, 50, 100 and 200 µg/mL. The GABA-d6 standard solutions were spotted at a volume of 0.6 µL onto rat brain tissue sections, which resulted in a round spot of approximately 1.5 mm in diameter. After drying the spotted solution at the ambient environment, ZnO NP dispersion at the optimal concentration of 1.0 mg/mL was sprayed on the tissue using a TM-Sprayer (HTX Technologies, Chapel Hill, NC) at

the optimized conditions described below. The regression plot was constructed by plotting the peak heights versus concentrations.

2.2.3 Scanning Electron Microscope Visualization of Dried NP

Deposition of NP was performed by spotting 0.6 μL of ZnO and TiO₂ NP dispersions onto silicon chips attached to carbon stubs, respectively, at the concentrations of 1.0 and 0.5 mg/mL. Images of the dried NP were obtained using a scanning electron microscope (SEM, Zeiss Leo 1540XB FIB, Oberkochen, Germany) operated at 1 kV accelerating voltage.

2.2.4 Preparation of Brain Tissue Sections and Matrix Depositions

Cryostat sectioning of mouse and rat brain tissues was conducted at a thickness of 10 μm and temperature of $-20\text{ }^{\circ}\text{C}$ using a CM 1850 Cryostat (Leica Biosystems, Wetzlar, Germany), and the sections were mounted onto ITO-coated glass slides. Prior to NP deposition, the slides with tissues were dried in a desiccator under vacuum for 30 min at room temperature. ZnO NP dispersion was sprayed onto tissue sections using the TM-Sprayer at the following conditions preoptimized for signal intensity and spatial resolution: 1.0 mg/mL of ZnO NP dispersion in ACN/H₂O (50/50%, vol), flow rate of 0.05 mL/min, nozzle temperature at 65 $^{\circ}\text{C}$, moving nozzle velocity of 1200 mm/min, 32 passes, 3 mm line spacing, and pressure of 10 psi.

After the spraying cycle was finished, the loop and nozzle were cleaned with the cleaning solvent of MeOH/H₂O/TFA (50/50/0.1%, vol) at a flow rate of 0.5 mL/min for 10 min.

The default inline filter with a 2 μm pore size (Valco Instruments, Houston, TX) was replaced regularly for maintenance as recommended by the manufacturer.

For the experiment where the tissue sections were spiked with additional K^+ and Na^+ , the ZnO NP dispersions were prepared in solutions of sodium acetate and potassium acetate at a concentration of 5 mM in ACN/ H_2O (50/50%, vol). The conditions for spraying the ZnO NP dispersion were otherwise unchanged.

The deposition of TiO_2 NP was performed by spraying 0.5 mg/mL dispersion in ACN/ H_2O (50/50%, vol) onto tissue sections using a hand-held sprayer with a 0.5 mm nozzle (K9200, Anest Iwata, Yokohama, Japan). The objective was to apply even coatings of NP as fine droplets of the dispersion on the tissue sections. The pressure of the nebulization inert gas was set at 25 psi, and the airbrush was maintained roughly 10 cm from the glass slide. Approximately 30 to 50 passes of spraying were applied to consume 1.7 mL of NP dispersion.

2.2.5 MALDI MS Analysis and Data Processing

A Sciex 5800 MALDI TOF/TOF mass spectrometer (Framingham, MA) equipped with a 349 nm Nd:YLF laser with a pulse rate of 400 Hz was used to acquire all mass spectra and images. The laser energy was optimized prior to each run based on a balance between peak resolution and S/N. The number of laser shots summed for each mass spectrum was between 500 and 625. For MS mass calibration, 0.75 μL of 5.5 mg/mL CHCA solution

prepared in ACN/H₂O/TFA (50/50/0.1%, vol) was spotted, and the mass calibration was based on: [CHCA – H₂O + H]⁺ at 170.04 Da, [CHCA + H]⁺ at 190.05 Da, [CHCA + Na]⁺ at 212.03 Da, [CHCA – H + 2Na]⁺ at 234.01 Da, and [2CHCA + H]⁺ at 379.09 Da. Data were acquired and processed with Sciex TOF-TOF Series Explorer and Data Explorer.

Images of tissue sections were acquired using Sciex TOF-TOF Imaging software. The number of shots applied for imaging in each pixel was between 30 and 50. Mouse brain tissue sections were imaged at the raster size of 40, 70, and 100 μm, and the rat brain tissue sections were imaged at a raster size of 80 μm. The laser intensity was optimized based on the number of signals from the *m/z* range of 50 to 500 Da, peak resolution, and S/N. MSiReader (1.02), developed by North Carolina State University [70], was used to process and display ion distributions within the tissue sections. The *m/z* list was generated from the mass spectrum summed from all signals acquired from the entire brain section.

2.2.6 Sample Preparations for Liquid Chromatography–Mass Spectrometry (LC–MS)

A hundred and eleven milligrams of frozen brain samples were homogenized in 400 μL of prechilled MeOH/H₂O (50/50%, vol) using a tissue grinder pestle in a 1.5 mL microtube, followed by centrifugation (Sorvall Legend Micro 21, Thermo Scientific, Waltham, MA) at 13 000 x *g* for 20 min at 4 °C. A hundred microlitres of the supernatant was transferred into another microtube and then spun in a vacuum concentrator for 3 hours at 43 °C until dry. The aqueous extracts of the tissue samples were finally reconstituted in 200 μL of the

solvent mixture of MeOH/H₂O (50/50%, vol), after centrifugation for 20 min at 13 000 x g and 4 °C. Following the aqueous extraction, the residual pellet was homogenized in 400 µL of prechilled CHCl₃/MeOH (75/25%, vol) using the tissue grinder pestle in the 1.5 mL microtube, followed by centrifugation at 13 000 x g for 20 min at 4 °C. A hundred and fifty microlitres of the supernatant was transferred into another microtube and was allowed to evaporate at room temperature in a fume hood overnight. The organic extracts of the tissue samples were reconstituted in 25 µL of the solvent mixture of H₂O/ACN/ISP (25/25/50%, vol) after centrifugation for 10 min at 5000 x g and 4 °C.

2.2.7 LC–MS Analysis and Data Processing

LC–MS/MS analysis was performed with an Agilent 1290 HPLC system coupled to a Q-Exactive Quadrupole Orbitrap mass spectrometer (Thermo Scientific, Waltham, MA). Chromatographic conditions consisted of an Eclipse Plus C18 RRHD column (2.1 × 100 mm, 1.8 µm; Agilent Technologies, Santa Clara, CA) maintained at 35 °C using an established gradient program. The mobile phase consisted of water with 0.1% formic acid (A) and acetonitrile with 0.1% formic acid (B). Mobile phase B was held at 0% B for 0.5 min before increasing to 100% over 3.5 min and held at 100% for 2.5 min before returning to 0% B over 0.5 min. The aqueous and organic extracts of brain metabolites were injected with a volume of 5 µL each and separated at a flow rate of 0.3 mL/min.

Heated electrospray ionization was used in the positive ionization mode with the following settings: capillary voltage, 3.9 kV; capillary temperature, 400 °C; sheath gas, 17 units; auxiliary gas, 8 units; probe heater temperature, 450 °C; S-Lens RF level, 50%. MS data

were acquired using untargeted data-dependent acquisition (DDA) that included a full MS scan at a resolution of 35 000, with a scan range of 70–1000 m/z ; automatic gain control (AGC) target, 1×10^6 ; a maximum injection time (IT) of 128 ms. The five highest intensity ions were selected from each full scan for MS/MS analysis using a 1.2 Da isolation window and were acquired using the following conditions: resolution, 17 500; AGC target, 1×10^6 ; max IT, 64 ms; stepped normalized collision energy (NCE), 20/40; intensity threshold, 2×10^5 ; dynamic exclusion, 7 s. Raw data files were imported into MZmine, and the m/z peak list was exported.

2.2.8 Metabolite Identification

For chemical identification, the MALDI MSI experimental m/z values were searched at 50 ppm against a peak list created from an LC–MS analysis of brain samples. The experimental m/z values from LC–MS were matched at 5 ppm against the theoretical m/z values from METLIN Metabolomics Database (<https://metlin.scripps.edu>) and Mouse Multiple Tissue Metabolome Database (<http://mmdmdb.iab.keio.ac.jp>). The identification of the MALDI MSI peaks was then verified by the isotope peak patterns from carbon and potassium. For signals with intensity above 1000, MS/MS was carried out on the tissue samples for structural confirmation.

2.3 Results and Discussion

2.3.1 Background Signals in ZnO NP-assisted LDI MS Analysis

To examine the chemical background of ZnO NP, the LDI mass spectra were recorded individually for myo-inositol and GABA in the positive ion mode, and for palmitic acid in the negative ion mode (Appendix I). In both positive and negative ion modes, ZnO NP produced very few background signals in the low mass region (ca. 120 to 400 Da). As expected, palmitic acid was detected as the deprotonated ion in the negative ion mode. In the positive mode, myo-inositol and GABA were mainly detected as adducts of Na^+ and K^+ and not the protonated ion, $[\text{M} + \text{H}]^+$.

2.3.2 Comparison for LMWM Analysis Using ZnO NP, TiO_2 NP, DHB, and CHCA as Matrices

The ionization efficiency of analytes depends on the concentration of matrices used in MALDI MS, and thus the experiments began with determining the optimal NP concentration in the dispersion with a mixture of five LMWM standards: GABA, myo-inositol, spermine, palmitic acid, and cholesterol. The S/N and peak resolution of the above five standards were recorded using the two-layer deposition method described in the Experimental Section with varying NP concentrations in the ZnO or TiO_2 dispersions (from 0.1 to 10 mg/mL). After comparing the results, the optimal concentrations were found to be 1.0 and 0.5 mg/mL, respectively. The performance of both NPs in LMWM analysis was evaluated with the above five standards, along with DHB and CHCA as matrices for comparison. The optimized mass spectra are shown in Figure 2.1. The results generally agreed with the literature; namely, the NP of metal oxides provided superior LDI MS

detection of LMWM and cleaner matrix backgrounds than the organic matrices. With NP of metal oxides, the five standards were mainly detected as adducts of Na^+ and K^+ and not the protonated ion, $[\text{M} + \text{H}]^+$. When using conventional MALDI matrices, signals of the protonated ions can be enhanced by acidifying the sample, e.g., with formic acid or TFA. It is acknowledged that sample acidification is incompatible with ZnO and TiO_2 NP, respectively due to NP dissolution and aggression. Nevertheless, results in a later section will demonstrate that high-quality images of LMWM can be obtained from Na^+ or K^+ adducts, and thus the absence of the $[\text{M} + \text{H}]^+$ signals is not necessarily a limiting factor.

2.3.3 Quantitative Analysis in ZnO NP-assisted LDI MS

To illustrate the capabilities of quantitative analysis of LMWM using ZnO NP-assisted LDI MS, the dynamic range of ZnO NP-assisted LDI MS was estimated using deuterated GABA (GABA-d6, m/z 148.06) that was spotted on brain tissues. The signal from $[\text{GABA-d6} + \text{K}]^+$ at m/z 148.08 does not interfere with endogenous signals naturally present at the same m/z within the brain tissues or background from the matrix. Solutions of deuterated GABA-d6 at various concentrations were spiked on the same region of serial tissue sections of a rat brain. Triplicate spots for each concentration were deposited, and three spectra from each spot were acquired.

The resulting calibration curve is shown in Figure 2.2. A non-linear curve was observed under the wide concentration range studied ($y = -1.67 x^2 + 613.25 x + 1600$, $R^2 = 0.996$), but good linearity was observed up to 50 $\mu\text{g/mL}$ ($y = 583.9 x + 1442$, $R^2 = 0.991$), based on signals from standards deposited on tissue. The limit of quantitation ($\text{S/N} = 10$) was

found to be 0.5 $\mu\text{g/mL}$ for GABA-d6, based on standards deposited off tissue. This corresponded to approximately 170 pg/mm^2 in density, calculated based on a spot diameter of 1.5 mm and a spot volume of 0.6 μL . The overall results demonstrate the feasibility of quantitation on tissue sections with our ZnO NP-assisted LDI MS technique.

2.3.4 Stability of NP Dispersion Against Aggregation

The particle size specified by the suppliers was described as “5–30 nm” for the TiO_2 NP acquired and “less than 100 nm” for the ZnO NP. The SEM images of dried spots of NP are shown in Figure 2.3. Under the lower magnification examined, these nanometer-size particles should not be visible without aggregation. However, μm -sized aggregates were visible in the images. In the images acquired at higher magnification, clusters of NP were clearly observed. Based on the size and density of these aggregates, a greater extent of aggregation was evident with TiO_2 NP. We speculated that the ZnO NP acquired for this work have lower surface energy [71] when compared to the TiO_2 NP, making it less susceptible to aggregation. Overall, the SEM results supported our observation that nozzle clogging can occur due to NP aggregation, and thus the ability to dissolve ZnO NP with dilute acid solutions is crucial in maintaining high run-to-run reproducibility.

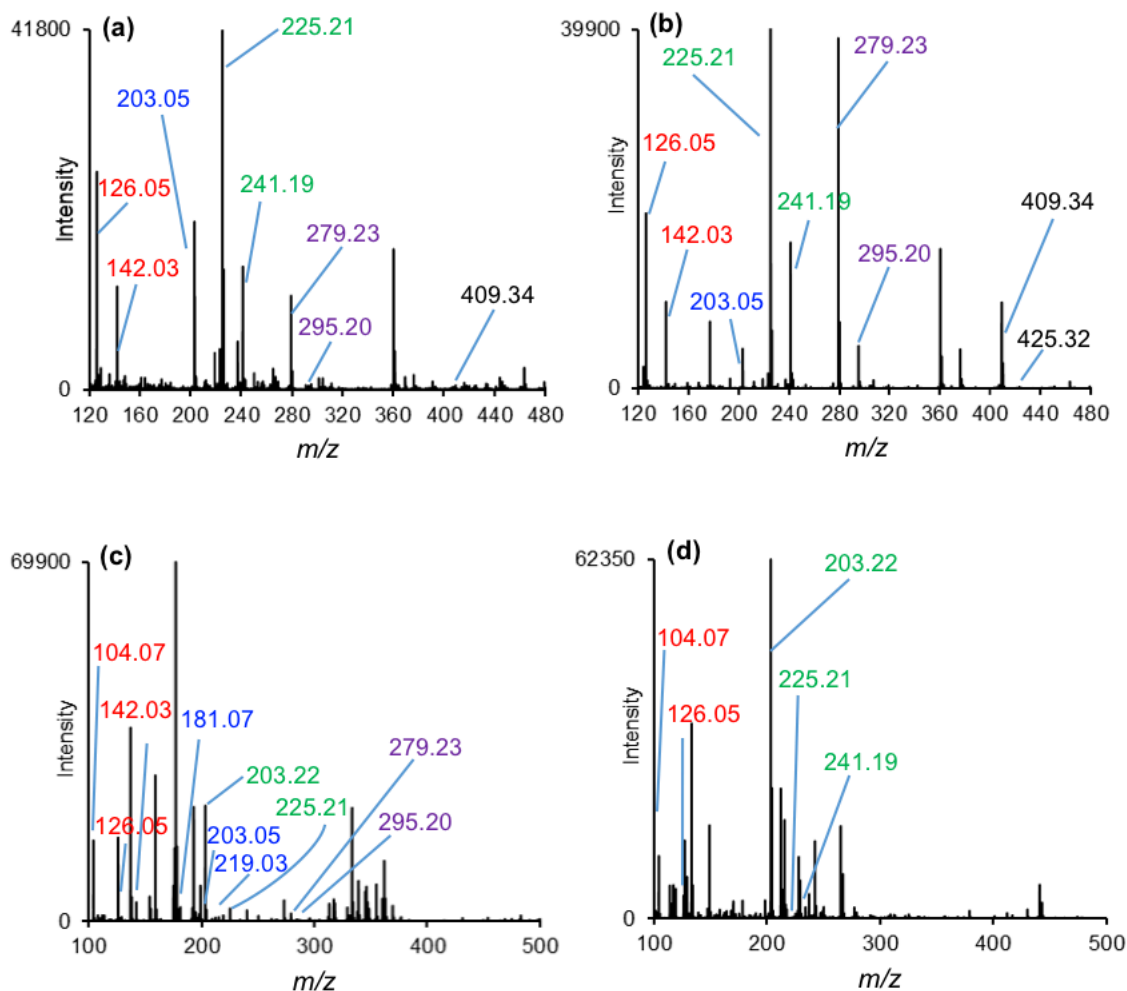


Figure 2.1. Positive-ion mass spectra of a mixture of γ -aminobutyric acid (**GABA**, 75.0 ng; $[M + H]^+$, m/z 104.07; $[M + Na]^+$, m/z 126.05; $[M + K]^+$, m/z 142.03), **myo-inositol** (37.5 ng; $[M + H]^+$, m/z 181.07; $[M + Na]^+$, m/z 203.05; $[M + K]^+$, m/z 219.03), **spermine** (37.5 ng; $[M + H]^+$, m/z 203.22; $[M + Na]^+$, m/z 225.21; $[M + K]^+$, m/z 241.19), **palmitic acid** (375 ng; $[M + Na]^+$, m/z 279.23; $[M + K]^+$, m/z 295.20), and **cholesterol** (375 ng; $[M + Na]^+$, m/z 409.34; $[M + K]^+$, m/z 425.32) with (a) ZnO NP, (b) TiO₂ NP, (c) DHB, and (d) CHCA in the mass region 120–500 on an ITO glass slide.

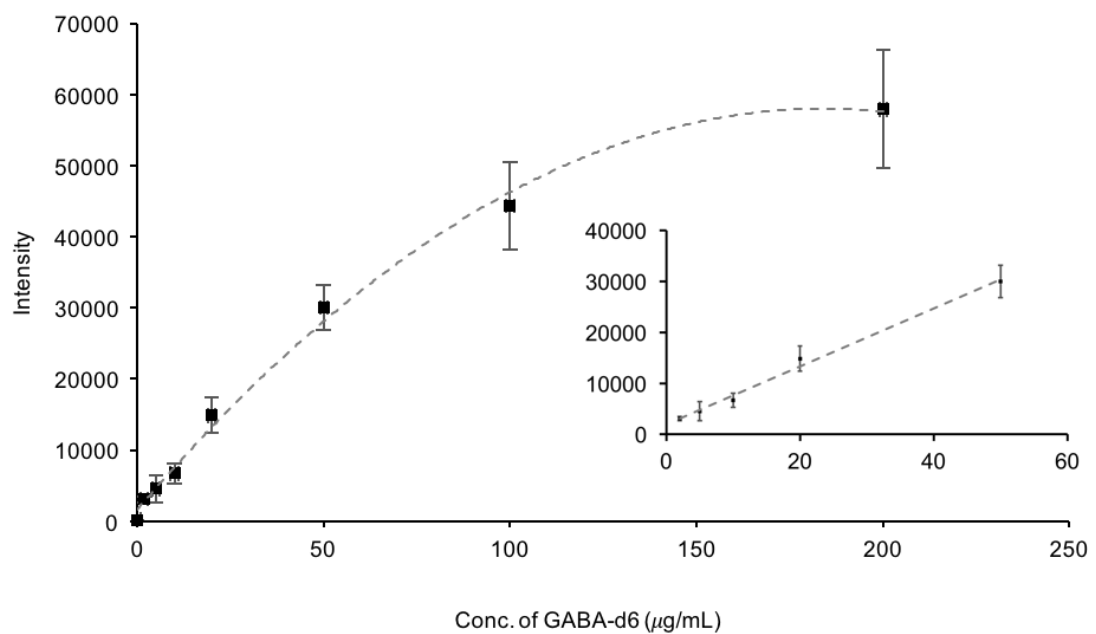


Figure 2.2. Calibration curve of GABA-d6 signals measured by ZnO NP-assisted LDI MS. Inlay shows the linear range of the calibration curve. The GABA-d6 concentration refers to that of the standard solution spiked on rat brain tissue sections. Error bars show +/- the standard deviation from 9 replicate measurements.

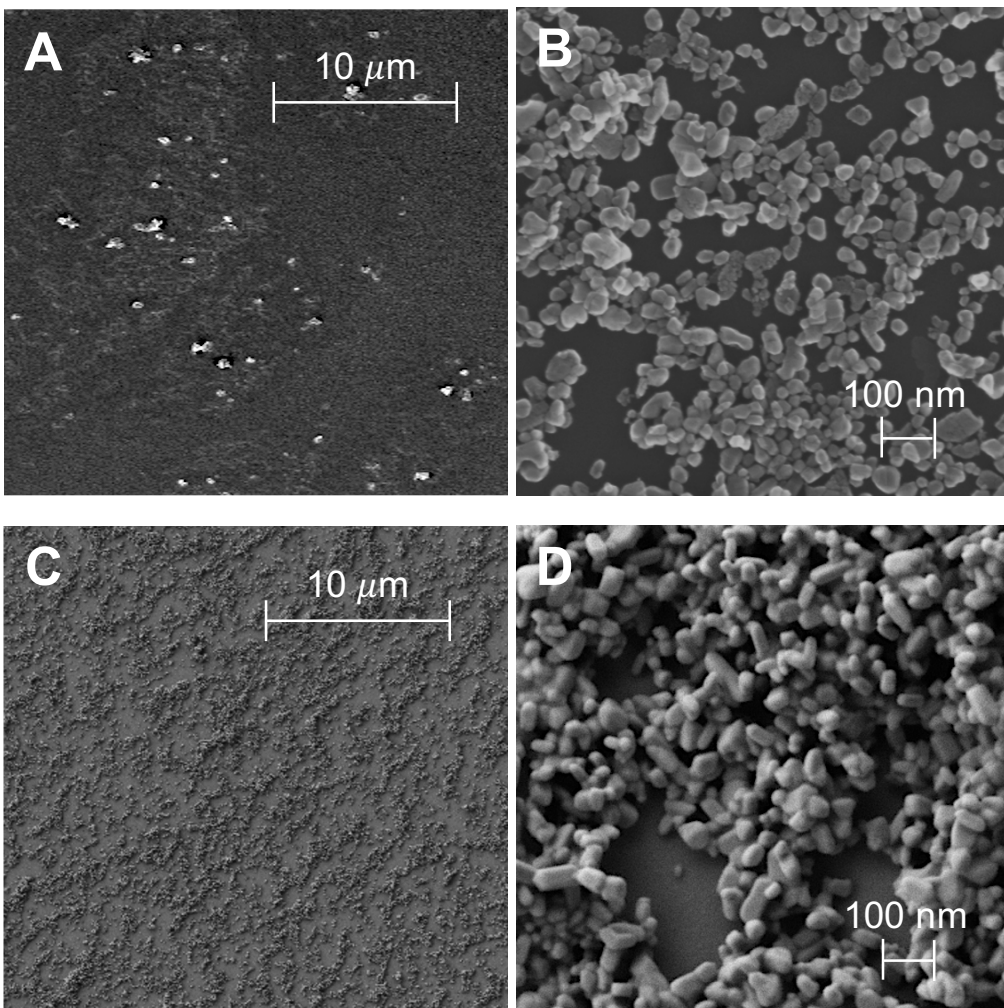


Figure 2.3. SEM (scanning electron microscope) images of (A, B) ZnO and (C, D) TiO₂ NP, with different magnifications. Suspensions were prepared in 1:1 mixture of acetonitrile and water, deposited on silicon and dried in ambient conditions.

2.3.5 ZnO NP-assisted LDI MSI for Investigation of Mouse and Rat Brain Tissues

Rodent models are the most commonly used in neuroscience research involved animals, and thus, a large number of MS imaging experiments were conducted on mouse and rat brains, using both the sagittal and coronal sections. The identities of the detected ions were determined by searching against the METLIN Metabolomics Database, Mouse Multiple Tissue Metabolome Database, and our LC–MS data that confirmed the presence of the identified LMWM in our samples. MS/MS was carried out on the brain tissue sections for signals with intensity above 1000 for structural confirmation. A complete list of LMWM detected by our ZnO NP-assisted LDI MSI technique from the sagittal section of mouse and rat brains is presented (Table 2.1). The list was grouped by functional groups: amino acids, neurotransmitters, alkaloids, purine, sterol lipids, fatty acids (FA), peptides, organic acids, and others. As indicated earlier, the LMWM are detected as adducts of K^+ or Na^+ ions. In total, signals from 56 compounds were found from the mouse brain section, and 60 compounds were found from the rat brain section. Among these, 11 LMWM were found only in the mouse brain sample, 15 LMWM were found only in the rat brain sample, and 45 LMWM were observed in both.

To illustrate the visual quality of the resulting images, a selection of ion images with relatively strong signal intensities are presented, from the sagittal section of a mouse brain (Figure 2.4) and the coronal sections of a rat brain at different anatomical points (Figure 2.5). In general, the images exhibit very high-quality spatial resolution and dynamic range in differentiating changes in analyte concentrations within the various parts of the brain.

For example, in Figure 2.4, the cerebellum structure can be clearly observed in ion images of cytosine (m/z 150.00). In addition, certain metabolites were found in localized parts of the brain: glycine (m/z 113.98) in the hindbrain, an unidentified molecule (m/z 184.09) in white matter regions, and other abundant signals in grey matter regions. In Figure 2.5, the dynamic range of the selected analytes was illustrated from the coronal images, where different MS signal intensities were observed at three different Bregma positions.

In addition to the ion images presented in Figures 2.4 and 2.5, many other molecules were detected from the rat and mouse brain tissue analyzed, and their ion images from the sagittal mouse brain were provided in Appendix I. Imaging in the negative ion mode with ZnO NP was also conducted. The most intense signals observed were mainly from fatty acids as $[M - H]^-$ ions, and the images are shown in Appendix I. Since the number of LMWM detected in the positive ion mode far exceeded that of the negative ion mode, our discussion will focus on the positive ion mode results from this point forward.

Table 2.1. Information of Ions with MW below 500 Da Detected in the Sagittal Sections of Mouse and Rat Brains with ZnO NP-assisted LDI MSI.

classification	measured <i>m/z</i>		calculated <i>m/z</i>	tentative assignment			
	mouse	rat		ion form	compound	formula	
amino acids	113.98	113.97	114.00	[M + K] ⁺	glycine	C ₂ H ₅ NO ₂	
	128.00	127.99	128.01	[M + K] ⁺	alanine ¹	C ₃ H ₇ NO ₂	
	144.00	144.00	144.01	[M + K] ⁺	serine ¹	C ₃ H ₇ NO ₃	
	154.06	154.04	154.06	[M + Na] ⁺	creatine ¹	C ₄ H ₉ N ₃ O ₂	
	170.03	170.03	170.03	[M + K] ⁺			
	156.05	156.02	156.04	[M + K] ⁺	valine	C ₅ H ₁₁ NO ₂	
	158.03	158.00	158.02	[M + K] ⁺	threonine	C ₄ H ₉ NO ₃	
	159.98		159.98	[M + K] ⁺	cysteine	C ₃ H ₇ NO ₂ S	
	167.99	167.99	168.01	[M + K] ⁺	pyroglutamic acid	C ₅ H ₇ NO ₃	
	169.06	169.04	169.06	[M + Na] ⁺	glutamine ¹	C ₅ H ₁₀ N ₂ O ₃	
	185.03	185.02	185.03	[M + K] ⁺			
	185.99	186.00	186.02	[M + K] ⁺	glutamic acid ¹	C ₅ H ₉ NO ₄	
		188.00	188.01	[M + K] ⁺	methionine	C ₅ H ₁₁ NO ₂ S	
	194.01	194.01	194.03	[M + K] ⁺	histidine	C ₆ H ₉ N ₃ O ₂	
	196.00	195.99	196.00	[M + K] ⁺	amino-muconic acid	C ₆ H ₇ NO ₄	
	neurotransmitters	213.06		213.08	[M + K] ⁺	arginine	C ₆ H ₁₄ N ₄ O ₂
		220.02		220.04	[M + K] ⁺	tyrosine	C ₉ H ₁₁ NO ₃
142.03		142.00	142.03	[M + K] ⁺	γ-aminobutyric acid (GABA) ¹	C ₄ H ₉ NO ₂	
192.03		192.03	192.04	[M + K] ⁺	dopamine ¹	C ₈ H ₁₁ NO ₂	
208.01		208.01	208.04	[M + K] ⁺	norepinephrine	C ₈ H ₁₁ NO ₃	
		206.08	206.08	[M + Na] ⁺	epinephrine	C ₉ H ₁₃ NO ₃	
		222.05	222.05	[M + K] ⁺			
alkaloids	306.07	306.06	306.06	[M + K] ⁺	adenosine	C ₁₀ H ₁₃ N ₅ O ₄	
		111.08	111.09	[M + Na] ⁺	putrescine	C ₄ H ₁₂ N ₂	
	161.01	160.99	161.01	[M + K] ⁺	nicotinamide	C ₆ H ₆ N ₂ O	
	168.14	168.13	168.15	[M + Na] ⁺	spermidine	C ₇ H ₁₉ N ₃	
	225.20		225.21	[M + Na] ⁺	spermine ¹	C ₁₀ H ₂₆ N ₄	
purine	241.19	241.17	241.18	[M + K] ⁺			
	174.02	174.00	174.02	[M + K] ⁺	adenine	C ₅ H ₅ N ₅	
pyrimidine	174.99	174.99	175.00	[M + K] ⁺	hypoxanthine	C ₅ H ₄ N ₄ O	
		150.97	150.99	[M + K] ⁺	uracil	C ₄ H ₄ N ₂ O ₂	
sterol lipids	409.35	409.35	409.34	[M + Na] ⁺	cholesterol	C ₂₇ H ₄₆ O	
	425.32	425.33	425.32	[M + K] ⁺			
	423.31	423.33	423.32	[M + Na] ⁺	OH-7-dehydrocholesterol	C ₂₇ H ₄₄ O ₂	
fatty acids	277.19	277.19	277.21	[M + Na] ⁺	FA(16:1)	C ₁₆ H ₃₀ O ₂	
	279.23		279.23	[M + Na] ⁺	FA(16:0)	C ₁₆ H ₃₂ O ₂	
	295.19	295.20	295.20	[M + K] ⁺			
	305.24	305.23	305.25	[M + Na] ⁺	FA(18:1)	C ₁₈ H ₃₄ O ₂	
	321.22	321.22	321.22	[M + K] ⁺			
	307.26	307.25	307.26	[M + Na] ⁺	FA(18:0)	C ₁₈ H ₃₆ O ₂	
	323.24	323.23	323.24	[M + K] ⁺			
	327.23	327.22	327.23	[M + Na] ⁺	FA(20:4)	C ₂₀ H ₃₂ O ₂	
	343.20	343.20	343.20	[M + K] ⁺			
	337.23		337.21	[M + K] ⁺	hydroxy-oleic acid	C ₁₈ H ₃₄ O ₃	
	351.23	351.23	351.23	[M + Na] ⁺	FA(22:6)	C ₂₂ H ₃₂ O ₂	
	367.21	367.20	367.20	[M + K] ⁺			
	363.29		363.27	[M + K] ⁺	FA(21:1)	C ₂₁ H ₄₀ O ₂	
	371.24		371.24	[M + K] ⁺	FA(22:4)	C ₂₂ H ₃₆ O ₂	
peptides	277.04	277.06	277.06	[M + K] ⁺	Gly-Tyr	C ₁₁ H ₁₄ N ₂ O ₄	

(table continued on next page)

classification	measured <i>m/z</i>		calculated <i>m/z</i>	tentative assignment			
	mouse	rat		ion form	compound	formula	
organic acids		139.00	139.00	[M + Na] ⁺	fumaric acid	C ₄ H ₄ O ₄	
		145.00	144.98	144.99	[M + K] ⁺	glyceric acid	C ₃ H ₆ O ₄
		155.01	155.01	155.01	[M + K] ⁺	levulinic acid	C ₅ H ₈ O ₃
			156.97	156.99	[M + K] ⁺	succinic acid	C ₄ H ₆ O ₄
			172.98	172.99	[M + K] ⁺	malic acid	C ₄ H ₆ O ₅
		187.02	187.02	187.02	[M + K] ⁺	cinnamic acid	C ₉ H ₈ O ₂
		189.05	189.01	189.03	[M + K] ⁺	3-phenylpropionic acid	C ₉ H ₁₀ O ₂
		197.00	196.98	197.00	[M + Na] ⁺	aconitic acid	C ₆ H ₆ O ₆
		212.98	212.98	212.98	[M + K] ⁺		
	others		104.11	104.11	104.11	M ⁺	choline ¹
			112.00	112.00	[M + Na] ⁺	oxamic acid	C ₂ H ₃ NO ₃
		136.04		136.05	[M + Na] ⁺	creatinine ¹	C ₄ H ₇ N ₃ O
		152.02	152.01	152.02	[M + K] ⁺		
		146.99	146.98	146.98	[M + Na] ⁺	phosphonoacetaldehyde ¹	C ₂ H ₅ O ₄ P
		162.97	162.96	162.96	[M + K] ⁺		
		150.00		150.01	[M + K] ⁺	cytosine	C ₄ H ₅ N ₃ O
		163.96	163.96	163.98	[M + K] ⁺	taurine	C ₂ H ₇ NO ₃ S
		164.95	164.96	164.96	[M + K] ⁺	isethionic acid	C ₂ H ₆ O ₄ S
		192.98		192.99	[M + Na] ⁺	dihydroxyacetone phosphate	C ₃ H ₇ O ₆ P
			200.08	200.07	[M + K] ⁺	carnitine	C ₇ H ₁₅ NO ₃
		203.05	203.04	203.05	[M + Na] ⁺	myo-inositol ¹	C ₆ H ₁₂ O ₆
		219.02	219.02	219.03	[M + K] ⁺		
		214.00	214.00	214.01	[M + K] ⁺	N-acetylaspartic acid	C ₆ H ₉ NO ₅
			223.01	223.04	[M + K] ⁺	3-methoxy-4-hydroxyphenylglycol ¹	C ₉ H ₁₂ O ₄
			228.01	228.03	[M + K] ⁺	N-acetylglutamic acid ¹	C ₇ H ₁₁ NO ₅
			230.02	230.02	[M + K] ⁺	5-hydroxyindoleacetic acid	C ₁₀ H ₉ NO ₃
		236.08	236.08	236.07	[M + K] ⁺	metanephine	C ₁₀ H ₁₅ NO ₃
			250.05	250.05	[M + K] ⁺	methoxytyrosine	C ₁₀ H ₁₃ NO ₄
		251.98	251.98	251.97	[M + K] ⁺	3-indoxyl sulfuric acid	C ₈ H ₇ NO ₄ S
			261.03	261.03	[M + K] ⁺	cystathionine	C ₇ H ₁₄ N ₂ O ₄ S
			283.02	283.03	[M + K] ⁺	uridine	C ₉ H ₁₂ N ₂ O ₆
		296.07		296.07	[M + K] ⁺	glycerophosphoryl-choline	C ₈ H ₂₀ NO ₆ P
		298.97		298.99	[M + K] ⁺	fructose 6-phosphate	C ₆ H ₁₃ O ₉ P
		301.00	301.01	301.01	[M + K] ⁺	sorbitol 6-phosphate	C ₆ H ₁₅ O ₉ P
		307.06	307.05	307.04	[M + K] ⁺	inosine	C ₁₀ H ₁₂ N ₄ O ₅
			330.07	330.07	[M + Na] ⁺	glutathione	C ₁₀ H ₁₇ N ₃ O ₆ S
		340.02	340.02	[M + K] ⁺	N-acetylglucosamine-1-phosphate	C ₈ H ₁₆ NO ₉ P	

¹Molecule assignment was verified by MS/MS.

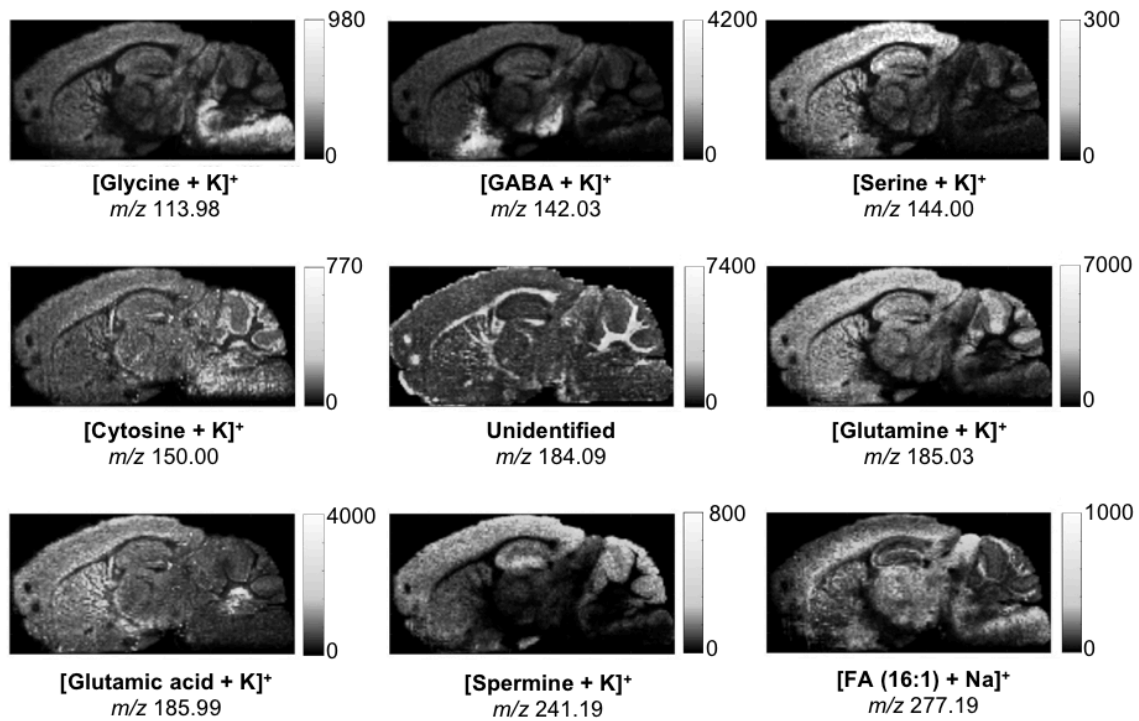


Figure 2.4. Ion images of the sagittal section of a mouse brain acquired with ZnO NP-assisted LDI MSI at a raster size of 70 μm .

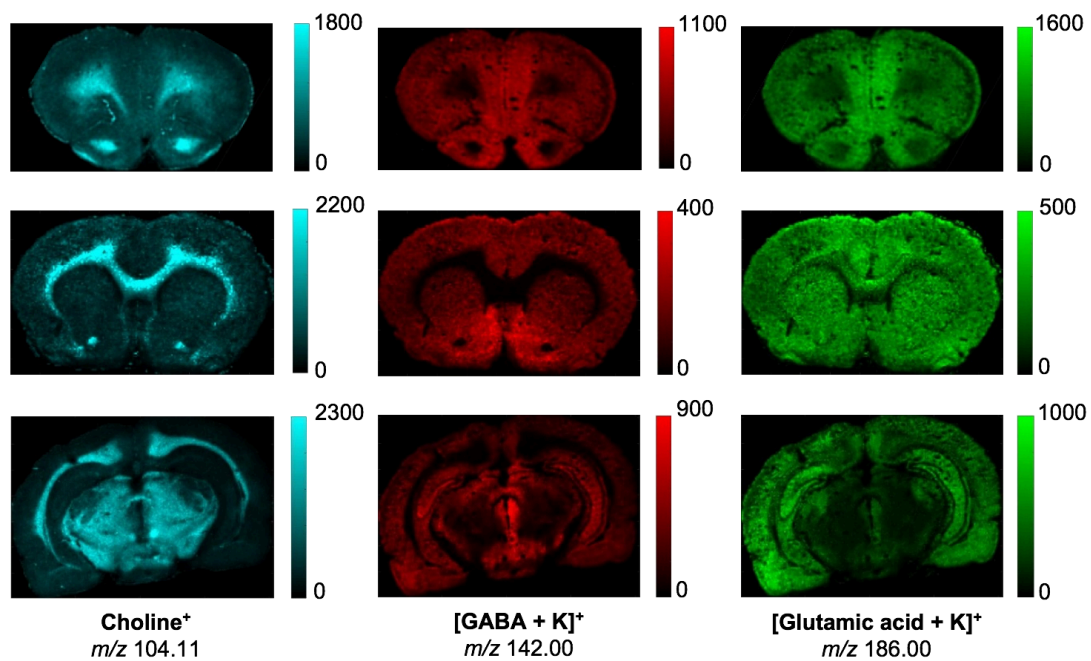


Figure 2.5. Ion images of coronal sections of a rat brain acquired with ZnO NP-assisted LDI MSI (top to bottom: Bregma +3.00 mm, +2.04 mm, and -6.00 mm; Paxinos and Watson Atlas; raster size of 80 μ m).

2.3.6 Comparison for Imaging of LMWM in Mouse Brain Tissues Using ZnO NP and TiO₂ NP

We compared the identities of detected ions in the coronal sections of mouse brains using either ZnO NP- or TiO₂ NP-assisted LDI MSI, as listed in Table 2.2. Again, the identification was independently confirmed by LC-MS. A Venn diagram is shown in Figure 2.6. Of the identified LMWM, 50 were common to both ZnO and TiO₂, while 13 and 10 were unique to TiO₂ and ZnO respectively. Slightly higher numbers of amino acids, neurotransmitters, and dipeptides were observed with TiO₂. However, in general, similar signals below m/z 300 were observed with ZnO and TiO₂ (Figure 2.7). Molecules identified with ZnO NP have amine groups, carboxylic groups, and hydroxyl groups, which is in agreement with the literature [72], but we are unable to draw any definitive conclusions of unique specificity between the two metal oxides studied.

In the report by Lee and co-workers examining the use of nanoparticles of various metal oxides for LDI MS analysis of small molecules [61], the performance of TiO₂ NP was found to be one of the best, while that of the ZnO NP was significantly inferior. However, in our experience, both ZnO NP and TiO₂ NP exhibited superior performances, with ZnO NP being less prone to sprayer nozzle clogging. We attribute the different observations between our work and that of ref. [61] to two possible factors. First, different sources of NP were used. Variations in NP size, crystal phase, shapes, and surface modifications may contribute to the different performances in LDI MS [73-77]. Second, the comparison was conducted with purified standards in ref. [61], while in this work, we performed MSI on biological tissues with the presence of endogenous salt ions. Without having to worry about

nozzle clogging, we were able to reliably apply ZnO NP onto the tissue samples with an automated sprayer. Compared to the use of a hand-held airbrush for TiO₂ NP, an enhancement in spatial resolution was clearly observed with ZnO NP (Figure 2.8). Delocalization was evident in the images acquired with TiO₂ NP due to the lateral diffusion of analytes during the relatively wet spraying conditions with an airbrush.

2.3.7 Comparison of NP-assisted LDI MSI with Other Imaging Studies

Additional to examining the experimental data collected for this work, we also compared our data with previously published reports in the literature as a quality control of our skills and the conditions of our equipment. In Appendix I, the list of 63 LMWM detected with TiO₂ NP (presented in Table 2.2) is compared to a list of 22 molecules reported also using TiO₂ NP by Shrivastava *et al.* [56], and a list of 38 molecules reported by Wu *et al.* using dopamine-modified TiO₂ monolith [59]. Based on the higher number of analytes detected in our work, we are very confident with the quality of our data presented in this work.

Furthermore, we searched the literature for reports of LDI MS imaging of neurotransmitters to the best of our abilities and compiled our findings in Appendix I. This table lists 16 neurotransmitters to which MS imaging data had been reported in the literature. It is noteworthy that many of the previous imaging work required chemical derivatization of the analytes.

Table 2.2. List of Small Molecules Detected in Mouse Coronal Brain Sections in the Positive-ion Mode Using ZnO NP- and TiO₂ NP-assisted LDI MSI (Bregma -2.46mm; Paxinos and Watson Atlas).

measured <i>m/z</i>	compound	detected ions		classification
		ZnO	TiO ₂	
99.00 113.97	glycine		[M + Na] ⁺ [M + K] ⁺	amino acids
127.98 127.99	alanine ¹	[M + K] ⁺	[M + K] ⁺	amino acids
172.01 172.01	aspartic acid	[M + K] ⁺	[M + K] ⁺	amino acids
143.99 143.99	serine ¹	[M + K] ⁺	[M + K] ⁺	amino acids
154.00 154.02	proline	[M + K] ⁺	[M + K] ⁺	amino acids
156.02 156.02	valine	[M + K] ⁺	[M + K] ⁺	amino acids
158.00 158.01	threonine	[M + K] ⁺	[M + K] ⁺	amino acids
167.01	2-amino-4-cyano-butanoic acid		[M + K] ⁺	amino acids
167.99 168.00	pyroglutamic acid	[M + K] ⁺	[M + K] ⁺	amino acids
169.04 185.02 169.05 185.02	glutamine ¹	[M + Na] ⁺ [M + K] ⁺	[M + Na] ⁺ [M + K] ⁺	amino acids
170.03 170.03	creatine ¹	[M + K] ⁺	[M + K] ⁺	amino acids
186.00 186.01	glutamic acid ¹	[M + K] ⁺	[M + K] ⁺	amino acids
188.00 188.00	methionine	[M + K] ⁺	[M + K] ⁺	amino acids
194.01 194.02	histidine	[M + K] ⁺	[M + K] ⁺	amino acids
195.99 196.01	amino-muconic acid	[M + K] ⁺	[M + K] ⁺	amino acids
204.03	phenylalanine		[M + K] ⁺	amino acids
213.06	arginine		[M + K] ⁺	amino acids
111.09 111.10	putrescine	[M + Na] ⁺	[M + Na] ⁺	alkaloids
160.99 160.99	nicotinamide	[M + K] ⁺	[M + K] ⁺	alkaloids
168.13 184.09 184.10	spermidine	[M + K] ⁺	[M + Na] ⁺ [M + K] ⁺	alkaloids
241.17 241.18	spermine ¹	[M + K] ⁺	[M + K] ⁺	alkaloids
174.01 174.02	adenine	[M + K] ⁺	[M + K] ⁺	purine
159.00 174.98 174.99	hypoxanthine	[M + K] ⁺	[M + Na] ⁺ [M + K] ⁺	purine
150.96 150.96	uracil	[M + K] ⁺	[M + K] ⁺	pyrimidine
126.02 126.03 142.00 142.00	γ-aminobutyric acid (GABA) ¹	[M + Na] ⁺ [M + K] ⁺	[M + Na] ⁺ [M + K] ⁺	neurotransmitters

(table continued on next page)

measured <i>m/z</i>	compound	detected ions		classification
		ZnO	TiO ₂	
192.03 192.04	dopamine ¹	[M + K] ⁺	[M + K] ⁺	neurotransmitters
208.02 208.02	norepinephrine ¹	[M + K] ⁺	[M + K] ⁺	neurotransmitters
222.05	epinephrine		[M + K] ⁺	neurotransmitters
306.06	adenosine		[M + K] ⁺	neurotransmitters
126.99	butyric acid		[M + K] ⁺	fatty acids
168.98	5-oxohexanoic acid		[M + K] ⁺	fatty acids
197.08	pelargonic acid	[M + K] ⁺		fatty acids
277.18 277.19	FA(16:1)	[M + Na] ⁺	[M + Na] ⁺	fatty acids
279.22	FA(16:0)	[M + K] ⁺		fatty acids
305.25 321.22 321.23	FA(18:1)	[M + Na] ⁺ [M + K] ⁺	[M + K] ⁺	fatty acids
307.26 323.23 323.23	FA(18:0)	[M + Na] ⁺ [M + K] ⁺	[M + K] ⁺	fatty acids
327.23 343.21 343.21	FA(20:4)	[M + Na] ⁺ [M + K] ⁺	[M + K] ⁺	fatty acids
351.22 367.21 351.24 367.21	FA(22:6)	[M + Na] ⁺ [M + K] ⁺	[M + Na] ⁺ [M + K] ⁺	fatty acids
363.29	FA(21:1)	[M + K] ⁺		fatty acids
371.24	FA(22:4)	[M + K] ⁺		fatty acids
409.36 425.33 409.36 425.34	cholesterol	[M + Na] ⁺ [M + K] ⁺	[M + Na] ⁺ [M + K] ⁺	sterol lipids
423.32 439.31	OH-7-dehydrocholesterol	[M + Na] ⁺	[M + K] ⁺	sterol lipids
243.08	Met-Ala		[M + Na] ⁺	dipeptides
139.00 139.01	fumaric acid	[M + Na] ⁺	[M + Na] ⁺	organic acids
144.98 145.01	glyceric acid	[M + K] ⁺	[M + K] ⁺	organic acids
153.00 168.96	citraconic acid	[M + K] ⁺	[M + Na] ⁺	organic acids
154.99 154.99	levulinic acid	[M + K] ⁺	[M + K] ⁺	organic acids
141.02 156.98 156.99	succinic acid ¹	[M + Na] ⁺ [M + K] ⁺	[M + K] ⁺	organic acids
159.00 159.02	threonic acid	[M + Na] ⁺	[M + Na] ⁺	organic acids
187.01 187.02	cinnamic acid	[M + K] ⁺	[M + K] ⁺	organic acids
189.01 189.03	3-phenylpropionic acid	[M + K] ⁺	[M + K] ⁺	organic acids
212.97	aconitic acid		[M + K] ⁺	organic acids
217.00 217.02	glucuronic acid	[M + Na] ⁺	[M + Na] ⁺	organic acids
230.98	citric acid	[M + K] ⁺		organic acids
104.09 104.10	choline ¹	M ⁺	M ⁺	others

(table continued on next page)

measured <i>m/z</i>	compound	detected ions		classification
		ZnO	TiO ₂	
112.00 112.01	oxamic acid	[M + Na] ⁺	[M + Na] ⁺	others
149.99 150.00	cytosine	[M + K] ⁺	[M + K] ⁺	others
152.01 152.02	creatinine ¹	[M + K] ⁺	[M + K] ⁺	others
146.98 162.96 146.98 162.97	phosphonoacetaldehyde ¹	[M + Na] ⁺ [M + K] ⁺	[M + Na] ⁺ [M + K] ⁺	others
192.98 192.98	dihydroxyacetone phosphate	[M + Na] ⁺	[M + Na] ⁺	others
203.04 219.01 203.05 219.02	myo-inositol ¹	[M + Na] ⁺ [M + K] ⁺	[M + Na] ⁺ [M + K] ⁺	others
205.01 205.99	homovanillic acid pyridoxal	[M + Na] ⁺ [M + K] ⁺		others others
207.03 223.01 207.05 223.03	3-methoxy-4-hydroxyphenylglycol ¹	[M + Na] ⁺ [M + K] ⁺	[M + Na] ⁺ [M + K] ⁺	others
214.00 214.01	N-acetylaspartic acid ¹	[M + K] ⁺	[M + K] ⁺	others
228.01	N-acetylglutamic acid		[M + K] ⁺	others
246.03	N-acetylphenylalanine	[M + K] ⁺		others
258.05	pantothenic acid	[M + K] ⁺		others
260.04 260.05	N-acetylglucosamine	[M + K] ⁺	[M + K] ⁺	others
266.05	cytidine		[M + Na] ⁺	others
268.96	ribulose 5-phosphate	[M + K] ⁺		others
307.05 307.05	inosine	[M + K] ⁺	[M + K] ⁺	others
375.20 391.20	prostaglandin E2		[M + Na] ⁺ [M + K] ⁺	others

¹Molecule assignment was verified by MS/MS.

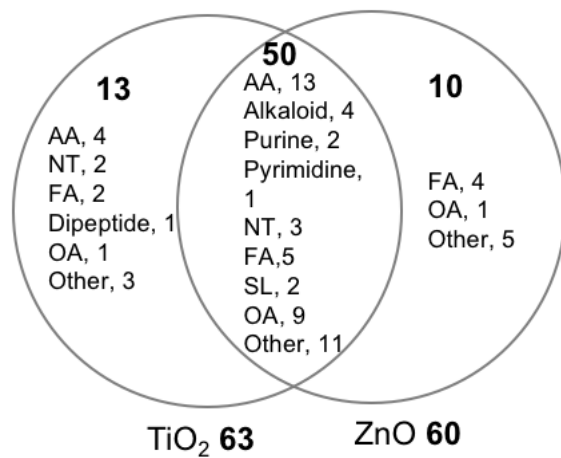


Figure 2.6. Lists of molecules detected from a mouse brain with either TiO₂ or ZnO NP-assisted LDI MSI (AA, amino acids; NT, neurotransmitters; SL, sterol lipids; FA, fatty acids; OA, organic acids).

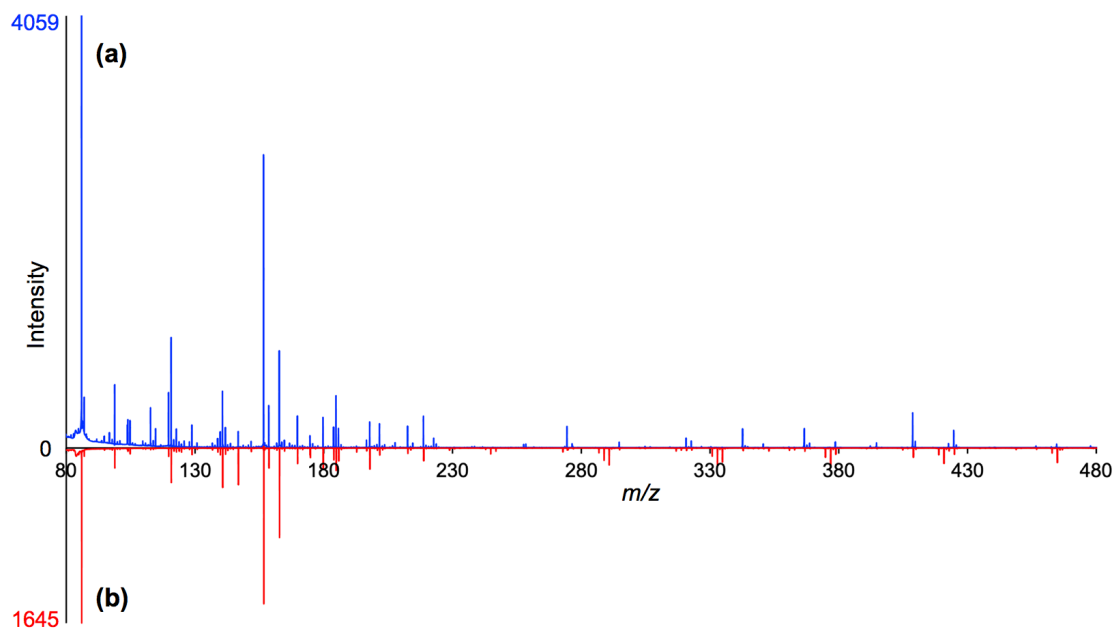


Figure 2.7. Averaged mass spectra from all pixels acquired on mouse coronal brain hemisphere sections with either **(a)** ZnO NP- or **(b)** TiO₂ NP-assisted LDI MSI at a raster step size of 70 μm .

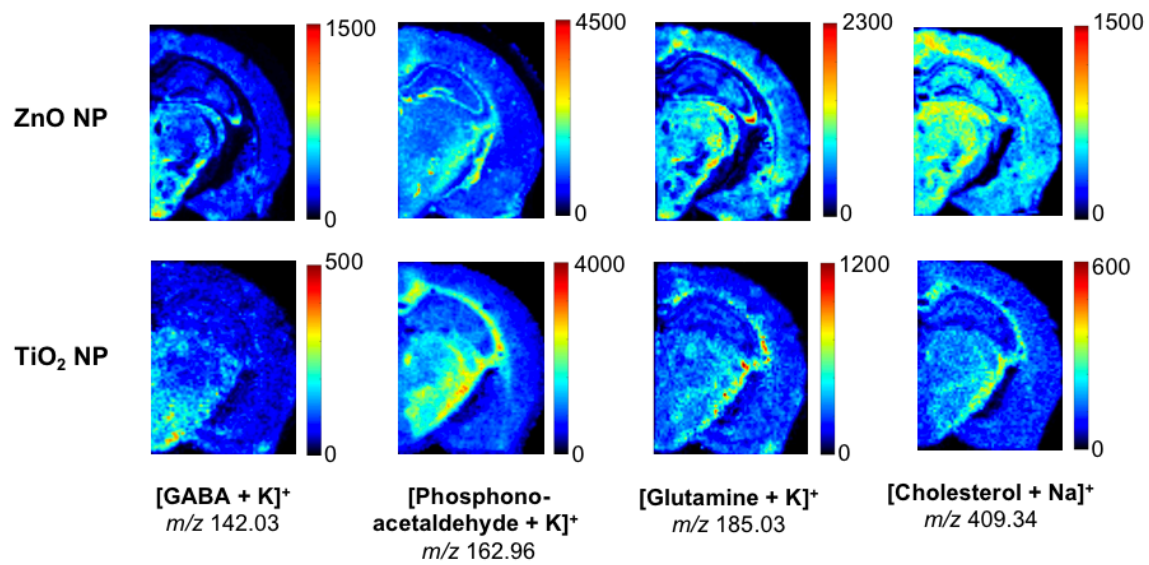


Figure 2.8. Ion images of mouse coronal brain hemisphere sections collected with ZnO NP or TiO₂ NP at a raster step size of 70 μm .

2.3.8 Effects of NP Aggregation on Spatial Resolutions

Generally, in matrix-assisted LDI MS imaging, the uniform deposition of the matrix coating is critical to the spatial resolution of the resulting ion images. This is the reason that gas-phase deposition methods, such as sublimation or sputtering, are preferred when high spatial resolution is required. When NP of metal oxides are used, the most direct deposition approach is spraying of NP dispersions. However, despite of the nanometer-size specified by the NP suppliers, a certain extent of NP aggregation was evident in our experience working with the NP presented in this work. Hence it is important to illustrate whether the ZnO NP presented herein imposes a limitation in the spatial resolution of LDI MS imaging.

The laser of our MALDI MS instrument has an estimated focused beam diameter of 35 μm . Based on our prior experience working with most uniform matrix coatings applied via sublimation, the optimal raster step setting of our instrument is 40 μm . That is, the resolution of images did not improve when a raster step size of 30 μm was attempted. Hence, we assessed the spatial resolution of images obtained with ZnO NP at three raster step size settings, 100, 70, and 40 μm , to represent respectively the “low,” “medium,” and “high” resolution settings of our instrument. MS images collected under these three settings are presented in Figure 2.9. Significant improvement in spatial resolution was evident at each reduction of the raster step size; i.e., more details in the localization of ions within the subfields of the hippocampus. This allows us to conclude that, the extent of aggregation of ZnO NP, if any, did not cause any issues in allowing an automated sprayer to produce a

uniform coating of the NP with the quality required to benefit from the 40 μm spatial resolution setting of our MALDI MS instrument.

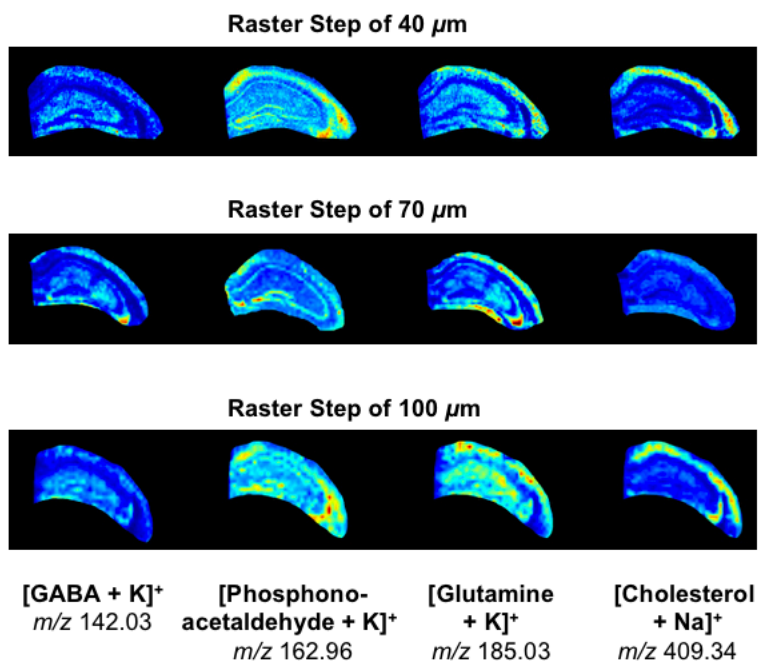


Figure 2.9. Ion images of the hippocampal region of a mouse brain acquired with ZnO NP-assisted LDI MSI at different raster step sizes.

2.3.9 Repeatability of ZnO NP-assisted LDI MSI

To examine the effects of NP aggregation on the repeatability of ZnO NP-assisted LDI MSI, we measured adjacent tissue sections from the same brain multiple times. Specifically, four adjacent tissue sections were mounted on one slide, ZnO dispersion was deposited in one spray run, and MS measurement was conducted under the same conditions as intra-slide replicates. In addition, four adjacent tissue sections were mounted on four different slides, ZnO dispersion was prepared separately and deposited in separate spray runs, and MS measurement was conducted under the same conditions as inter-slide replicates. The averaged spectra from the infralimbic cortex (IL) of adjacent tissue sections were exported. The peak areas were integrated using the m/z and intensity in the averaged spectra. Overall, intra-slide replicates are repeatable. The relative standard deviations of peak areas of signals at m/z 142.03, 186.02, 192.04, 219.03, and 409.34 acquired from four intra-slide replicates are less than 10%. Inter-slide replicates showed more variability, which can be explained by slight differences in matrix densities from ZnO dispersion preparation and matrix deposition. The relative standard deviations of peak areas of those signals from four inter-slide replicates range from 14% to 31%, depending on the signal. In conclusion, partial clogging can still happen during the spray run and causes signal variations in ZnO NP-assisted LDI MSI.

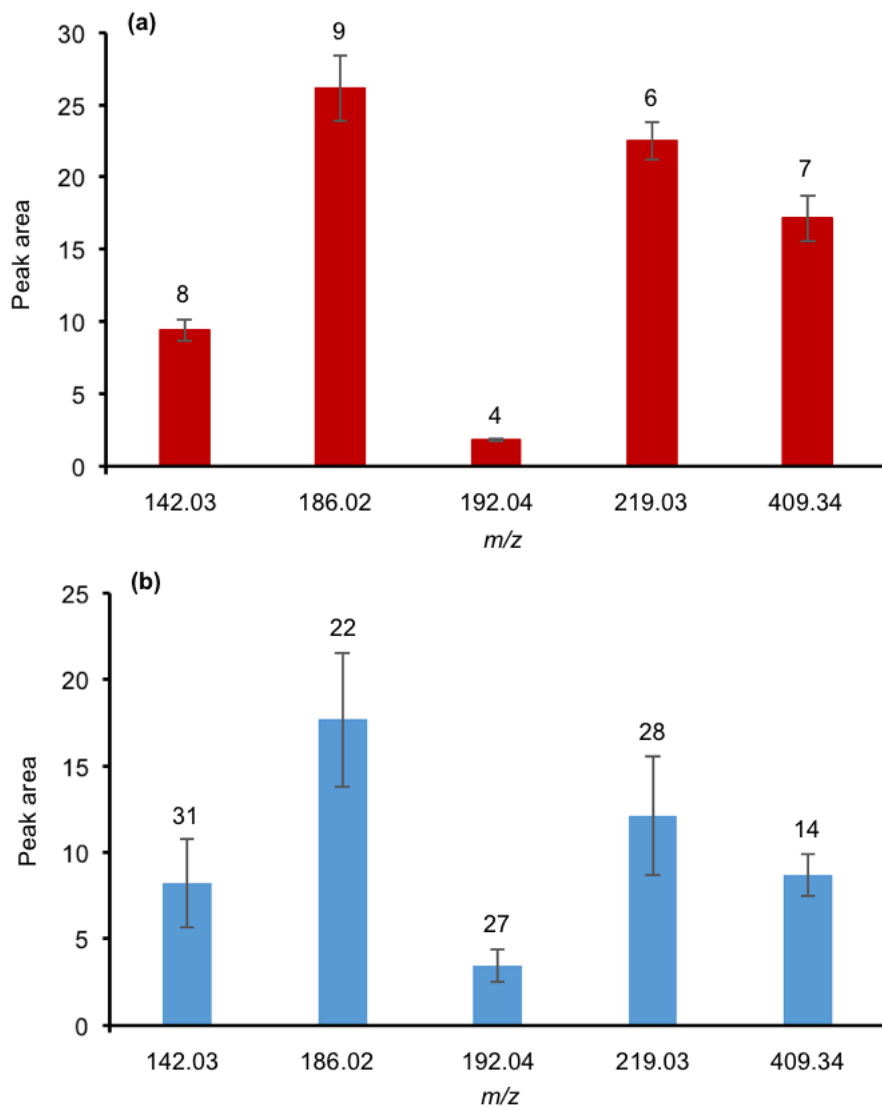


Figure 2.10. Average peak areas of signals at m/z 142.03, 186.02, 192.04, 219.03, and 409.34 with standard deviation error bars calculated using data obtained from (a) four adjacent tissue sections collected from the same rat brain on one slide as intra-slide replicates and (b) four adjacent tissue sections from the same rat brain on multiple slides and matrix deposited separately as inter-slide replicates. The relative standard deviations of replicates acquired are labeled on the corresponding bar graphs.

2.3.10 Effect of Salts in ZnO NP-assisted LDI MSI

Salt ions, particularly Na^+ and K^+ , are abundantly present in biological tissues, and they cannot be easily removed or washed away without losing other important endogenous ions in LMWM analysis and/or compromising their spatial resolution. Hence, it is reasonable that they are detected as the protonated ions, $[\text{M} + \text{H}]^+$, as well as the adducts of Na^+ and K^+ from biological tissues. When ZnO or TiO_2 NP were used to facilitate LDI MSI in our studies, Na^+ and K^+ adducts were predominantly detected (Table 2.2), although this may be attributed to our deliberate avoidance of sample acidification. Importantly, we hope that the images presented in Figures 2.4 and 2.5 can convince readers that the quality of the ion images was not compromised by the fact that they were from $[\text{M} + \text{Na}]^+$ and $[\text{M} + \text{K}]^+$ ions instead of $[\text{M} + \text{H}]^+$ ions.

While both signals from Na^+ or K^+ adducts were observed in many of the detected ions with ZnO NP assisted LDI MSI in our work, the signals from K^+ adducts were stronger in most cases. This was hypothesized to be a result of the generally higher amount of K^+ ions present in the brain, as the concentration of K^+ was estimated to be at least 10 times higher than that of Na^+ [78]. To test this hypothesis, the introduction of additional Na^+ and K^+ ions to the tissue samples should, in theory, further enhance the signal intensities of the corresponding ions in a similar way that acidification of sample will boost the signals of protonated ions. An experiment was therefore conducted to spike the tissue sections with solutions of potassium acetate or sodium acetate using an automated sprayer. The potassiated and sodiated ion intensity ratios for a number of detected LMWM are presented in Figure 2.11, with and without the spiked ions. As expected, the relative signal intensities

of the potassiated ions went up in the presence of additional K^+ (Figure 2.11a), and those of the sodiated ions went up with additional Na^+ (Figure 2.11b).

It is noteworthy that some of the $[M + Na]^+$ signals reported in Figure 2.11b were not detected before spiking the samples with additional Na^+ ions. In other words, the introduction of additional Na^+ ions was demonstrated to enhance the sensitivity of ZnO NP assisted LDI MSI. Similar approaches of using salt additives to enhance the analyte MS signals were reported [79,80]. Another benefit of using K^+ or Na^+ spiking to alter the relative ratio of the potassiated and sodiated ion is a confirmation on the identification of a given signal being either $[M + Na]^+$ or $[M + K]^+$. That is, a signal correctly assigned as $[M + Na]^+$ or $[M + K]^+$ should increase in relative intensity upon addition of the corresponding ions to the tissue sample. Furthermore, the natural isotope ratio of ^{39}K (93%) and ^{41}K (7%) could also be used to identify $[M + K]^+$ when the peak intensity is sufficiently high to see the small isotopic peak of $[M + ^{41}K]^+$ (shown in the figure inset of Figure 2.11a).

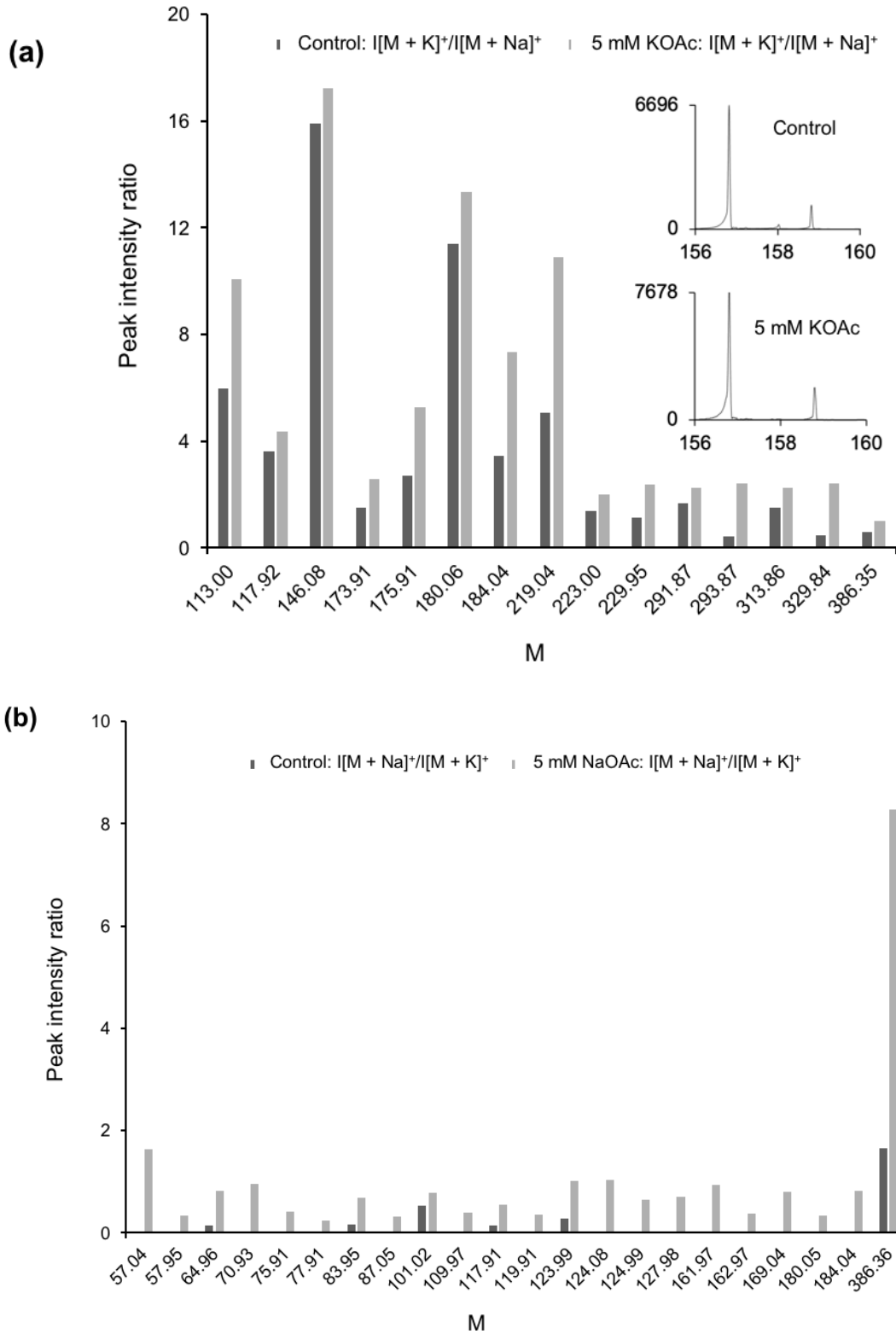


Figure 2.11. Peak height intensity ratios of the sodiated and potassiated ions from two adjacent mouse brain tissue sections without (control) and with the application of 5 mM potassium acetate (KOAc) **(a)** or 5 mM sodium acetate (NaOAc) **(b)** by automated sprayer. M represent the molecular weight. The figure inset shows the isotope patterns of $[M + K]^+$ at m/z 156.88 without and with the application of 5 mM potassium acetate.

2.4 Conclusion

Compared to TiO₂ NP, the use of ZnO NP to facilitate LDI MS imaging of biological tissues is uncommon, and the performance of ZnO NP as a matrix for LDI was not generally regarded as particularly superior in the literature. In this work, we demonstrated that commercially available ZnO NP dispersion is indeed ideal for facilitating the LDI MS imaging of LMWM in brain tissues. It offers many desirable characteristics, including a low degree of NP aggregation, low level of matrix background signals in the low mass region, compatibility with automated sprayers, superb detectability of LMWM, and the ability to deliver relatively high spatial resolution images. These characteristics are essential in achieving highly sensitive and reproducible imaging data, and importantly, in developing an automated workflow for routine and/or large sample-size analyses.

2.5 References

- (1) Hanrieder, J.; Phan, N. T. N.; Kurczy, M. E.; Ewing, A. G. *Acs Chemical Neuroscience* **2013**, *4*, 666-679.
- (2) Pandey, R.; Caflisch, L.; Lodi, A.; Brenner, A. J.; Tiziani, S. *Molecular Carcinogenesis* **2017**, *56*, 2355-2371.
- (3) Dumas, M. E.; Davidovic, L. *Journal of Neuroimmune Pharmacology* **2015**, *10*, 402-424.
- (4) Gonzalez-Riano, C.; Garcia, A.; Barbas, C. *Journal of Pharmaceutical and Biomedical Analysis* **2016**, *130*, 141-168.
- (5) Trushina, E.; Mielke, M. M. *Biochimica Et Biophysica Acta-Molecular Basis of Disease* **2014**, *1842*, 1232-1239.
- (6) Sharma, S.; Moon, C. S.; Khogali, A.; Haidous, A.; Chabenne, A.; Ojo, C.; Jelebinkov, M.; Kurdi, Y.; Ebadi, M. *Neurochemistry International* **2013**, *63*, 201-229.
- (7) Zaima, N.; Hayasaka, T.; Goto-Inoue, N.; Setou, M. *International Journal of Molecular Sciences* **2010**, *11*, 5040-5055.
- (8) Vickerman, J. C. *Analyst* **2011**, *136*, 2199-2217.
- (9) van Hove, E. R. A.; Smith, D. F.; Heeren, R. M. A. *Journal of Chromatography A* **2010**, *1217*, 3946-3954.
- (10) Thomas, A.; Charbonneau, J. L.; Fournaise, E.; Chaurand, P. *Analytical Chemistry* **2012**, *84*, 2048-2054.
- (11) Wang, X. D.; Han, J.; Pan, J. X.; Borchers, C. H. *Analytical Chemistry* **2014**, *86*, 638-646.
- (12) Le, C. H.; Han, J.; Borchers, C. H. *Analytical Chemistry* **2012**, *84*, 8391-8398.

- (13) Francese, S.; Bradshaw, R.; Flinders, B.; Mitchell, C.; Bleay, S.; Cicero, L.; Clench, M. R. *Analytical Chemistry* **2013**, *85*, 5240-5248.
- (14) Wang, X. D.; Han, J.; Chou, A.; Yang, J. C.; Pan, J. X.; Borchers, C. H. *Analytical Chemistry* **2013**, *85*, 7566-7573.
- (15) Li, B.; Sun, R. Y.; Gordon, A.; Ge, J. Y.; Zhang, Y.; Li, P.; Yang, H. *Analytical Chemistry* **2019**, *91*, 8221-8228.
- (16) Enthaler, B.; Trusch, M.; Fischer, M.; Rapp, C.; Pruns, J. K.; Vietzke, J. P. *Analytical and Bioanalytical Chemistry* **2013**, *405*, 1159-1170.
- (17) Ly, A.; Buck, A.; Balluff, B.; Sun, N.; Gorzolka, K.; Feuchtinger, A.; Janssen, K. P.; Kuppen, P. J. K.; van de Velde, C. J. H.; Weirich, G.; Erlmeier, F.; Langer, R.; Aubele, M.; Zitzelsberger, H.; McDonnell, L.; Aichler, M.; Walch, A. *Nature Protocols* **2016**, *11*, 1428-1443.
- (18) Miura, D.; Fujimura, Y.; Yamato, M.; Hyodo, F.; Utsumi, H.; Tachibana, H.; Wariishi, H. *Analytical Chemistry* **2010**, *82*, 9789-9796.
- (19) Sugiura, Y.; Honda, K.; Kajimura, M.; Suematsu, M. *Proteomics* **2014**, *14*, 829-838.
- (20) Wang, J. N.; Qiu, S. L.; Chen, S. M.; Xiong, C. Q.; Liu, H. H.; Wang, J. Y.; Zhang, N.; Hou, J.; He, Q.; Nie, Z. X. *Analytical Chemistry* **2015**, *87*, 422-430.
- (21) Liu, H. H.; Zhou, Y. M.; Wang, J. Y.; Xiong, C. Q.; Xue, J. J.; Zhan, L. P.; Nie, Z. X. *Analytical Chemistry* **2018**, *90*, 729-736.
- (22) Ibrahim, H.; Jurcic, K.; Wang, J. S. H.; Whitehead, S. N.; Yeung, K. K. C. *Analytical Chemistry* **2017**, *89*, 12828-12836.
- (23) Sun, C. L.; Liu, W.; Mu, Y.; Wang, X. *Talanta* **2020**, *209*, 9.
- (24) Gemperline, E.; Rawson, S.; Li, L. J. *Analytical Chemistry* **2014**, *86*, 10030-10035.

- (25) Teearu, A.; Vahur, S.; Haljasorg, U.; Leito, I.; Haljasorg, T.; Toom, L. *Journal of Mass Spectrometry* **2014**, *49*, 970-979.
- (26) Smirnov, I. P.; Zhu, X.; Taylor, T.; Huang, Y.; Ross, P.; Papayanopoulos, I. A.; Martin, S. A.; Pappin, D. J. *Analytical Chemistry* **2004**, *76*, 2958-2965.
- (27) He, H. X.; Qin, L.; Zhang, Y. W.; Han, M. M.; Li, J. M. M.; Liu, Y. Q.; Qiu, K. D.; Dai, X. Y.; Li, Y. Y.; Zeng, M. M.; Guo, H. H.; Zhou, Y. J.; Wang, X. D. *Analytical Chemistry* **2019**, *91*, 2634-2643.
- (28) Esteve, C.; Tolner, E. A.; Shyti, R.; van den Maagdenberg, A.; McDonnell, L. A. *Metabolomics* **2016**, *12*, 9.
- (29) Shariatgorji, M.; Nilsson, A.; Goodwin, R. J. A.; Kallback, P.; Schintu, N.; Zhang, X. Q.; Crossman, A. R.; Bezar, E.; Svenningsson, P.; Andren, P. E. *Neuron* **2014**, *84*, 697-707.
- (30) Manier, M. L.; Spraggins, J. M.; Reyzer, M. L.; Norris, J. L.; Caprioli, R. M. *Journal of Mass Spectrometry* **2014**, *49*, 665-673.
- (31) Wu, Q.; Comi, T. J.; Li, B.; Rubakhin, S. S.; Sweedler, J. V. *Analytical Chemistry* **2016**, *88*, 5988-5995.
- (32) Sun, C.; Liu, W.; Geng, Y.; Wang, X. *Analytical Chemistry* **2020**, *92*, 12126-12131.
- (33) Shariatgorji, R.; Nilsson, A.; Strittmatter, N.; Vallianatou, T.; Zhang, X.; Svenningsson, P.; Goodwin, R. J. A.; Andren, P. E. *Journal of the American Society for Mass Spectrometry* **2020**, *31*, 2553-2557.
- (34) Shariatgorji, M.; Nilsson, A.; Fridjonsdottir, E.; Vallianatou, T.; Kallback, P.; Katan, L.; Savmarker, J.; Mantas, I.; Zhang, X. Q.; Bezar, E.; Svenningsson, P.; Odell, L. R.; Andren, P. E. *Nature Methods* **2019**, *16*, 1021-1028.

- (35) Stopka, S. A.; Rong, C.; Korte, A. R.; Yadavilli, S.; Nazarian, J.; Razunguzwa, T. T.; Morris, N. J.; Vertes, A. *Angewandte Chemie International Edition* **2016**, *55*, 4482-4486.
- (36) Shi, R.; Dai, X.; Li, W. F.; Lu, F.; Liu, Y.; Qu, H. H.; Li, H.; Chen, Q. Y.; Tian, H.; Wu, E. H.; Wang, Y.; Zhou, R. H.; Lee, S. T.; Lifshitz, Y.; Kang, Z. H.; Liu, J. *ACS Nano* **2017**, *11*, 9500-9513.
- (37) Lv, R.; Shi, R.; Wu, E. H.; Ma, C. Q.; Guo, R. C.; Li, J.; Ouyang, F. Z.; Fang, Q. Q.; Hu, L. H.; Sun, C.; Liu, Y.; Kang, Z. H.; Liu, J. *Talanta* **2020**, *220*, 8.
- (38) Korte, A. R.; Song, Z. H.; Nikolau, B. J.; Lee, Y. J. *Analytical Methods* **2012**, *4*, 474-481.
- (39) Zhou, D.; Guo, S.; Zhang, M.; Liu, Y. J.; Chen, T. J.; Li, Z. L. *Analytica Chimica Acta* **2017**, *962*, 52-59.
- (40) Wang, Z. J.; Cai, Y.; Wang, Y.; Zhou, X. W.; Zhang, Y.; Lu, H. J. *Scientific Reports* **2017**, *7*, 9.
- (41) Chen, S. M.; Xiong, C. Q.; Liu, H. H.; Wan, Q. Q.; Hou, J.; He, Q.; Badu-Tawiah, A.; Nie, Z. X. *Nature Nanotechnology* **2015**, *10*, 176-182.
- (42) Hansen, R. L.; Duenas, M. E.; Lee, Y. J. *Journal of the American Society for Mass Spectrometry* **2019**, *30*, 299-308.
- (43) Sekula, J.; Niziol, J.; Rode, W.; Ruman, T. *Analytica Chimica Acta* **2015**, *875*, 61-72.
- (44) Tang, H. W.; Wong, M. Y. M.; Lam, W.; Cheng, Y. C.; Che, C. M.; Ng, K. M. *Rapid Communications in Mass Spectrometry* **2011**, *25*, 3690-3696.
- (45) Kawasaki, H.; Ozawa, T.; Hisatomi, H.; Arakawa, R. *Rapid Communications in Mass Spectrometry* **2012**, *26*, 1849-1858.

- (46) Hayasaka, T.; Goto-Inoue, N.; Zaima, N.; Shrivastava, K.; Kashiwagi, Y.; Yamamoto, M.; Nakamoto, M.; Setou, M. *Journal of the American Society for Mass Spectrometry* **2010**, *21*, 1446-1454.
- (47) Dufresne, M.; Thomas, A.; Breault-Turcot, J.; Masson, J. F.; Chaurand, P. *Analytical Chemistry* **2013**, *85*, 3318-3324.
- (48) Jun, J. H.; Song, Z. H.; Liu, Z. J.; Nikolau, B. J.; Yeung, E. S.; Lee, Y. J. *Analytical Chemistry* **2010**, *82*, 3255-3265.
- (49) Yang, E.; Fournelle, F.; Chaurand, P. *Journal of Mass Spectrometry* **2020**, *55*, 10.
- (50) Niziol, J.; Misiolek, M.; Ruman, T. *Phytochemistry* **2019**, *159*, 11-19.
- (51) Cha, S. W.; Song, Z. H.; Nikolau, B. J.; Yeung, E. S. *Analytical Chemistry* **2009**, *81*, 2991-3000.
- (52) Niziol, J.; Sunner, J.; Beech, I.; Ossolinski, K.; Ossolinska, A.; Ossolinski, T.; Plaza, A.; Ruman, T. *Analytical Chemistry* **2020**, *92*, 4251-4258.
- (53) Klein, A. T.; Yagnik, G. B.; Hohenstein, J. D.; Ji, Z. Y.; Zi, J. C.; Reichert, M. D.; MacIntosh, G. C.; Yang, B.; Peters, R. J.; Vela, J.; Lee, Y. J. *Analytical Chemistry* **2015**, *87*, 5294-5301.
- (54) Wei, W. W.; Zhong, Y. H.; Zou, T.; Chen, X. F.; Ren, L.; Qi, Z. H.; Liu, G. G.; Chen, Z. F.; Cai, Z. W. *Journal of Hazardous Materials* **2020**, *388*, 9.
- (55) Feenstra, A. D.; Hansen, R. L.; Lee, Y. J. *Analyst* **2015**, *140*, 7293-7304.
- (56) Shrivastava, K.; Hayasaka, T.; Sugiura, Y.; Setou, M. *Analytical Chemistry* **2011**, *83*, 7283-7289.
- (57) Bradshaw, R.; Denison, N.; Francese, S. *Analytical Methods* **2016**, *8*, 6795-6804.
- (58) Hinners, P.; Lee, Y. J. *Journal of Mass Spectrometry* **2020**, *55*, 9.

- (59) Wu, Q.; Chu, J. L.; Rubakhin, S. S.; Gillette, M. U.; Sweedler, J. V. *Chemical Science* **2017**, *8*, 3926-3938.
- (60) Wang, J. N.; Sun, J.; Wang, J. Y.; Liu, H. H.; Xue, J. J.; Nie, Z. X. *Chemical Communications* **2017**, *53*, 8114-8117.
- (61) Yagnik, G. B.; Hansen, R. L.; Korte, A. R.; Reichert, M. D.; Vela, J.; Lee, Y. J. *Analytical Chemistry* **2016**, *88*, 8926-8930.
- (62) Li, P. D.; Jiu, T. G.; Tang, G.; Wang, G. J.; Li, J.; Li, X. F.; Fang, J. F. *Acs Applied Materials & Interfaces* **2014**, *6*, 18172-18179.
- (63) French, R. A.; Jacobson, A. R.; Kim, B.; Isley, S. L.; Penn, R. L.; Baveye, P. C. *Environmental Science & Technology* **2009**, *43*, 1354-1359.
- (64) Mallakpour, S.; Madani, M. *Progress in Organic Coatings* **2015**, *86*, 194-207.
- (65) Pachon, L. D.; Rothenberg, G. *Applied Organometallic Chemistry* **2008**, *22*, 288-299.
- (66) Kinumi, T.; Saisu, T.; Takayama, M.; Niwa, H. *Journal of Mass Spectrometry* **2000**, *35*, 417-422.
- (67) Watanabe, T.; Kawasaki, H.; Yonezawa, T.; Arakawa, R. *Journal of Mass Spectrometry* **2008**, *43*, 1063-1071.
- (68) Yang, H.-J.; Lee, A.-R.; Lee, M.-K.; Kim, W.; Kim, J.-K. *Bulletin of the Korean Chemical Society* **2010**, *31*, 35-40.
- (69) Bae, E.; Murakami, N.; Nakamura, M.; Ohno, T. *Applied Catalysis A: General* **2010**, *380*, 48-54.
- (70) Robichaud, G.; Garrard, K. P.; Barry, J. A.; Muddiman, D. C. *Journal of the American Society for Mass Spectrometry* **2013**, *24*, 718-721.
- (71) Oskam, G. *Journal of Sol-Gel Science and Technology* **2006**, *37*, 161-164.

- (72) Chen, J. X.; Ruther, R. E.; Tan, Y. Z.; Bishop, L. M.; Hamers, R. J. *Langmuir* **2012**, *28*, 10437-10445.
- (73) Castro, A. L.; Madeira, P. J. A.; Nunes, M. R.; Costa, F. M.; Florencio, M. H. *Rapid Communications in Mass Spectrometry* **2008**, *22*, 3761-3766.
- (74) Lorkiewicz, P.; Yappert, M. C. *Analytical Chemistry* **2009**, *81*, 6596-6603.
- (75) Yonezawa, T.; Asano, T.; Matsubara, M. *Bulletin of the Chemical Society of Japan* **2016**, *89*, 346-353.
- (76) Popovic, I.; Nesic, M.; Vranjes, M.; Saponjic, Z.; Petkovic, M. *RSC Advances* **2016**, *6*, 1027-1036.
- (77) Watanabe, T.; Okumura, K.; Kawasaki, H.; Arakawa, R. *Journal of Mass Spectrometry* **2009**, *44*, 1443-1451.
- (78) Takahashi, S.; Hatashita, S.; Taba, Y.; Sun, X. Z.; Kubota, Y.; Yoshida, S. *Journal of Neuroscience Methods* **2000**, *100*, 53-62.
- (79) Sugiura, Y.; Setou, M. *Rapid Communications in Mass Spectrometry* **2009**, *23*, 3269-3278.
- (80) Griffiths, R. L.; Bunch, J. *Rapid Communications in Mass Spectrometry* **2012**, *26*, 1557-1566.

**Chapter 3: Relative Quantitation of Neurotransmitters in
Brains from Adolescent and Adult Rats Subjected to
Chronic Adolescent Nicotine Exposure Using Laser
Desorption/Ionization Mass Spectrometry Imaging
Assisted with ZnO Nanoparticles**

3.1 Introduction

Altered abundances of small molecules, especially small-molecule neurotransmitters, in specific brain regions are involved in neurological disorders [1-5]. For example, a significant elevation in glutamate was observed in basal ganglia in schizophrenia patients compared to healthy individuals [4]. A decrease in the level of γ -aminobutyric acid (GABA) has been found in mouse brains with familial Alzheimer's disease [5]. Nuclear magnetic resonance spectroscopy, most commonly known as NMR spectroscopy or magnetic resonance spectroscopy (MRS), and mass spectrometry (MS) are two analytical techniques commonly applied in small molecule quantitation studies [6-8]. MRS is a non-invasive and non-destructive method and is capable of quantifying regional brain molecules without sample preparation. Because the naturally abundant hydrogen exists in a large number of small molecules and is one of the most sensitive nuclei, ^1H -MRS is extensively used for its high sensitivity. However, the sensitivity of ^1H -MRS is still relatively low compared to MS [9]. In MS-based techniques, gas chromatography (GC) or liquid chromatography (LC) coupled to MS can measure the abundance of small molecules from various brain regions after brain dissection and extraction of small molecules from each brain region separately. Mass spectrometry imaging (MSI), on the other hand, does not require the extraction of small molecules and provides information on their abundances and spatial distributions of the small molecules in multiple sub-regions of the brain because of its high spatial resolution. Among the ionization techniques compatible with MSI, matrix-assisted laser desorption ionization (MALDI) has been the most widely used ionization method because the careful selection of matrices favours the detection and imaging of a specific class of compounds [10, 11].

In quantitative MALDI MSI, the signal intensity of an analyte is related not only to its concentration but also to its microenvironment, the matrix deposition, and MS measurement [12, 13]. In the MALDI source, endogenous biomolecules from the tissues compete with the analytes for ionization, which is also referred to as ion suppression. In heterogeneous tissues (like brain tissue), strong changes in ion suppression induced from different anatomical regions with diverse chemical compositions and histological structures contributes to signal variations in various parts of the brain [14]. Therefore, it is generally difficult to generate a reliable calibration curve to perform absolute quantitation, which provides an accurate value of the concentration or amount of the compound of interest in well-defined regions of the brain [12, 15]. Alternatively, relative quantitation of analytes, allowing the evaluation of relative concentrations of molecules in different regions within a single tissue section or relative level changes between different tissue samples such as vehicle-treated versus drug-treated or control versus disease model, has been more commonly applied for the investigation of biomarkers in diseases [12]. Recent quantitative MALDI MSI studies have shown success in relatively quantifying small molecules such as metabolites [16-18] and drugs and their metabolites [19-25] from different treatments.

Ion signal correction (normalization) is normally required to achieve reliable relative quantitation. For example, normalization to an isotope-labelled standard has been suggested to help correct for the signal variations from the sample preparation, MS measurement, and ion suppression effect and significantly improve the quantitative ability of MALDI MSI [12]. However, it is not always feasible to apply the normalization to the

isotope-labelled standard since the standard need to be applied at an appropriate level, ideally at a similar concentration to the level of the analyte in the sample, to be effective [14]. Alternatively, the relative quantitation of target analyte between the vehicle-treated versus drug-treated or control versus disease model has been conducted by putting one sample of each group (vehicle- or drug-treated) on one slide and achieved by calculating the ion signal ratios between the samples. In this approach, the sample preparation and MS measurement between the samples on the same slide are considered to be identical, while the ion suppression effect in the same region between the samples is assumed to be similar [18].

Recently, Dr. Laviolette's lab at Western University is assessing the effects of chronic adolescent nicotine exposure on behavioural, neuronal, and molecular alterations using animal models. Nicotine, the principal constituent of the tobacco plant and commercial cigarettes, is considered to be the main cause of compulsive tobacco smoking. Chronic nicotine exposure during adolescence has been found to produce anxiety- and depressive-like behavioural abnormalities in adulthood in rats [26, 27]. Social withdrawal (demonstrated by the rat spending less time with unfamiliar rats) and social recognition memory deficits (demonstrated by the rat spending the same amount of time with a familiar rat versus an unfamiliar rat) have been reported in adult rats exposed to nicotine during adolescence. Anxiety-like behaviours in an open field (the rat spent more time in the outer zone of the test chamber), light/dark box (the rat spent more time in the dark environment and had fewer transitions between light and dark environments), and fear conditioning assays (the rat would freeze longer to fear-related cues) have also been reported in adult

rats following adolescent nicotine exposure [26, 27]. The electrical activities of neurons, which are from the flow of ions, have been measured using electrophysiology (EP) tools. As shown in Figure 3.1 [28], chronic adolescent nicotine exposure has been shown to upregulate the activities of glutamatergic neurons in the medial prefrontal cortex (mPFC), GABAergic neurons in the nucleus accumbens shell (NAcSh), and dopaminergic neurons in the ventral tegmental area (VTA) in the adult rat brains [26, 27]. Furthermore, a reduction in dopamine type 1 receptors (D1R), an elevation of the phosphorylated extracellular signal-regulated kinase (ERK) 1-2 in the mPFC and NAcSh, and upregulation of protein kinase B (Akt)-glycogen-synthase-kinase-3 (GSK-3) signalling pathways in the NAcSh have been linked to chronic nicotine exposure during adolescence [26, 27].

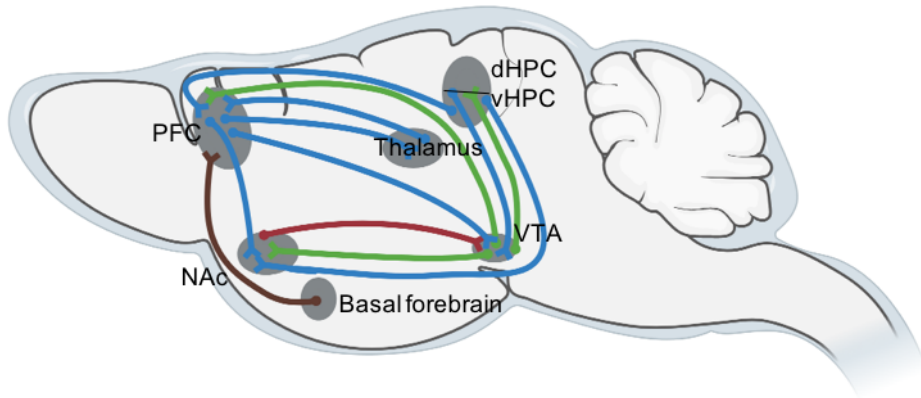


Figure 3.1. A simplified diagram of the main connections to and from the PFC (prefrontal cortex), NAc (nucleus accumbens), basal forebrain, thalamus, dHPC (dorsal hippocampus), vHPC (ventral hippocampus), and VTA (ventral tegmental area), in a sagittal section of a rodent brain. GABAergic, glutamatergic, dopaminergic, and cholinergic projections are in red, blue, green, and brown, respectively. Figure created using BioRender (<https://biorender.com/>).

Regardless, the effects of chronic adolescent nicotine exposure on the total neurotransmitter levels in various brain regions remain unclear. The total neurotransmitter levels could be affected by several processes, including synthesis, release, receptor binding, and metabolism. For example, after the release of GABA from the presynaptic terminals of GABAergic neurons, GABA binds to the target receptors on the postsynaptic neuron. The inhibitory action of GABA at the synapse is terminated by its reuptake into both presynaptic neurons and surrounding glial cells where GABA gets metabolized. Most of the previous studies focused on neurotransmitter release when investigating the impact of nicotine on neurotransmitters [29, 30]. Nicotine binds to the nicotinic acetylcholine receptors (nAChRs), which are ligand-gated ion channels and composed of different subunits that are widely distributed throughout the central nervous system (CNS), including the prefrontal cortex (PFC), nucleus accumbens (NAc), hippocampus (HPC), and VTA [31]. The neurotransmitter levels may be altered from nicotine exposure through direct and indirect interactions in several regions across the brain. Activation of presynaptic and preterminal nAChRs directly enhances the release of many different neurotransmitters, including acetylcholine (ACh), GABA, glutamate, and dopamine [29]. The binding of nicotine to somatodendritic or postsynaptic nAChRs promotes the release of neurotransmitters and can have opposite modulatory effects on downstream neurons depending on whether nAChRs are expressed on excitatory or inhibitory neurons [30]; e.g., the activation of postsynaptic nAChRs on excitatory neurons, glutamatergic neurons, promotes the release of glutamate and makes the target neuron more likely to transfer the electrical signals to nearby neurons. Moreover, nicotine may alter neurotransmitter release by indirect interaction through the inputs of other neurons [30]. For example, the nicotine-

induced release of NAc dopamine is mediated directly by nAChRs located on presynaptic and postsynaptic terminals of dopaminergic neurons and indirectly by glutamate and GABA received on dopaminergic neurons in the VTA, as shown in Figure 3.2 [28].

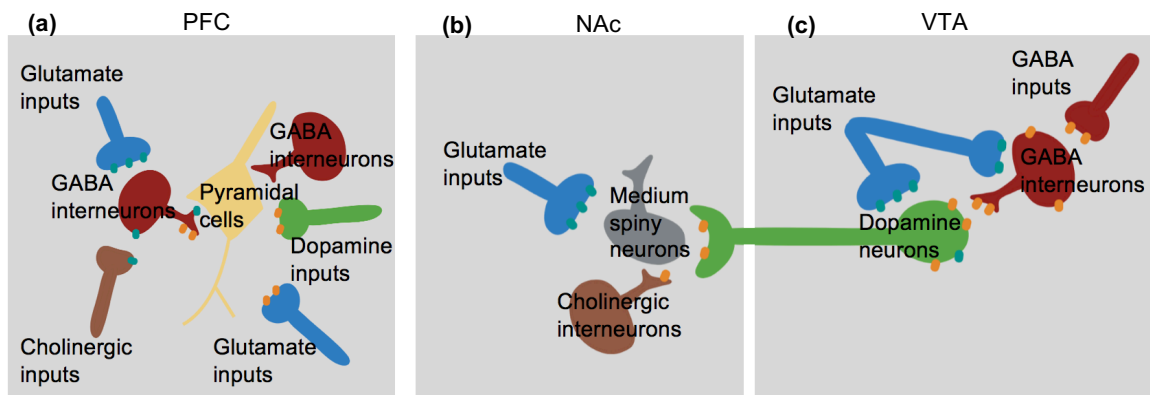


Figure 3.2. Schematic diagram shows the neurons in the (a) PFC, (b) NAc, and (c) VTA. The green and orange dots represent $\alpha 7$ and $\alpha 4\beta 2$ subunits of nAChRs (nicotinic acetylcholine receptors), respectively. Figure created using BioRender (<https://biorender.com/>).

In this study, we applied matrix-assisted laser desorption ionization MSI (MALDI MSI) to study the effects of chronic adolescent nicotine exposure on total neurotransmitter levels in various brain regions in both adolescent and adult rat brains, providing information to the Laviolette lab. The application of ZnO nanoparticles (NP) allows us to measure the abundances of GABA and glutamate and map their distributions in various brain sections without an extra derivatization step. The superior spatial resolution allows MALDI MSI to examine the total neurotransmitter abundance in multiple well-defined regions between the nicotine-treated and vehicle-treated samples, including the prelimbic cortex (PrL) and infralimbic cortex (IL), the sub-regions of mPFC, nucleus accumbens core (NAcC) and NAcSh, the sub-regions of NAc, and dorsal subiculum (DS) and ventral subiculum (VS), the sub-regions of dorsal and ventral hippocampus (dHPC and vHPC) respectively, in both adolescent and adult rat brains subject to chronic adolescent nicotine exposure. Current evidence indicates functional differences between the PrL and IL, NAcC and NAcSh, and dHPC and vHPC from behavioural, anatomical, and gene expression studies [32-34]. Specifically, the PrL is more involved in cognitive functions, while the IL modulates fear related behaviours [33]; the NAcC is related to reward seeking, while the NAcSh helps avoid distractions [34]; the dHPC is primarily involved in cognitive functions, while the vHPC regulates stress, emotion, and affect [32]. The results will help us understand the short-term and long-lasting effects of chronic nicotine exposure during adolescence on total neurotransmitter levels in various regions of interest (ROI) in adolescent and adult brains. In addition, these study results from animal models can be used for direct comparison with human studies using MRS.

3.2 Experimental Section

3.2.1 Chemicals and Supplies

Nicotine bitartrate, phosphate-buffered saline (PBS), ZnO NP aqueous dispersion (50 %, wt) with a particle size of less than 100 nm (product no. 721077), and α -cyano-4-hydroxycinnamic acid (CHCA) were purchased from Sigma-Aldrich (St. Louis, MO). Sodium pentobarbital (Euthanyl) was purchased from Bimeda-MTC Animal Health Inc. (Quebec, Canada). HPLC-grade acetonitrile (ACN) was purchased from VMR (Karlsruhe, Germany). Methanol (MeOH), trifluoroacetic acid (TFA), and Optima grade water, ACN, formic acid, and ammonium formate were purchased from Fisher Scientific (Waltham, MA). Chloroform was purchased from Merck Group (Darmstadt, Germany). Deionized water (18.2 M Ω ·cm) was purified by the Milli-Q Gradient A10 System (Darmstadt, Germany). Indium-tin oxide (ITO) coated glass slides were purchased from Hudson Surface Technology (Old Tappan, NJ).

3.2.2 Animals and housing

Adolescent Sprague-Dawley male rats were obtained at postnatal day (PND) 30 from Charles River Laboratories (Quebec, Canada). At arrival, rats were pair-housed under controlled conditions (12hour light/dark cycle, constant temperature and humidity) with free access to food and water. The experimental protocols were approved by the Animal Care Committee at Western University, Ontario. All procedures were performed in accordance with the Canadian Council on Animal Care guidelines for the appropriate care and use of rats.

3.2.3 Drug Preparation and Administration

Nicotine bitartrate was dissolved in PBS. The Sprague-Dawley rats were injected three times daily from postnatal day (PND) 35 to 44 (10:00/13:00/15:00) with 0.4 mg/kg of nicotine bitartrate, equivalent to 0.13 mg/kg free nicotine, or blank (PBS, vehicle) via subcutaneous injections. The total concentration of daily nicotine exposure (1.2 mg/kg) used in the present study corresponds to the levels of nicotine exposure obtained from smoking about one pack of cigarettes per day, equivalent to moderate to heavy tobacco exposure levels [35]. The rodent exposure age range (PND 35–44) corresponds to mid-adolescence in the rat [36]. Following nicotine exposure, rats were left in the home cage until PND 45 (adolescent groups) or PND 75 (adult groups). On day 45/75, the rats were euthanized by intraperitoneal injection (i.p.) of sodium pentobarbital (240 mg/kg), and the brains were extracted, fresh frozen, and stored in a -80°C freezer until analysis. Animal care, drug administration, and brain extraction were carried out by Roger Hudson, a graduate student in the Laviolette lab, and the brain samples were generously given to the Yeung lab for MALDI MSI.

3.2.4 Sample Preparations for MSI

The brains from the vehicle-treated and nicotine-treated rats were randomly paired and sectioned to a thickness of $10\ \mu\text{m}$ at -20°C at different anatomical points (Bregma +3.00, PFC; +2.04, NAc; -6.00 , HPC) using a cryostat (CM 1850, Leica Biosystems, Wetzlar, Germany), and the tissue sections from the same anatomical points from the paired vehicle-treated and nicotine-treated rat brains were mounted onto the same ITO-coated glass slide. The number of rats used in each group was as follows: vehicle-treated ($n = 5$) and nicotine-

treated adolescent rats (n = 5) for the effect of chronic adolescent nicotine exposure on the adolescent rat brain studies; vehicle-treated (n = 4) and nicotine-treated adult rats (n = 4) were used for the effects of chronic adolescent nicotine exposure on the adult rat brain studies. Prior to matrix deposition, the slides were dried in a vacuum desiccator at room temperature for half an hour. ZnO NP dispersion was prepared in ACN/H₂O (50/50%, vol) at a concentration of 10 mg/mL, ultrasonicated for 10 min, and diluted to a concentration of 1 mg/mL. ZnO NP dispersion was then sprayed onto tissue sections using a TM-Sprayer (HTX Technologies, Chapel Hill, NC) at the following conditions: 1.0 mg/mL of ZnO NP dispersion in ACN/H₂O (50/50%, vol), flow rate of 0.05 mL/min, nozzle temperature at 65 °C, moving nozzle velocity of 1200 mm/min, 32 passes, 3 mm line spacing, and pressure of 10 psi, alternating horizontal and vertical positions between passes. After the spraying cycle was finished, the loop and nozzle were cleaned with a solvent mixture of MeOH/H₂O/TFA (50/50/0.1%, vol) at a flow rate of 0.25 mL/min for 40 minutes to remove any aggregates in the sprayer and help maintain run-to-run reproducibility. The default inline filter with a 2 μm pore size (Valco Instruments, Houston, TX) was replaced regularly for maintenance purposes as recommended by the manufacturer.

3.2.5 MALDI MSI Analysis and Data Processing

A Sciex 5800 MALDI TOF/TOF mass spectrometer (Framingham, MA) equipped with a 349 nm Nd: YLF laser with a pulse rate at 400 Hz was used, and images were acquired with Sciex TOF-TOF Series Explorer and TOF-TOF Imaging. For MS mass calibration, 0.75 μL of 5.5 mg/mL CHCA solution containing ACN/H₂O/TFA (50/50/0.1%, vol) was spotted, and the calibration was based on the following ions with m/z : [CHCA - H₂O + H]⁺

at 170.04 Da, [CHCA + H]⁺ at 190.05 Da, [CHCA + Na]⁺ at 212.03 Da, [CHCA – H + 2Na]⁺ at 234.01 Da, and [2CHCA + H]⁺ at 379.09 Da. Images of tissue sections were acquired at the raster step of 80 μm from 50 to 500 Da in the positive ionization mode. The number of shots applied for imaging in each pixel was between 30 and 70. The laser intensity for MSI was optimized based on the number of signals from an *m/z* range of 50 to 500 Da, peak resolution, and signal-to-noise ratios (S/N).

For neurotransmitter identification, the *m/z* list was generated from multiple individual spectra across the entire region of scanned images. Structural identification was carried out by performing MS/MS on the tissue samples. MSiReader (1.02), developed by North Carolina State University [[37]], was used to process and display the ion distributions within tissue sections and to export the data from the ROI for quantitation. Ion images were created within an *m/z* window of 0.1 Da.

For relative quantitation, mass spectra were generated by exporting the averaged *m/z* and intensity values from the ROI. The ROI include the PrL and IL from the PFC section, the NAcC and NAcSh from the NAc section, and the DS and VS from the HPC section. The areas of the peaks corresponding to [GABA + K]⁺ at *m/z* 142.03, [glutamic acid + K]⁺ at *m/z* 186.02, and the signal at *m/z* 192.04 were integrated with baseline subtraction, and the peak area ratios between the nicotine-treated and vehicle-treated rat brains were obtained using Microsoft Office Excel 2010 (Microsoft, Redmond, WA).

3.2.6 Statistical Analysis

Four (adult group) or five (adolescent group) biological replicates were measured, and the nicotine/vehicle ratios from the left and right hemispheres were calculated separately, resulting in either eight (adult group) or ten (adolescent group) ratios. However, one hemisphere in the adolescent group was unusable, resulting in seven ratios obtained from the VS. For each neurotransmitter in each ROI, the mean of the peak area ratios as well as their 95% confidence interval (CI) were calculated. Next, we performed the Student's t-test (one sample t-test). In all cases, $p < 0.05$ was considered statistically significant.

3.2.7 Sample Preparations for LC–MS

Fresh rat brains were trimmed to a thickness of 1 mm from Bregma +2.00 mm to +1.00 mm using a brain matrix designed for rat brains. The corpus callosum, which consists of the white matter tracts connecting the two cerebral hemispheres, and the NAc (grey matter) were then punched and fresh frozen. Twenty-eight milligrams of the frozen brain samples containing either white matter or grey matter region was homogenized in 100 μ L of prechilled MeOH/H₂O (50/50%, vol), using a tissue grinder pestle in a 1.5 mL microtube, followed by centrifugation (Sorvall Legend Micro 21, Thermo Scientific, Waltham, MA) at 13 000 x g for 20 min, at 4 °C. Fifty microliters of the supernatant was transferred into another microtube and then spun in a vacuum concentrator for 3 hours at 43 °C until dry. The aqueous extracts of the tissue samples were finally reconstituted in 50 μ L of MeOH/H₂O (50/50%, vol) after centrifugation for 20 min at 13 000 x g and 4 °C.

3.2.8 LC–MS Analysis and Data Processing

LC–MS/MS analysis was performed with an Agilent 1290 HPLC system coupled to a Q-Exactive Quadrupole Orbitrap mass spectrometer (Thermo Scientific, Waltham, MA). Chromatographic conditions consisted of an Eclipse Plus C18 RRHD column (2.1×100 mm, $1.8 \mu\text{m}$; Agilent Technologies, Santa Clara, CA) or a HILIC-Z column (2.1×100 mm, $2.7 \mu\text{m}$; Agilent Technologies, Santa Clara, CA) maintained at $35 \text{ }^\circ\text{C}$ using established gradient programs. The mobile phase for the C18 column consisted of water with 0.1% formic acid (A) and acetonitrile with 0.1% formic acid (B). Mobile phase B was held at 0% B for 0.5 min before increasing to 100% over 3.5 min and held at 100% for 2.5 min before returning to 0% B over 0.5 min. The mobile phase for the HILIC-Z column consisted of 20 mM ammonium formate in water (A) and 20 mM ammonium formate in 90% acetonitrile (B) operating with the following gradients: 0 min, 100% B; 0.5 min, 100% B; 5.3 min, 80% B; 9.5 min, 30% B; 12.5 min, 30% B, 13.5 min 100% B and 17 min, 100% B. The brain metabolite extracts were injected with volumes of 5 and $3 \mu\text{L}$ and separated at flow rates of 0.3 and 0.35 mL/min , respectively, on the C18 and HILIC columns.

Heated electrospray ionization was used in the positive ionization mode with the following settings: capillary voltage, 3.9 kV; capillary temperature, $400 \text{ }^\circ\text{C}$; sheath gas, 17 units; auxiliary gas, 8 units; probe heater temperature, $450 \text{ }^\circ\text{C}$; S-Lens RF level, 50%. MS data were acquired using untargeted data-dependent acquisition (DDA) that included a full MS scan at a resolution of 35 000 with a scan range of 70–1000 m/z ; automatic gain control (AGC) target of 1×10^6 ; a maximum injection time (IT) of 128 ms. The five highest intensity ions were selected from each full scan for MS/MS analysis using a 1.2 Da

isolation window and were acquired using the following conditions: resolution, 17 500; AGC target, 1×10^6 ; max IT, 64 ms; stepped normalized collision energy (NCE), 20/35; intensity threshold, 2×10^5 ; dynamic exclusion, 7 s. Raw data files were imported into MZmine. The m/z values of the precursor ions and fragment pattern (MS/MS spectra) were used for the identification of metabolites. Metabolites were identified using various metabolite databases, such as the METLIN (metlin.scripps.edu) and Kyoto Encyclopedia of Genes and Genomes (KEGG, www.genome.jp/kegg).

3.3 Results and Discussion

3.3.1 Identification and Spatial Distribution of Neurotransmitters in the Rat Brain Sections

The identification of neurotransmitters was determined by searching the m/z list within 50 ppm against the theoretical m/z values of neurotransmitters, based on adducts with K^+ . We focused on several major neurotransmitters, including GABA, glutamic acid, and dopamine. The identification of the peaks was then verified by the isotope peak patterns from carbon and potassium. MS/MS was carried out on the brain tissue sections for structural confirmation, where the MS/MS spectra of tentatively identified GABA, glutamate, and dopamine are shown in Figure 3.3. Those neurotransmitters were manually identified by comparing MS/MS fragmentation spectra to the standard MS/MS spectra in the METLIN Metabolomics Database as well as the prediction of cleavage sites.

The product-ion spectrum of GABA from the rat brain at m/z 142.03 $[M + K]^+$ is shown in Figure 3.3a. The peak observed at m/z 125.00 $[M - NH_3 + K]^+$ corresponds to the loss of NH_3 from the molecular ions. Figure 3.3b represents the potassiated molecular ions of glutamic acid at m/z 186.02 $[M + K]^+$ with a loss of H_2O or CO_2NH_3 at m/z 168.01 $[M - H_2O + H]^+$ and at m/z 125.00 $[M - CO_2NH_3 + H]^+$. The ion images of the neurotransmitters in Figures 3.4 and 3.5 show the structure of adolescent and adult rat brains at various anatomical points with distinguishable ion distributions in different compartments of brain sections. The grey matter of the rat brain can be differentiated by ion images of $[GABA + K]^+$ at m/z 142.03, while $[glutamic\ acid + K]^+$ at m/z 186.02 shows a more uniform distribution of ions across the tissue sections, agreeing with the localization of GABA and

glutamic acid in the rat brains in other work [38-40]. In addition, the presence of GABA and glutamate was confirmed by the metabolite list created from an LC–MS analysis of brain samples in Chapter 2. All those verified the existence of those neurotransmitters in the brain.

The MS/MS spectrum of tentatively identified dopamine is not informative because of the low intensity of molecular ions. The removal of NH_3 in the fragmentation pattern at m/z 175.02 $[\text{M} - \text{NH}_3 + \text{K}]^+$ in Figure 3.3c agrees with the fragments acquired from the dopamine standard (not shown). Regardless, the ion image of tentatively assigned $[\text{dopamine} + \text{K}]^+$ at m/z 192.04 shows that the molecule is specifically localized in the white matter region of the rat brain, conflicting with the fact that the grey matter contains the cell bodies of neurons that secrete neurotransmitters [41] as well as the distribution of dopamine in other imaging work [38, 42, 43]. The greater abundance of dopamine in the grey matter region verified by LC–MS/MS confirms that the signal at m/z 192.04 comes from another molecule. However, the identification of the molecule remains inconclusive given that a great number of possible identities are assigned based on m/z values. Additional MS/MS spectra need to be acquired to help with the identification.

Based on our prior experience, in the mass range from 500 to 1000 Da, lipids are the dominant molecules present in brain tissues and could fragment into lower molecular weight molecules during laser ablation. Another hypothesis is that the peak at m/z 192.04 comes from the fragmentation of lipids. To validate this hypothesis, we acquired the ion images from a mouse brain section from m/z 50 to 1000 and monitored the signals between

m/z 500 and 1000 that have the same ion distribution as the peak at m/z 192.04 in the section. It was found that signals at m/z 766.4 and 782.4 have an almost identical ion distribution as the peak at m/z 192.04. However, without acquiring the MS/MS spectra from those signals, we cannot conclude that the peak at m/z 192.04 is generated from lipid fragmentation. Overall, more experiments will need to be conducted to help with the identification of the peak. For the completeness of this study, we still include the quantitation results from the peak at m/z 192.04 in the later sections.

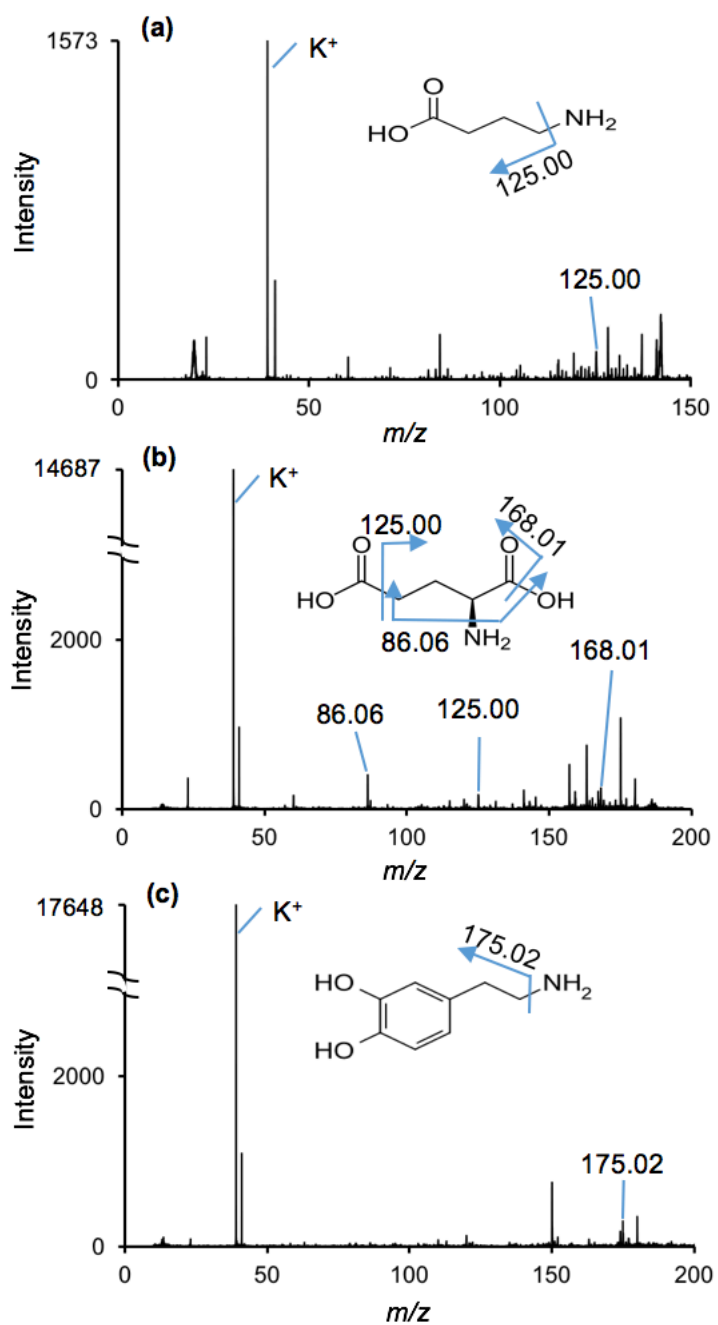


Figure 3.3. MS/MS spectra of (a) [GABA + K]⁺ at m/z 142.03, (b) [glutamate + K]⁺ at m/z 186.02, and (c) the signal at m/z 192.04 acquired from the rat brain sections with ZnO NP-assisted laser desorption ionization mass spectrometry imaging (LDI MSI).

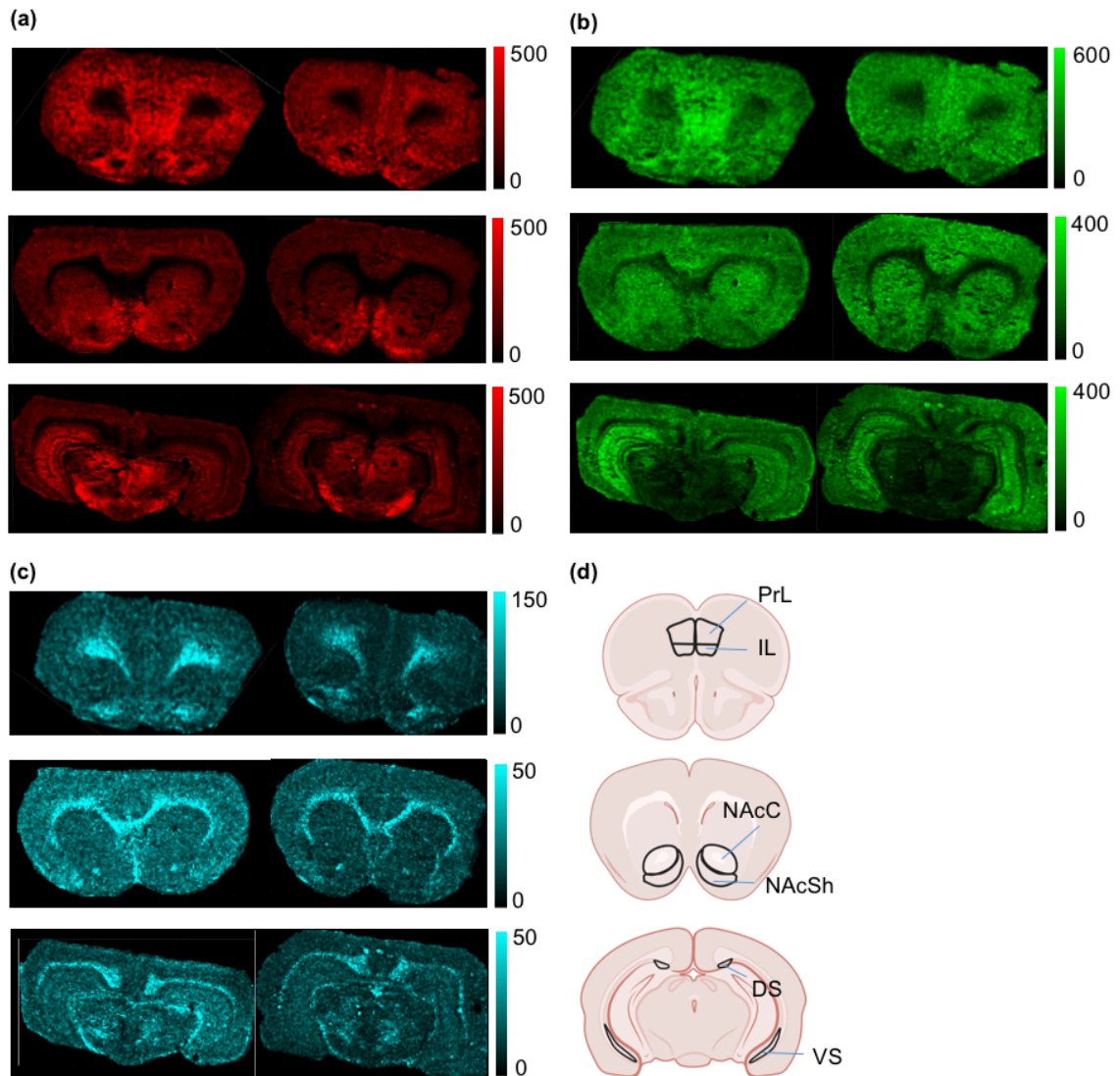


Figure 3.4. Ion images of vehicle-treated (left) or nicotine-treated (right) tissue sections from the adolescent rat brains acquired with ZnO NP-assisted LDI MSI, (a) [GABA + K]⁺ at m/z 142.03, (b) [glutamate + K]⁺ at m/z 186.02, and (c) the signal at m/z 192.04 and (d) schematic diagrams showing the ROI (PrL (prelimbic cortex), IL (infralimbic cortex), NAcC (nucleus accumbens core), NAcSh (nucleus accumbens shell), DS (dorsal subiculum), and VS (ventral subiculum)) are presented (top to bottom: Bregma +3.00 mm, PFC; +2.04 mm, NAc; -6.00 mm, HPC; Paxinos and Watson Atlas; raster size of 80 μ m).

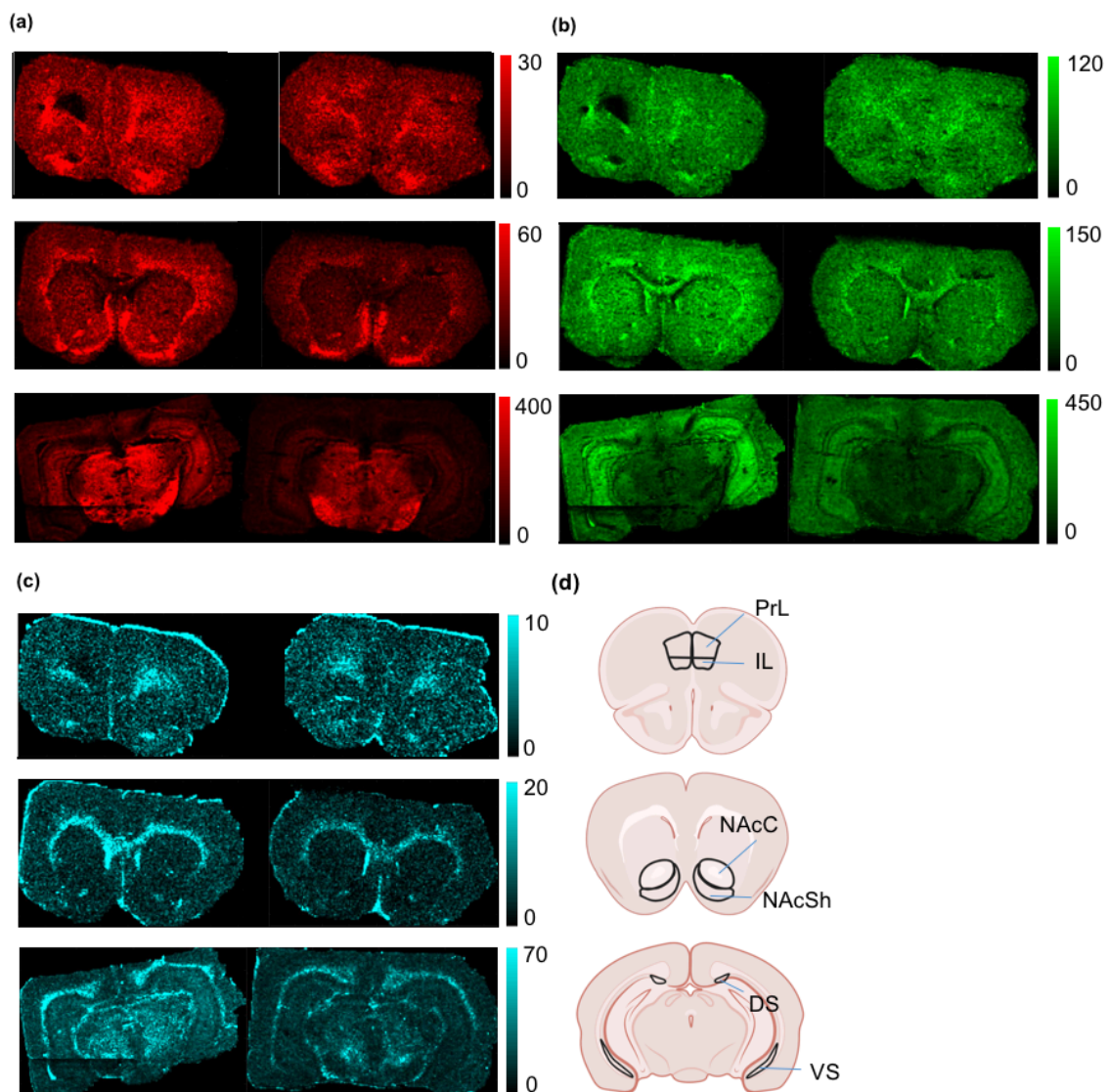


Figure 3.5. Ion images of **vehicle-treated (left)** or **nicotine-treated (right)** tissue sections from the adult rat brains acquired with ZnO NP-assisted LDI MSI, **(a)** [GABA + K]⁺ at m/z 142.03, **(b)** [glutamate + K]⁺ at m/z 186.02, and **(c)** the signal at m/z 192.04 and **(d)** schematic diagrams showing the ROI (PrL, IL, NAcC, NAcSh, DS, and VS) are presented (top to bottom: Bregma +3.00 mm, PFC; +2.04 mm, NAc; -6.00 mm, HPC; Paxinos and Watson Atlas; raster size of 80 μ m).

3.3.2 Relative Quantitation of Neurotransmitters between the Nicotine-treated and Vehicle-treated Rat Brains

To allow direct comparison between the vehicle-treated and drug-treated tissue samples, one sample of each group (vehicle-treated or nicotine-treated) was put on one slide to enable all subsequent sample preparations and MS measurement to be identical. Namely, ZnO NP dispersion was deposited on the vehicle-treated and nicotine-treated samples in one spray run, and the same laser energy was used to image brain samples from both groups. The averaged m/z and intensity values were generated from the ROI to calculate the peak area, and the peak area ratios between the nicotine-treated and vehicle-treated brains from the left and right hemispheres were calculated separately. Biological replicates were measured to capture random biological variations and help identify true biological differences. For every neurotransmitter in each ROI, a series of peak area ratios resulted from the biological replicates were then used to calculate the mean of the ratios, their 95% CI, and p-values. When the geometric mean of the ratios is less than 1, decreased relative signals are found in the drug-treated vs vehicle-treated groups, and vice versa. The procedures to conduct relative quantitation of neurotransmitters between the drug-treated and vehicle-treated samples are shown in Figure 3.6.

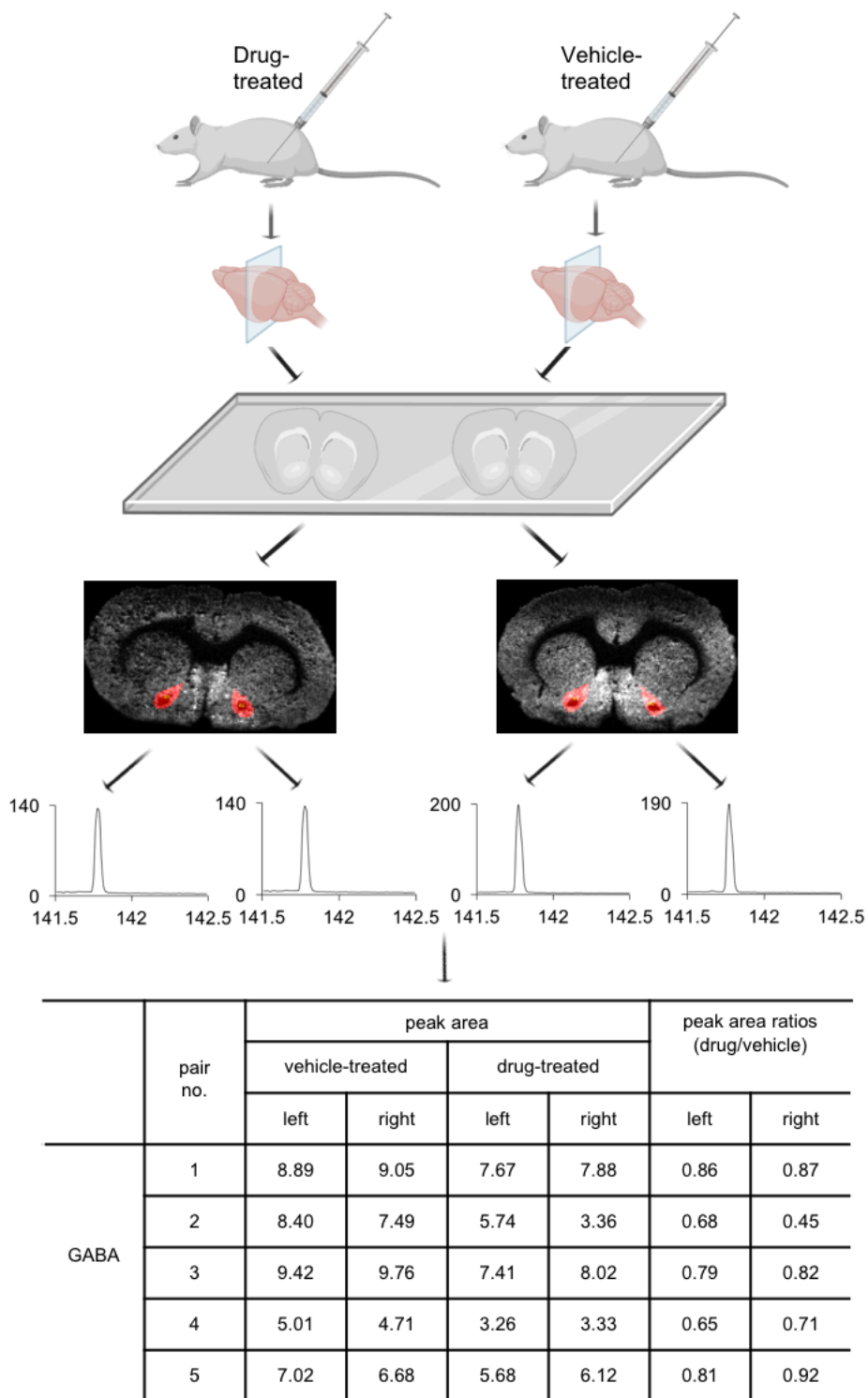


Figure 3.6. Schematic diagram shows the procedures for relative quantitation of neurotransmitters between the **drug-treated** and **vehicle-treated** brains.

3.3.2.1 Relative Quantitation of Neurotransmitters in the Brains from Adolescent Rats Subjected to Chronic Adolescent Nicotine Exposure

We first examined the relative neurotransmitter signal changes between the nicotine-treated and vehicle-treated brains from the adolescent rats following chronic adolescent nicotine exposure. We demonstrate the geometric means of the signal peak area ratios of [GABA + K]⁺ at *m/z* 142.03, [Glutamate + K]⁺ at *m/z* 186.02, and the signal at *m/z* 192.04, 95% CIs, and p-values from the Student t-test between the adolescent rats with nicotine injection and vehicle injection in each brain region, including the PrL, IL, NAcC, NAcSh, DS, and VS, in Table 3.1. Compared to the GABA signals obtained from the vehicle-treated rats, significant differences ($p < 0.05$) were found in the PrL, IL, NAcC, and NAcSh (PrL: $p = 1.6E-7$; IL: $p = 1.9E-5$; NAcC: $p = 0.00034$; NAcSh: $p = 2.9E-5$) in the nicotine-treated rats. A decrease of at least 20% was observed in the NAcC and NAcSh and around 30% in the PrL and IL. No significant differences were detected in the DS and VS (DS: $p = 0.47$; VS: $p = 0.22$).

In terms of glutamate, significant differences ($p < 0.05$) were found in the PrL and IL (PrL: $p = 0.0049$; IL: $p = 0.00086$), with 12% and 17% of signal decreases in the PrL and IL, respectively. However, no significant differences were detected in the NAcC, NAcSh, DS, and VS (NAcC: $p = 0.55$; NAcSh: $p = 0.33$; DS: $p = 0.75$; VS: $p = 0.93$). Comparing GABA and glutamate signals, downregulated GABA and glutamate in the PrL and IL, and selective decreases of GABA but not glutamate in the NAcC and NAcSh were found in the adolescent rat brains.

The signal at m/z 192.04 showed significant changes ($p < 0.05$) in the NAcC, NAcSh, and DS (NAcC: $p = 0.033$; NAcSh: $p = 0.010$; DS: $p = 0.0021$). 12% of reduction was observed in the NAcC and around 20% of decrease in the NAcSh and DS. No significant differences were detected in the PrL, IL, and VS (PrL: $p = 0.35$; IL: $p = 0.54$; VS: $p = 0.46$).

When comparing neurotransmitter abundances in the sub-regions of mPFC, NAc, and HPC in the adolescent rat brains, a selective decrease of the signal at m/z 192.04 in the DS but not VS was found. Downregulation of GABA and glutamate in both PrL and IL and downregulation of GABA and the signal at m/z 192.04 in both NAcC and NAcSh were observed.

When taking a close look at the individual peak area ratios of GABA at m/z 142.03, glutamate at m/z 186.02, and the signal at m/z 192.04 in various regions between the nicotine-treated and vehicle-treated brains from the adolescent rats, as shown in Figure 3.7, the fluctuations in individual peak area ratios vary across different ROI and signals, which are a result of fluctuations in individual peak areas from the five biological replicates. As shown in Figure 3.8, for example, the peak areas of GABA in the PrL fluctuated from around 5 to 16 from the five vehicle-treated animals. Regardless, there are no correlations between the fluctuations and the ROI or signal intensity. For every molecule in each ROI, when more individual peak area ratios between the drug-treated and vehicle-treated samples are either larger or smaller than 1, and more individual peak area ratios are far from 1, it is more likely to have a smaller p-value. Visually, when more of the straight lines connecting the two data points from the paired animals are in either an upward or

downward direction, and more of the straight lines have a steep slope, it is more likely to draw the conclusion that the drug-treated samples are significantly different from the vehicle-treated samples.

The signal variations from those biological replicates can be originated from two sources: the technical variations from slightly different matrix densities and instrument performances as well as the biological variations. Generally speaking, when the same absolute measurement error is applied, the relative measurement error (the ratio of absolute measurement error to a measurement) with smaller values is more significant. Similarly, fluctuations in measurement can lead to a more significant relative change of weak signals when compared with strong signals. Therefore, improvement in the detection sensitivity is always preferred. Individual animals following the same drug treatment, can be affected differently, meaning there are always differences in the total neurotransmitter levels between the individual rats that received the same drug treatment. Similar biological variations are present in the vehicle-treated group. By randomly pairing one animal from each group and mounting the brain tissue sections from both groups on the same slide to allow the sample preparation and MS measurement to be identical, the technical variations between the two paired samples are minimized. However, a more positive or negative error is induced due to the biological variations, resulting in more variabilities in the biological variations. In other words, there are compromises between the biological variations and technical variations using this method. Therefore, a large number of biological replicates is important to improve the measurement accuracy.

Table 3.1. The Averaged Peak Area Ratios (Fold Changes) of [GABA + K]⁺ at *m/z* 142.03, [Glutamate + K]⁺ at *m/z* 186.02, and the Signal at *m/z* 192.04, Their 95% CIs, and P-values from the Student T-test in Various ROI between the Nicotine-treated and Vehicle-treated Adolescent Rat Brains (n = 10) Are Presented. The Fold Change ± 95% CI Is Bolded When It Is Significantly Different than 1. P-value Is Bolded When It Is Less Than 0.05.

brain ROI	GABA		glutamate		signal at <i>m/z</i> 192.04	
	fold change	p-value	fold change	p-value	fold change	p-value
prelimbic cortex, PrL	0.70 ± 0.05	1.6E-7	0.88 ± 0.07	0.0049	0.89 ± 0.25	0.35
infralimbic cortex, IL	0.68 ± 0.09	1.9E-5	0.83 ± 0.08	0.00086	0.92 ± 0.27	0.54
nucleus accumbens core, NAcC	0.76 ± 0.10	0.00034	0.97 ± 0.11	0.55	0.88 ± 0.11	0.033
nucleus accumbens shell, NAcSh	0.79 ± 0.06	2.9E-5	0.96 ± 0.10	0.33	0.81 ± 0.13	0.010
dorsal subiculum, DS	1.12 ± 0.36	0.47	1.04 ± 0.31	0.75	0.78 ± 0.12	0.0021
ventral subiculum, VS	0.89 ± 0.20	0.22	0.99 ± 0.17	0.93	0.89 ± 0.31	0.46

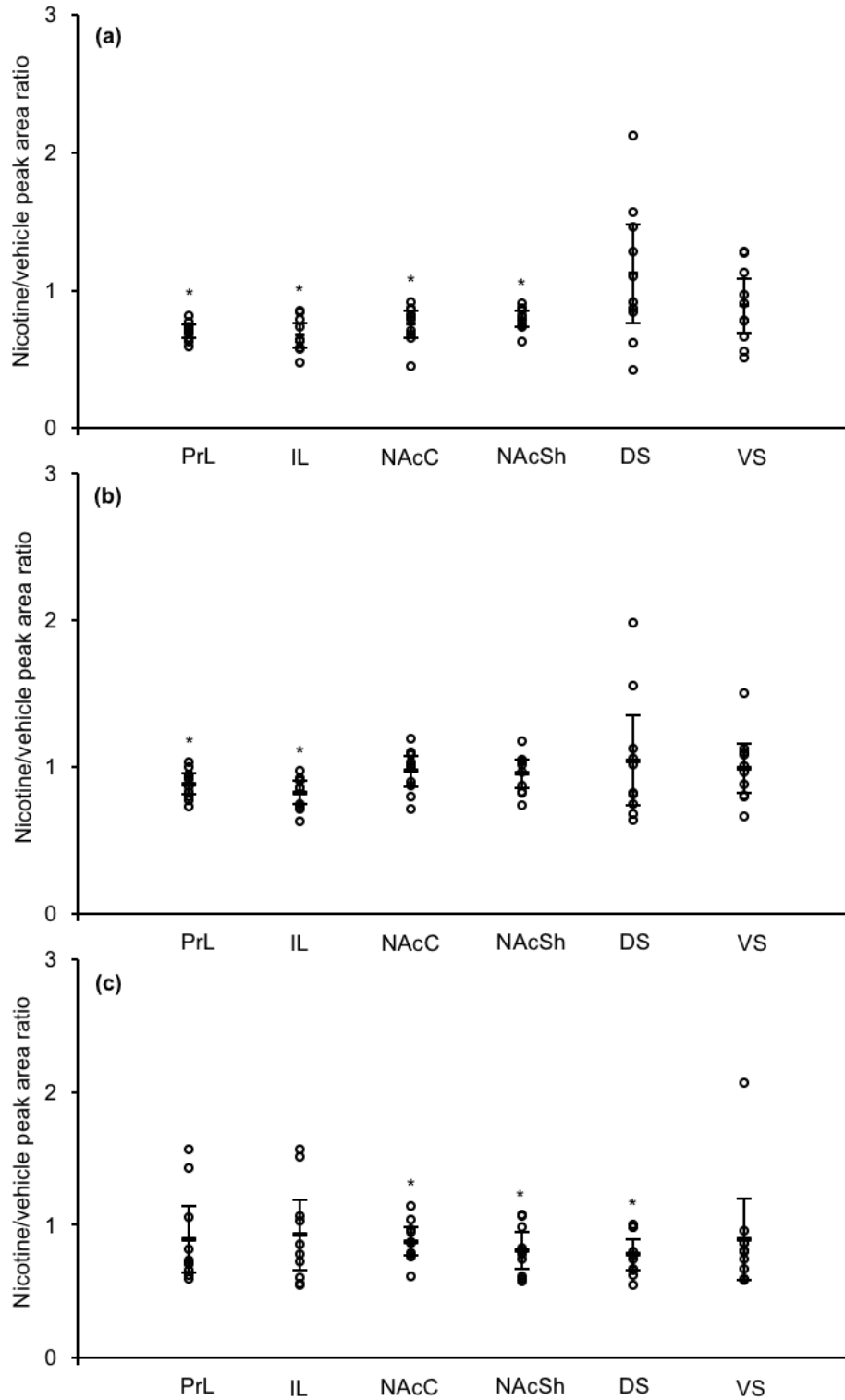


Figure 3.7. The peak area ratios of (a) $[GABA + K]^+$ at m/z 142.03, (b) $[glutamate + K]^+$ at m/z 186.02, and (c) the signal at m/z 192.04 in various brain regions between the nicotine-treated and vehicle-treated brains from the adolescent rats ($n = 10$). The arithmetic mean and a 95% CI of nicotine/vehicle peak area ratios are displayed as a bar. Asterisks indicate the brain regions that featured significant differences using the peak area ratios between the nicotine-treated and vehicle-treated adolescent rat brains in the Student t-test ($*p < 0.05$).

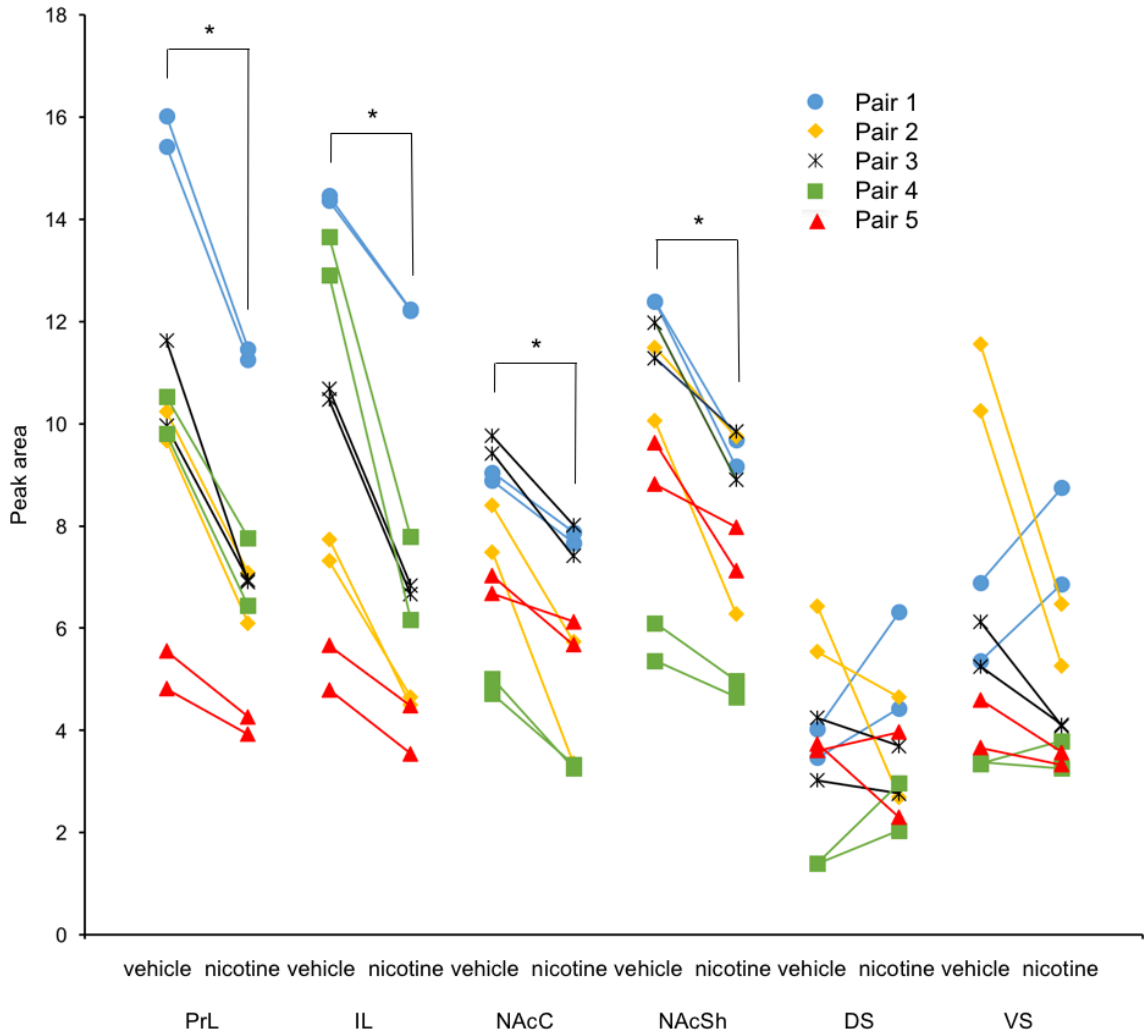


Figure 3.8. The peak areas of $[GABA + K]^+$ at m/z 142.03 in various brain regions from the nicotine-treated and vehicle-treated adolescent rat brains ($n = 10$). Asterisks indicate the brain regions that featured significant differences between the nicotine-treated and vehicle-treated adolescent rat brains in the Student t-test ($*p < 0.05$).

3.3.2.2 Relative Quantitation of Neurotransmitters in the Brains from Adult Rats Subjected to Chronic Adolescent Nicotine Exposure

We next examined the relative neurotransmitter signal changes between the nicotine-treated and vehicle-treated brains from the adult rats 30 days after the chronic administrations of nicotine during adolescence. We demonstrate the geometric means of the signal peak area ratios of [GABA + K]⁺ at *m/z* 142.03, [Glutamate + K]⁺ at *m/z* 186.02, and the signal at *m/z* 192.04, 95% CIs, and p-values from the Student t-test in each brain region, including the PrL, IL, NAcC, NAcSh, DS, and VS, between the adult rats with nicotine injections and vehicle injections from their adolescence in Table 3.2. No significant differences ($p > 0.05$) of GABA signals were detected in the nicotine-treated rats when compared to the vehicle-treated rats in all brain regions (PrL: $p = 0.73$; IL: $p = 0.39$; NAcC: $p = 0.080$; NAcSh: $p = 0.54$; DS: $p = 0.063$; VS: $p = 0.069$).

In terms of glutamate, significant differences ($p < 0.05$) were found in the DS (DS: $p = 0.018$), with a decrease of 34% in the DS in the nicotine-treated rats. However, no significant differences were detected in the PrL, IL, NAcC, NAcSh, and VS (PrL: $p = 0.63$; IL: $p = 0.99$; NAcC: $p = 0.35$; NAcSh: $p = 0.39$; VS: $p = 0.13$). Comparing GABA and glutamate signals, a selective decrease of glutamate but not GABA in the DS was found in the adult rat brains.

The signal at *m/z* 192.04 showed significant differences ($p < 0.05$) in the IL, NAcC, and NAcSh (IL: $p = 0.0013$; NAcC: $p = 0.00064$; NAcSh: $p = 0.0029$), with at least a 50%

decrease in the IL and a 30% decrease in the NAcC and NAcSh. No significant differences were detected in the PrL, DS, and VS (PrL: $p = 0.34$; DS: $p = 0.090$; VS: $p = 0.34$).

When looking at neurotransmitter levels in the sub-regions of mPFC, NAc, and HPC in the adult rat brains, glutamate was found to selectively decrease in the DS but not VS and the signal at m/z 192.04 was found to selectively increase in the IL but not PrL. Downregulation of the signal at m/z 192.04 in both NAcC and NAcSh were observed.

The individual peak area ratios of GABA at m/z 142.03, glutamate at m/z 186.02, and the signal at m/z 192.04 in various brain regions between the nicotine-treated and vehicle-treated brains from the adult rats are shown in Figure 3.9. Similarly, the fluctuations of peak area ratios of those signals changed in various ROI.

Table 3.2. The Averaged Peak Area Ratios (Fold Changes) of [GABA + K]⁺ at *m/z* 142.03, [Glutamate + K]⁺ at *m/z* 186.02, and the Signal at *m/z* 192.04, Their 95% CIs, and P-values from the Student T-test in Various Brain ROI between the Nicotine-treated and Vehicle-treated Adult Rat Brains (n = 8, PrL, IL, NAcC, NAcSh, and DS; n = 7, VS) Are Presented. The Fold Change ± 95% CI Is Bolded When It Is Significantly Different than 1. P-value Is Bolded When It Is Less Than 0.05.

brain ROI	GABA		glutamate		signal at <i>m/z</i> 192.04	
	fold change	p-value	fold change	p-value	fold change	p-value
prelimbic cortex, PrL	1.05 ± 0.31	0.73	1.03 ± 0.15	0.63	0.84 ± 0.36	0.34
infralimbic cortex, IL	1.12 ± 0.32	0.39	1.00 ± 0.12	0.99	0.45 ± 0.24	0.0013
nucleus accumbens core, NAcC	0.89 ± 0.12	0.080	0.95 ± 0.13	0.35	0.67 ± 0.13	0.00064
nucleus accumbens shell, NAcSh	0.94 ± 0.21	0.54	0.94 ± 0.15	0.39	0.66 ± 0.18	0.0029
dorsal subiculum, DS	0.69 ± 0.33	0.063	0.66 ± 0.26	0.018	0.64 ± 0.43	0.090
ventral subiculum, VS	0.76 ± 0.26	0.069	0.86 ± 0.20	0.13	1.79 ± 1.88	0.34

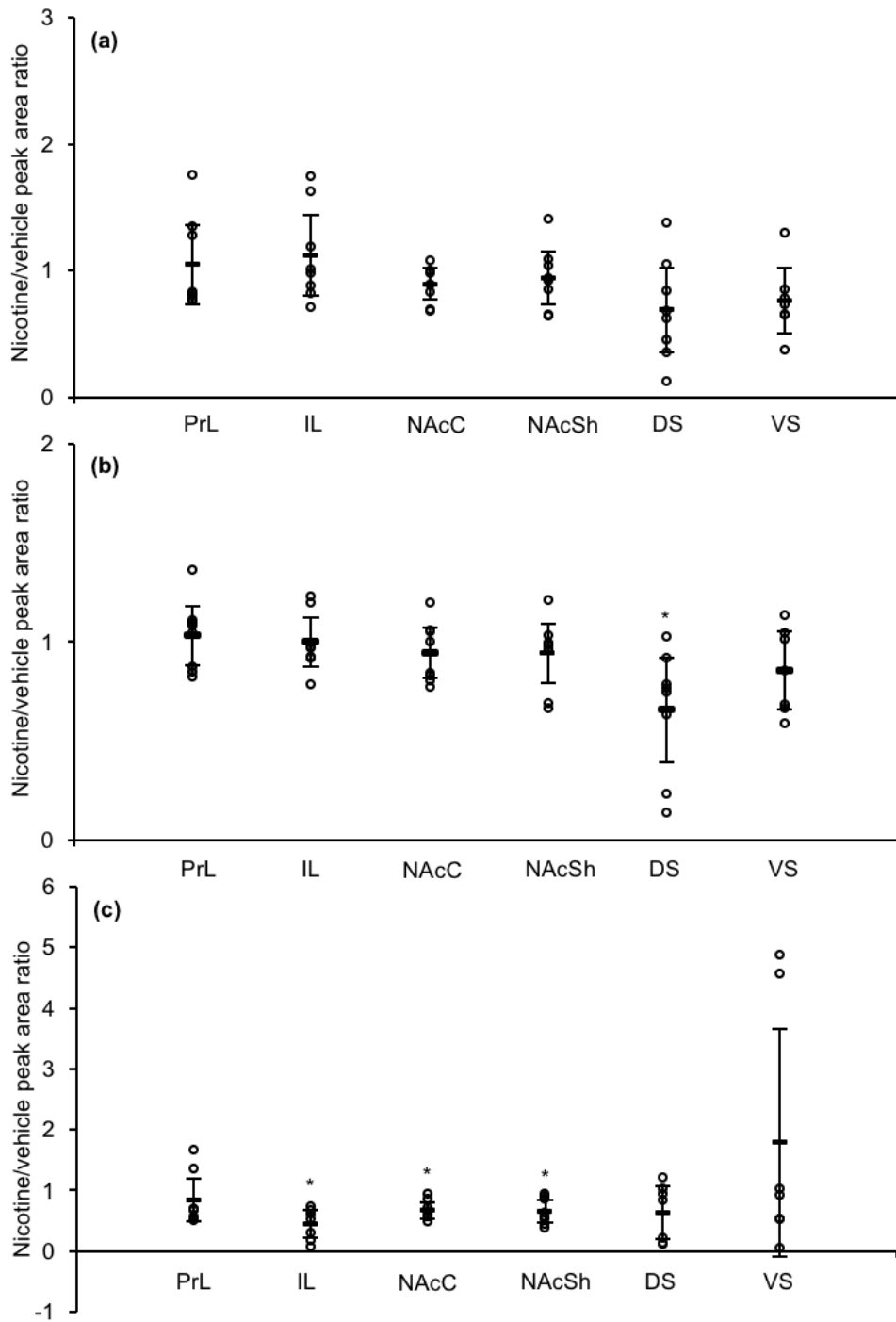


Figure 3.9. The peak area ratios of (a) [GABA + K]⁺ at *m/z* 142.03, (b) [glutamate + K]⁺ at *m/z* 186.02, and (c) the signal at *m/z* 192.04 in various brain regions between the nicotine-treated and vehicle-treated adult rat brains (n = 8, PrL, IL, NAcC, NAcSh, and DS; n = 7, VS). The arithmetic mean and a 95% CI of nicotine/vehicle peak area ratios are displayed as a bar. Asterisks indicate the brain regions that featured significant differences using the peak area ratios between the nicotine-treated and vehicle-treated adult rat brains in the Student t-test (*p < 0.05).

3.3.2.3 Comparison of Relative Quantitation of Neurotransmitters in the Brains from Adolescent and Adult Rats Subjected to Chronic Adolescent Nicotine Exposure

By comparing the relative neurotransmitter signal changes in the brains from the adolescent and adult rats following adolescent chronic nicotine exposure, we found GABA, glutamate, and the signal at m/z 192.04 were affected differently in the two periods in various ROI, as shown in Figure 3.10. The effects of nicotine on the levels of the signal at m/z 192.04 persisted in the NAcC and NAcSh, where the signal showed a decrease in both adolescent and adult nicotine rat brains. The decreased levels of GABA in the PrL, IL, NAcC, and NAcSh in the adolescent rat brains were rebalanced in the adult rat brains, where no significant differences of GABA level were observed between vehicle and nicotine groups. Similarly, nicotine exposure was shown to affect glutamate in the PrL and IL and affect the signal at m/z 192.04 in the DS in the short term, where they both decreased in the adolescent nicotine brains. On the contrary, long-lasting effects of nicotine were developed on glutamate in the DS and on the signal at m/z 192.04 in the IL, where decreased levels of glutamate and the signal at m/z 192.04 were observed in the adult nicotine-treated brains.

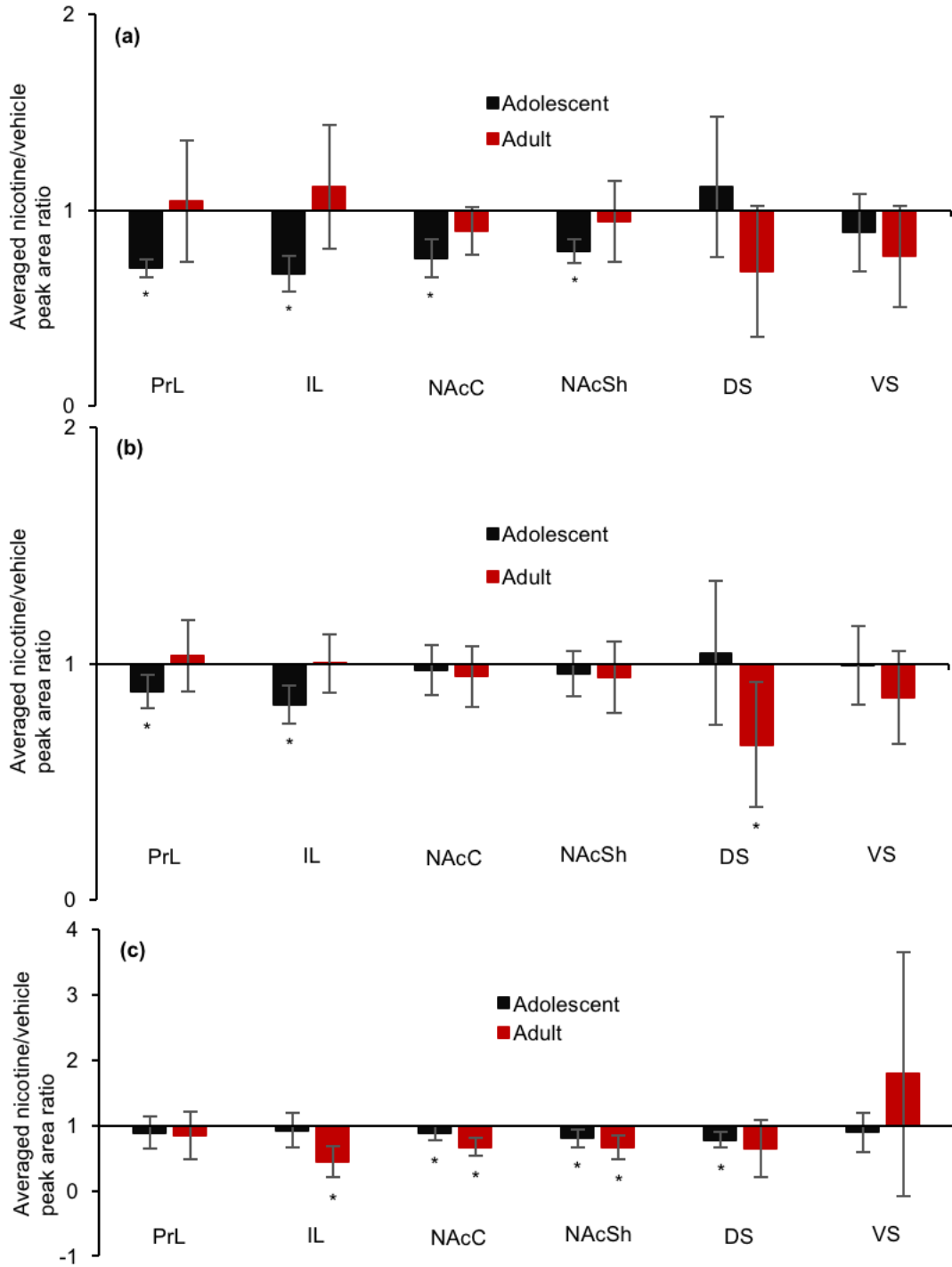


Figure 3.10. Comparison of the averaged signal ratios of (a) $[GABA + K]^+$ at m/z 142.03, (b) $[glutamate + K]^+$ at m/z 186.02, and (c) the signal at m/z 192.04 in various ROI between the nicotine-treated and vehicle-treated brains from the adolescent and adult rats ($n = 10$, adolescent; $n = 8$, PrL, IL, NAcC, NAcSh, and DS; $n = 7$, VS; adult). The averaged arithmetic mean of nicotine/vehicle peak area ratios is displayed as a bar. Each error bar represents a 95% CI of nicotine/vehicle peak area ratios. Asterisks indicate the brain regions that featured significant differences using the peak area ratios between the nicotine-treated and vehicle-treated rat brains in the Student t-test (* $p < 0.05$).

3.3.3 Comparison with Literature

3.3.3.1 Clinical Studies

When compared to nonsmokers, both daily and intermittent smokers exhibited lower concentrations of glutamate in the mPFC [44]. Similarly, we have detected a reduction of glutamate in the PrL and IL (which correspond to sub-regions of the mPFC in human brains) in adolescent rat brains following chronic nicotine exposure during adolescence.

3.3.3.2 Preclinical Studies Using Animal Models

Preclinical studies using rodent animal models have found that chronic adolescent nicotine exposure causes a transient increase in nicotine-simulated GABAergic transmission [45] in the mPFC of adolescent rat brains. A short-term increased level of presynaptic metabotropic glutamate receptor 2 (mGluR2) on mPFC glutamatergic neurons [46], which are activated by glutamate spillover and inhibit further glutamate release, has been observed as well. We observed decreases in the total levels of GABA and glutamate in the subdivisions of mPFC, the PrL and IL, between the nicotine-treated and vehicle-treated adolescent rats.

Chronic adolescent nicotine exposure has been found to upregulate the firing frequency of pyramidal neurons in the mPFC [26] and GABAergic medium spiny neurons in the NAcSh [27] of adult brains in the long term by the Laviolette lab, indicating more glutamate in the mPFC and more GABA in the NAcSh are released. On the other hand, a long-lasting reduction in presynaptic mGluR2 level has been found on mPFC glutamatergic neurons [46], meaning the inhibition of glutamate release by presynaptic mGluR2 was reduced.

However, no significant differences in the total glutamate level in the subdivisions of mPFC, the PrL and IL, and total GABA level in the NAcSh have been found between the nicotine-treated and vehicle-treated adult rat brains.

Nicotine exposure during adolescence disrupts the expression of neuronal nAChRs differently in the short term and long term, ultimately changing the release of GABA, glutamate, and dopamine during the two periods. Nicotine exposure during adolescence causes a transient increase in the adolescent rat mPFC nAChRs containing $\alpha 4$ or $\beta 2$ subunits (24 and 18%, respectively) 24 h after the last nicotine injection, while long-lasting effects are not present in adult rats [45]. We find chronic adolescent nicotine exposure affects GABA and glutamate in the PrL and IL of adolescent brains but not adult brains, which could partially be affected by alterations in the subunits of nAChRs.

We attribute the different observations between our work and previous reports to two possible factors. First, the total neurotransmitter levels were investigated in this work, while the previous reports mainly focused on neurotransmitter release. Second, the studied brain regions are different. In the ref. of [46], mPFC was studied, while we studied the sub-regions of mPFC, the PrL and IL. Altogether, it is expected that we see different results. Further studies are required to help explain the effects of chronic adolescent nicotine exposure on total neurotransmitter abundances in both adolescent and adult brains.

3.4 Conclusion

MALDI MSI enables the simultaneous detection and imaging of neurotransmitters such as GABA and glutamate in multiple brain regions at once and the relative quantitation of neurotransmitters between the drug-treated and vehicle-treated samples in various brain regions. Chronic nicotine exposure during adolescence has been found to modulate GABA levels in the PrL, IL, NAcC, and NAcSh and glutamate levels in the PrL and IL in the adolescent brains. In the adult brains, the alteration in the glutamate levels in the DS has been shown to be different from that in the VS. Altogether, GABA and glutamate levels have been affected differently in the adolescent and adult brains following chronic adolescent THC exposure.

3.5 Reference

- (1) Delvecchio, G.; Stanley, J. A.; Altamura, A. C.; Brambilla, P. *Epidemiology and Psychiatric Sciences* **2017**, *26*, 587-595.
- (2) Wang, H.; Tan, L.; Wang, H. F.; Liu, Y.; Yin, R. H.; Wang, W. Y.; Chang, X. L.; Jiang, T.; Yu, J. T. *Journal of Alzheimers Disease* **2015**, *46*, 1049-1070.
- (3) Drago, T.; O'Regan, P. W.; Welaratne, I.; Rooney, S.; O'Callaghan, A.; Malkit, M.; Roman, E.; Levins, K. J.; Alexander, L.; Barry, D.; O'Hanlon, E.; O'Keane, V.; Roddy, D. W. *Systematic Reviews* **2018**, *7*.
- (4) Merritt, K.; Egerton, A.; Kempton, M. J.; Taylor, M. J.; McGuire, P. K. *Jama Psychiatry* **2016**, *73*, 665-674.
- (5) Trushina, E.; Mielke, M. M. *Biochimica Et Biophysica Acta-Molecular Basis of Disease* **2014**, *1842*, 1232-1239.
- (6) Zhang, X. W.; Li, Q. H.; Xu, Z. D.; Dou, J. J. *Rsc Advances* **2020**, *10*, 3092-3104.
- (7) Ren, J. L.; Zhang, A. H.; Kong, L.; Wang, X. J. *Rsc Advances* **2018**, *8*, 22335-22350.
- (8) Gowda, G. A. N.; Djukovic, D. *Methods in molecular biology (Clifton, N.J.)* **2014**, *1198*, 3-12.
- (9) Emwas, A. H.; Roy, R.; McKay, R. T.; Tenori, L.; Saccenti, E.; Gowda, G. A. N.; Raftery, D.; Alahmari, F.; Jaremko, L.; Jaremko, M.; Wishart, D. S. *Metabolites* **2019**, *9*.
- (10) Palmer, A.; Trede, D.; Alexandrov, T. *Metabolomics* **2016**, *12*.
- (11) Bodzon-Kulakowska, A.; Suder, P. *Mass Spectrometry Reviews* **2016**, *35*, 147-169.
- (12) Rzagalinski, I.; Volmer, D. A. *Biochimica Et Biophysica Acta-Proteins and Proteomics* **2017**, *1865*, 726-739.
- (13) Tobias, F.; Hummon, A. B. *Journal of Proteome Research* **2020**, *19*, 3620-3630.

- (14) Taylor, A. J.; Dexter, A.; Bunch, J. *Analytical Chemistry* **2018**, *90*, 5637-5645.
- (15) Sun, N.; Walch, A. *Histochemistry and Cell Biology* **2013**, *140*, 93-104.
- (16) Miura, D.; Fujimura, Y.; Yamato, M.; Hyodo, F.; Utsumi, H.; Tachibana, H.; Wariishi, H. *Analytical Chemistry* **2010**, *82*, 9789-9796.
- (17) Jung, J. W.; Lee, M. S.; Choi, H. J.; Jung, S.; Lee, Y. J.; Hwang, G. S.; Kwon, T. H. *American Journal of Physiology-Renal Physiology* **2016**, *310*, F1317-F1327.
- (18) Eto, F.; Sato, S.; Setou, M.; Yao, I. *Scientific Reports* **2020**, *10*.
- (19) Prideaux, B.; Dartois, V.; Staab, D.; Weiner, D. M.; Goh, A.; Via, L. E.; Barry, C. E.; Stoeckli, M. *Analytical Chemistry* **2011**, *83*, 2112-2118.
- (20) Schulz, S.; Gerhardt, D.; Meyer, B.; Seegel, M.; Schubach, B.; Hopf, C.; Matheis, K. *Analytical and Bioanalytical Chemistry* **2013**, *405*, 9467-9476.
- (21) Buck, A.; Halbritter, S.; Spath, C.; Feuchtinger, A.; Aichler, M.; Zitzelsberger, H.; Janssen, K. P.; Walch, A. *Analytical and Bioanalytical Chemistry* **2015**, *407*, 2107-2116.
- (22) Sun, N.; Fernandez, I. E.; Wei, M.; Wu, Y.; Aichler, M.; Eickelberg, O.; Walch, A. *Histochemistry and Cell Biology* **2016**, *145*, 201-211.
- (23) Aikawa, H.; Hayashi, M.; Ryu, S.; Yamashita, M.; Ohtsuka, N.; Nishidate, M.; Fujiwara, Y.; Hamada, A. *Scientific Reports* **2016**, *6*.
- (24) Porta, T.; Grivet, C.; Kraemer, T.; Varesio, E.; Hopfgartner, G. *Analytical Chemistry* **2011**, *83*, 4266-4272.
- (25) Boudon, S. M.; Morandi, G.; Prideaux, B.; Staab, D.; Junker, U.; Odermatt, A.; Stoeckli, M.; Bauer, D. *Journal of the American Society for Mass Spectrometry* **2014**, *25*, 1803-1809.

- (26) Jobson, C. L. M.; Renard, J.; Szkudlarek, H.; Rosen, L. G.; Pereira, B.; Wright, D. J.; Rushlow, W.; Laviolette, S. R. *Cerebral Cortex* **2019**, *29*, 3140-3153.
- (27) Hudson, R.; Green, M.; Wright, D. J.; Renard, J.; Jobson, C. E. L.; Jung, T.; Rushlow, W.; Laviolette, S. R. *Addiction Biology* **2021**, *26*.
- (28) Feduccia, A. A.; Chatterjee, S.; Bartlett, S. E. *Frontiers in Molecular Neuroscience* **2012**, *5*.
- (29) Dani, J. A.; Bertrand, D. *Annual Review of Pharmacology and Toxicology* **2007**, *47*, 699-729.
- (30) Pistillo, F.; Clementi, F.; Zoli, M.; Gatti, C. *Progress in Neurobiology* **2015**, *124*, 1-27.
- (31) Hurst, R.; Rollema, H.; Bertrand, D. *Pharmacology & Therapeutics* **2013**, *137*, 22-54.
- (32) Fanselow, M. S.; Dong, H. W. *Neuron* **2010**, *65*, 7-19.
- (33) Franklin, K. B. J.; Chudasama, Y. *Mouse Nervous System* **2012**, 727-735.
- (34) Pavuluri, M.; Volpe, K.; Yuen, A. *Aims Neuroscience* **2017**, *4*, 52-70.
- (35) Murrin, L. C.; Ferrer, J. R.; Zeng, W. Y.; Haley, N. J. *Life Sciences* **1987**, *40*, 1699-1708.
- (36) Spear, L. P. *Neuroscience and Biobehavioral Reviews* **2000**, *24*, 417-463.
- (37) Robichaud, G.; Garrard, K. P.; Barry, J. A.; Muddiman, D. C. *Journal of the American Society for Mass Spectrometry* **2013**, *24*, 718-721.
- (38) Shariatgorji, M.; Nilsson, A.; Goodwin, R. J. A.; Kallback, P.; Schintu, N.; Zhang, X. Q.; Crossman, A. R.; Bezard, E.; Svenningsson, P.; Andren, P. E. *Neuron* **2014**, *84*, 697-707.

- (39) Esteve, C.; Tolner, E. A.; Shyti, R.; van den Maagdenberg, A.; McDonnell, L. A. *Metabolomics* **2016**, *12*, 9.
- (40) Sun, C. L.; Liu, W.; Mu, Y.; Wang, X. *Talanta* **2020**, *209*, 9.
- (41) Butt, A. M.; Fern, R. F.; Matute, C. *Glia* **2014**, *62*, 1762-1779.
- (42) Shariatgorji, M.; Nilsson, A.; Fridjonsdottir, E.; Vallianatou, T.; Kallback, P.; Katan, L.; Savmarker, J.; Mantas, I.; Zhang, X. Q.; Bezaud, E.; Svenningsson, P.; Odell, L. R.; Andren, P. E. *Nature Methods* **2019**, *16*, 1021-1028.
- (43) Shariatgorji, R.; Nilsson, A.; Strittmatter, N.; Vallianatou, T.; Zhang, X.; Svenningsson, P.; Goodwin, R. J. A.; Andren, P. E. *Journal of the American Society for Mass Spectrometry* **2020**, *31*, 2553-2557.
- (44) Faulkner, P.; Paioni, S. L.; Kozhuharova, P.; Orlov, N.; Lythgoe, D. J.; Daniju, Y.; Morgenroth, E.; Barker, H.; Allen, P. *Addiction Biology* **2021**, *26*.
- (45) Counotte, D. S.; Goriounova, N. A.; Moretti, M.; Smoluch, M. T.; Irth, H.; Clementi, F.; Schoffelmeer, A. N. M.; Mansvelder, H. D.; Smit, A. B.; Gotti, C.; Spijker, S. *Faseb Journal* **2012**, *26*, 1810-1820.
- (46) Counotte, D. S.; Goriounova, N. A.; Li, K. W.; Loos, M.; van der Schors, R. C.; Schetters, D.; Schoffelmeer, A. N. M.; Smit, A. B.; Mansvelder, H. D.; Pattij, T.; Spijker, S. *Nature Neuroscience* **2011**, *14*, 417-419.

Chapter 4: Investigation of Effects of Chronic Adolescent Δ -9-Tetrahydrocannabinol Exposure on Neurotransmitter Abundance in Adolescent and Adult Rat Brains Using Laser Desorption/Ionization Mass Spectrometry Imaging Assisted with ZnO Nanoparticles

4.1 Introduction

Marijuana is the one of the most frequently used drugs by adolescents. According to the Substance Abuse and Mental Health Services Administration, more than 3 million adolescents aged 12 to 17 reported marijuana use during 2018 in the United States. Adolescence is a critical period for brain development when important structural and functional changes occur [1]. Evidence has shown that chronic adolescent cannabis exposure may increase the risk of developing neuropsychiatric diseases like depression and schizophrenia at adulthood [2,3]. Moreover, neuroimaging studies using magnetic resonance imaging (MRI) and functional magnetic resonance imaging (fMRI) suggest that adolescent exposure to marijuana disrupts the structures and functions in the regions associated with neuropsychiatric diseases, such as the prefrontal cortex (PFC), striatum, and hippocampus (HPC), which are related to executive functioning, reward processing, and memory respectively [4,5]. However, the neurobiological processes underlying are still unclear.

The Laviolette lab at Western University is studying the impacts of chronic adolescent Δ -9-tetrahydrocannabinol (Δ -9-THC, THC), the primary psychoactive component of marijuana, on normal brain development using animal models [6,7]. The studies focus on a number of brain areas involved in the reward system [8] including the PFC, the nucleus accumbens (NAc, ventral striatum) in the forebrain, and the HPC and ventral tegmental area (VTA) in the midbrain. The PFC is one of the last areas to reach maturity [9]. During adolescence, the synaptic pruning (which eliminates extra synaptic connections) and myelination (which increases the efficiency of synaptic transmission) occur in the PFC.

Hence, neural connections, between the PFC and NAc, thalamus, HPC, and VTA, as shown in Figure 4.1 [10-13], are strengthened. GABAergic neurons, glutamatergic neurons, and dopaminergic neurons in the central nervous system (CNS), which are highly involved in reward system, are being studied.

Altered behaviours, neuron activities, and protein expressions were observed in adult rats following adolescent THC exposure in the Laviolette lab. Adolescent THC exposure has been found to induce long-term abnormalities in social motivation and social recognition during the social interaction test as well as in exploratory behaviour in an open field test [6,7]. Anxiety-like behaviours in a light/dark box and recognition memory deficits have been reported in adult rats subjected to adolescent THC exposure [6,7]. The medial prefrontal cortex (mPFC) showed a significant loss of glutamic acid decarboxylase-67 (GAD-67), the enzyme that catalyzes the decarboxylation of glutamate to produce γ -aminobutyric acid (GABA) [6]. Meanwhile, enhanced firing frequency of mPFC excitatory pyramidal neurons and VTA dopaminergic neurons has been found using electrophysiological tools [6,7]. Furthermore, several proteins involved in the signalling pathways, including glycogen synthase kinase-3 (GSK-3), β -catenin, and ribosomal protein S6 kinase beta-1 (p70S6K), have been reported to decrease dramatically in the PFC [7].

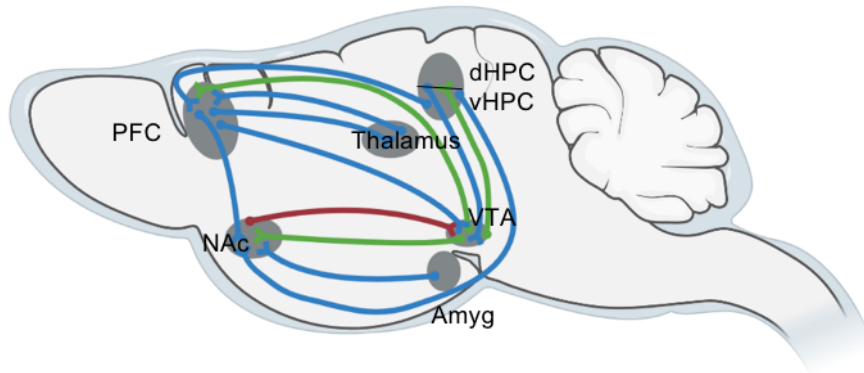


Figure 4.1. A simplified diagram of the main connections to and from the PFC (prefrontal cortex), NAc (nucleus accumbens), thalamus, dHPC (dorsal hippocampus), vHPC (ventral hippocampus), Amyg (amygdala), and VTA (ventral tegmental area), in a sagittal section of a rodent brain. GABAergic, glutamatergic, and dopaminergic projections are in red, blue, and green, respectively. Figure created using BioRender (<https://biorender.com/>).

Nevertheless, the effects of chronic THC exposure during adolescence on neurotransmitter abundance in various brain regions remain elusive. THC acts as a partial agonist of cannabinoid type 1 receptors (CB1Rs), one of the most widely-expressed G-protein-coupled (GPC) receptors in the CNS. The CB1Rs are mainly expressed in the PFC, VTA, substantia nigra (SN), HPC, and cerebellum [14]. The release of GABA, glutamate, and dopamine in the CNS can be regulated via the endocannabinoid (eCB) system, which consists of cannabinoid receptors (CBRs), endogenous cannabinoids, namely eCBs such as anandamide (N-arachidonylethanolamine, AEA) and 2-arachidonoyl glycerol (2-AG), and the enzymes involved in their metabolism [15]. THC affects the neurotransmitter systems in the CNS by disrupting the eCB system during brain development. THC may alter the neurotransmitter abundance in the CNS by direct interaction with the presynaptic CB1Rs. Specifically, the activation of CB1Rs at the presynaptic sites of GABAergic neurons directly inhibits the release of GABA in the rodent's PFC [16], NAc [17], HPC [18], VTA [19], and SN [20]. The release of glutamate from glutamatergic neurons is mediated by presynaptically localized CB1Rs in several brain regions such as the PFC [21], NAc [22], HPC [23], and VTA [19], as well as downstream N-methyl-D-aspartate (NMDA) receptor signalling [24]. Besides, THC may alter neurotransmitter abundance by indirect interaction through the inputs of other neurons from the same or different brain regions. For example, the GABAergic medium spiny neurons in the NAc receive glutamate inputs from the PFC and dopamine inputs from the VTA, regulating the release of GABA in the area. The release of dopamine in the PFC and NAc occurs indirectly via CB1R-dependent inhibitions of glutamate and GABA released onto the dopaminergic neurons in the VTA [25].

The neurotransmitters in the extracellular fluids in various brain regions could be sampled using microdialysis and subsequently be analyzed by other instruments, such as liquid chromatography–mass spectrometry (LC–MS), capillary electrophoresis (CE), and microchip electrophoresis (ME). In addition, it is possible to capture large protein molecules depending on the cut-off mass of the probe membranes using microdialysis. More importantly, microdialysis has the advantage of constantly monitoring neurotransmitter concentrations *in vivo* with the possibility to put multiple relatively noninvasive probes, one in each brain region, in a single awake animal [26]. For example, microdialysis has been used to collect the extracellular GABA and glutamate in the PFC of live adult rats after an acute treatment of THC. The results show that a reduction in the extracellular GABA level and an increase in the extracellular glutamate level have been induced from the treatment [27].

The total neurotransmitter levels, including extracellular and intracellular neurotransmitters, as well as their distributions in various tissue sections, could be measured using magnetic resonance spectroscopy imaging (MRSI) [28]. Limited by its sensitivity and spatial resolution, magnetic resonance spectroscopy (MRS) is more widely applied to characterize *in vivo* metabolite concentration in a certain area in disease diagnosis, treatment, and progress monitoring in humans and animal models because of its non-destructive and non-invasive nature rather than visualizing the metabolite distribution in tissues. A limited number of studies investigated the *in vivo* neurotransmitter level changes in response to adolescent cannabis usage in humans by MRS. A reduction of

glutamate in the basal ganglia (BG) and anterior cingulate cortex (ACC) [29] and lower GABA level in ACC [30] are reported in adolescent cannabis users.

Similar to MRSI, mass spectrometry imaging (MSI) offers simultaneous molecule identification, distribution visualization, and quantitation in various tissue regions. A wide range of biomolecules, including metabolites, lipids, peptides, and proteins, could be identified based on their m/z values, MS/MS analysis, and their spatial distribution. Because of its superior sensitivity and spatial resolution, it is used to investigate the distribution and abundance of biomolecules in relatively small, well-defined regions of interest (ROI) to clarify the region-specific functions. Accordingly, in this work, the prelimbic cortex (PrL) and infralimbic cortex (IL), the sub-regions of mPFC, nucleus accumbens core (NAcC) and nucleus accumbens shell (NAcSh), the sub-regions of NAc, dorsal subiculum (DS) and ventral subiculum (VS), the sub-regions of dorsal and ventral hippocampus (dHPC and vHPC) respectively, VTA, and SN are studied. Current evidence indicates functional differences between the PrL and IL, NAcC and NAcSh, and dHPC and vHPC from behavioural, anatomical, and gene expression studies [31-33]. Specifically, the PrL is more involved in cognitive functions, while the IL modulates fear related behaviours [32]; the NAcC is related to select reward, while the NAcSh helps avoid distractions [33]; the dHPC is primarily involved in cognitive functions, while the vHPC regulates stress, emotion, and affect [31]. Furthermore, by using ultra-high spatial resolution imaging, it is possible to visualize the distribution of neurotransmitters at the presynaptic neurons and monitor the intracellular neurotransmitter levels.

In the present study, our lab employed matrix-assisted laser desorption ionization mass spectrometry imaging (MALDI MSI) to study the effects of adolescent THC exposure on neurotransmitter levels, in a region-specific manner, providing neurotransmitter abundance information to the Laviolette lab for a comprehensive study of the impact of chronic THC consumption during adolescence. The strategic selection of ZnO nanoparticles (NP) enables the detection and quantitation of GABA and glutamate, the main inhibitory and excitatory neurotransmitters in the CNS, as well as the mapping of their distributions in various brain sections without an extra derivatization step. The superior spatial resolution of MSI allows us to examine the total neurotransmitter levels in multiple well-defined brain regions at once in both adolescent and adult rat brains subject to chronic adolescent THC exposure. The results will help us understand the short-term and long-lasting effects of chronic THC exposure during adolescence on the neurotransmitter abundances in various ROI including the PrL, IL, NAcC, NAcSh, DS, VS, VTA, and SN in the adolescent and adult brains. These results from the animal models can be compared to the results from human studies using MRS/MRSI directly.

4.2 Experimental Section

4.2.1 Chemicals and Supplies

Δ -9-THC was purchased from Tocris Bioscience (Bristol, United Kingdom). ZnO NP aqueous dispersion (50%, wt) with the particle size less than 100 nm (product no. 721077), α -cyano-4-hydroxycinnamic acid (CHCA), cremophor, and phosphate buffered saline were purchased from Sigma-Aldrich (St. Louis, MO). Sodium pentobarbital (Euthanyl) was purchased from Bimeda-MTC Animal Health Inc. (Quebec, Canada). Ethanol was purchased from Commercial Alcohols (Toronto, Canada). HPLC-grade acetonitrile (ACN) was purchased from VMR (Karlsruhe, Germany). Methanol (MeOH) and trifluoroacetic acid (TFA) were purchased from Fisher Scientific (Waltham, MA). Deionized water (18.2 M Ω ·cm) was purified by the Milli-Q Gradient A10 System (Darmstadt, Germany). Indium-tin oxide (ITO) coated glass slides were purchased from Hudson Surface Technology (Old Tappan, NJ).

4.2.2 Animals and housing

Adolescent Sprague-Dawley male rats were obtained at postnatal day (PND) 28 from Charles River Laboratories (Quebec, Canada). At arrival, rats were pair-housed under controlled conditions (12hour light/dark cycle, constant temperature and humidity) with free access to food and water. The experimental protocols were approved by the Animal Care Committee at Western University, Ontario. All procedures were performed in accordance with the Canadian Council on Animal Care guidelines for the appropriate care and use of rats.

4.2.3 Drug Preparation and Administration

THC was dissolved in ethanol, cremophor, and saline (5/5/90%, vol). Ethanol was then removed by evaporation with nitrogen gas. The Sprague-Dawley rats were injected intraperitoneally (i.p.) twice daily from postnatal day (PND) 35 to 45 with increasing doses of THC (2.5 mg/kg, Days 1–3; 5 mg/kg, Days 4–7; 10 mg/kg, Days 8–11) or vehicle (1/18 cremophor/saline). Increasing doses of THC were administered to counter the development of drug tolerance [34]. This THC dosing regimen was chosen based on previous studies [35] and is known to produce long-term behavioural impairments in rats. The rodent exposure age range (PND 35–45) corresponds to mid-adolescence in the rat [36]. Following THC exposure, rats were left in the home cage until PND 45 (adolescent groups) or PND 75 (adult groups). On day 45/75, the rats were euthanized by injection of sodium pentobarbital (240 mg/kg, i.p.), and then the brains were extracted, fresh frozen, and stored in a –80 °C freezer until analysis. Animal care, drug administration, and brain extraction were carried out by Dr. Marta De Felice in the Laviolette lab, and the brain samples were generously given to the Yeung lab for MALDI MSI analysis.

4.2.4 Sample Preparations for MSI

During tissue sectioning, the ITO-coated glass slides were kept at –20 °C in a CM 1850 Cryostat (Leica Biosystems, Wetzlar, Germany). The brains from the vehicle-treated and THC-treated rats were randomly paired and sectioned to a thickness of 10 µm at different anatomical points (Bregma +3.00, PFC; +2.04, NAc; –6.00, HPC) using a cryostat (CM 1850, Leica Biosystems, Wetzlar, Germany), and the tissue sections from the same anatomical points from the paired vehicle-treated and THC-treated rat brains were mounted

onto the same ITO-coated glass slide with the warmth from the finger. The number of rat brains in each group was as follows: vehicle-treated (n = 5) and THC-treated (n = 5) adolescent rat brains for the effects of chronic adolescent THC exposure on the adolescent rat brain studies; vehicle-treated (n = 4) and THC-treated (n = 4) adult rat brains were used for the effects of chronic adolescent THC exposure on the adult rat brain studies. Prior to matrix deposition, the slides were dried in a vacuum desiccator at room temperature for half an hour. ZnO NP dispersion was prepared in ACN/H₂O (50/50%, vol) at a concentration of 10 mg/mL, ultrasonicated for 10 min, and diluted to a concentration of 1 mg/mL. ZnO NP dispersion was then sprayed onto tissue sections using a TM-Sprayer (HTX Technologies, Chapel Hill, NC) at the following conditions: 1.0 mg/mL of ZnO NP dispersion in ACN/H₂O (50/50%, vol), flow rate of 0.05 mL/min, nozzle temperature at 65 °C, moving nozzle velocity of 1200 mm/min, 32 passes, 3 mm line spacing, and pressure of 10 psi, alternating horizontal and vertical positions between passes. After the spraying cycle was finished, the loop and nozzle were cleaned with a solvent mixture of MeOH/H₂O/TFA (50/50/0.1%, vol) at a flow rate of 0.25 mL/min for 40 min. The default inline filter with a 2 µm pore size (Valco Instruments, Houston, TX) was replaced regularly for maintenance purposes as recommended by the manufacturer.

4.2.5 MALDI MSI Analysis and Data Processing

A Sciex 5800 MALDI TOF/TOF mass spectrometer (Framingham, MA) equipped with a 349 nm Nd: YLF laser with a pulse rate at 400 Hz was used, and images were acquired with Sciex TOF-TOF Series Explorer and TOF-TOF Imaging. For MS mass calibration, 0.75 µL of 5.5 mg/mL CHCA solution containing ACN/H₂O/TFA (50/50/0.1%, vol) was

spotted, and the calibration was based on the following ions with m/z : $[\text{CHCA} - \text{H}_2\text{O} + \text{H}]^+$ at 170.04 Da, $[\text{CHCA} + \text{H}]^+$ at 190.05 Da, $[\text{CHCA} + \text{Na}]^+$ at 212.03 Da, $[\text{CHCA} - \text{H} + 2\text{Na}]^+$ at 234.01 Da, and $[2\text{CHCA} + \text{H}]^+$ at 379.09 Da. Images of tissue sections were acquired at the raster step of 80 μm from 50 to 500 Da in the positive ion mode. The number of shots applied for imaging in each pixel was between 30 and 70. The laser intensity for MSI was optimized based on the number of signals from an m/z range of 50 to 500 Da, peak resolution, and signal-to-noise ratios (S/N).

For neurotransmitter identification, the m/z list was generated from multiple individual spectra across the entire region of scanned images. Structural identification was carried out by performing MS/MS on the tissue samples. MSiReader (1.02), developed by North Carolina State University [37], was used to process and display the ion distributions within tissue sections and to export the data from the ROI for quantitation. Ion images were created within an m/z window of 0.1 Da.

For relative quantitation, mass spectra were generated by exporting the averaged m/z and intensity values from the ROI. The ROI include the PrL and IL from the PFC section, the NAcC and NAcSh from the NAc section, and the DS, VS, VTA, and SN from the HPC section. The peak areas corresponding to $[\text{GABA} + \text{K}]^+$ at m/z 142.03, $[\text{glutamic acid} + \text{K}]^+$ at m/z 186.02, and tentatively identified $[\text{dopamine} + \text{K}]^+$ at m/z 192.04 were integrated with baseline subtraction, and the peak area ratios between the THC-treated and vehicle-treated rat brains were obtained using Microsoft Office Excel 2010 (Microsoft, Redmond, WA).

4.2.6 Statistical Analysis

Four (adult group) or five (adolescent group) biological replicates were measured, and the THC/vehicle ratios from the left and right hemispheres were calculated separately, resulting in either eight (adult group) or ten (adolescent group) ratios. However, some of samples in the adolescent group were unusable, resulting in four ratios obtained from the VTA and SN regions each, and six ratios from the DS and VS regions each. For each neurotransmitter in each ROI, the mean of the peak area ratios as well as their 95% confidence interval (CI) were calculated. Next, we performed the Student's t-test (one sample t-test). In all cases, $p < 0.05$ was considered statistically significant.

4.3 Results and Discussion

4.3.1 Identification and Spatial Distribution of Neurotransmitters in the Rat Brain Sections

The identification of GABA, glutamate, and dopamine was determined by searching the m/z list from MALDI MSI within 50 ppm against the theoretical m/z values of neurotransmitters, based on adducts with K^+ . The peaks were then verified by the isotope peak patterns from carbon and potassium. MS/MS was carried out on the brain tissue sections for structural confirmation, and the neurotransmitters were manually identified by comparing MS/MS fragmentation spectra to the standard MS/MS spectra in the METLIN Metabolomics Database as well as the prediction of cleavage sites. The MS/MS spectra of identified GABA and glutamate were shown in the previous chapter (Figure 3.3). The presence of GABA and glutamate was also confirmed by the metabolite list created from an LC–MS analysis of brain samples in Chapter 2. The ion images of GABA and glutamate in Figures 4.2 and 4.3 show the structure of adolescent and adult rat brains at various anatomical points from either the vehicle or the THC treatment during adolescence. GABA and glutamate show similar spatial distributions in the adolescent and adult rat brains. In addition, the THC treatment during adolescence does not alter the spatial distributions of GABA and glutamate in those brain sections.

Similar to the ion images acquired in Chapter 3, the ion image of tentatively assigned [dopamine + K]⁺ at m/z 192.04 acquired in this chapter also show that the molecule is specifically localized in the white matter region of rat brain, conflicting with the fact that the grey matter region contains the cell bodies of neurons that secrete neurotransmitters

[38] as well as the distribution of dopamine in other imaging work [39-41]. Although the identification of the signal at m/z 192.04 could not be performed due to the limited MS/MS information in the METLIN Metabolomics Database, we still include the quantitation results from it in the later sections for the completeness of this study.

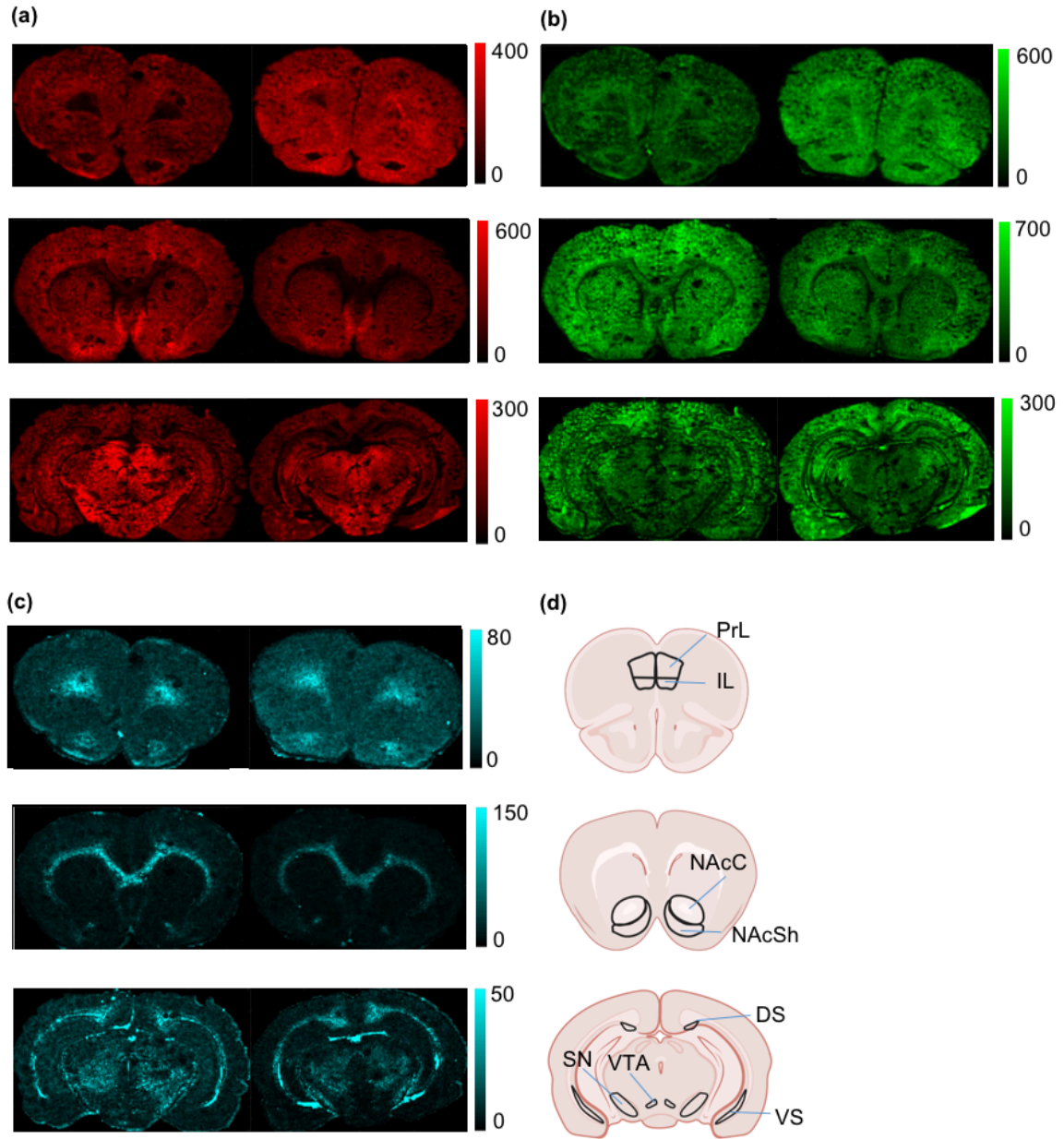


Figure 4.2. Ion images of **vehicle-** (left) or **THC-treated** (right) tissue sections from the adolescent rat brains acquired with ZnO NP-assisted laser desorption ionization mass spectrometry imaging (LDI MSI), **(a)** [GABA + K]⁺ at m/z 142.03, **(b)** [glutamate + K]⁺ at m/z 186.02, and **(c)** the signal at m/z 192.04 and **(d)** schematic diagrams showing the ROI (PrL, IL, NAcC, NAcSh, DS, VS, VTA, and SN) are presented (top to bottom: Bregma +3.00 mm, PFC; +2.04 mm, NAc; -6.00 mm, HPC; Paxinos and Watson Atlas; raster size of 80 μ m).

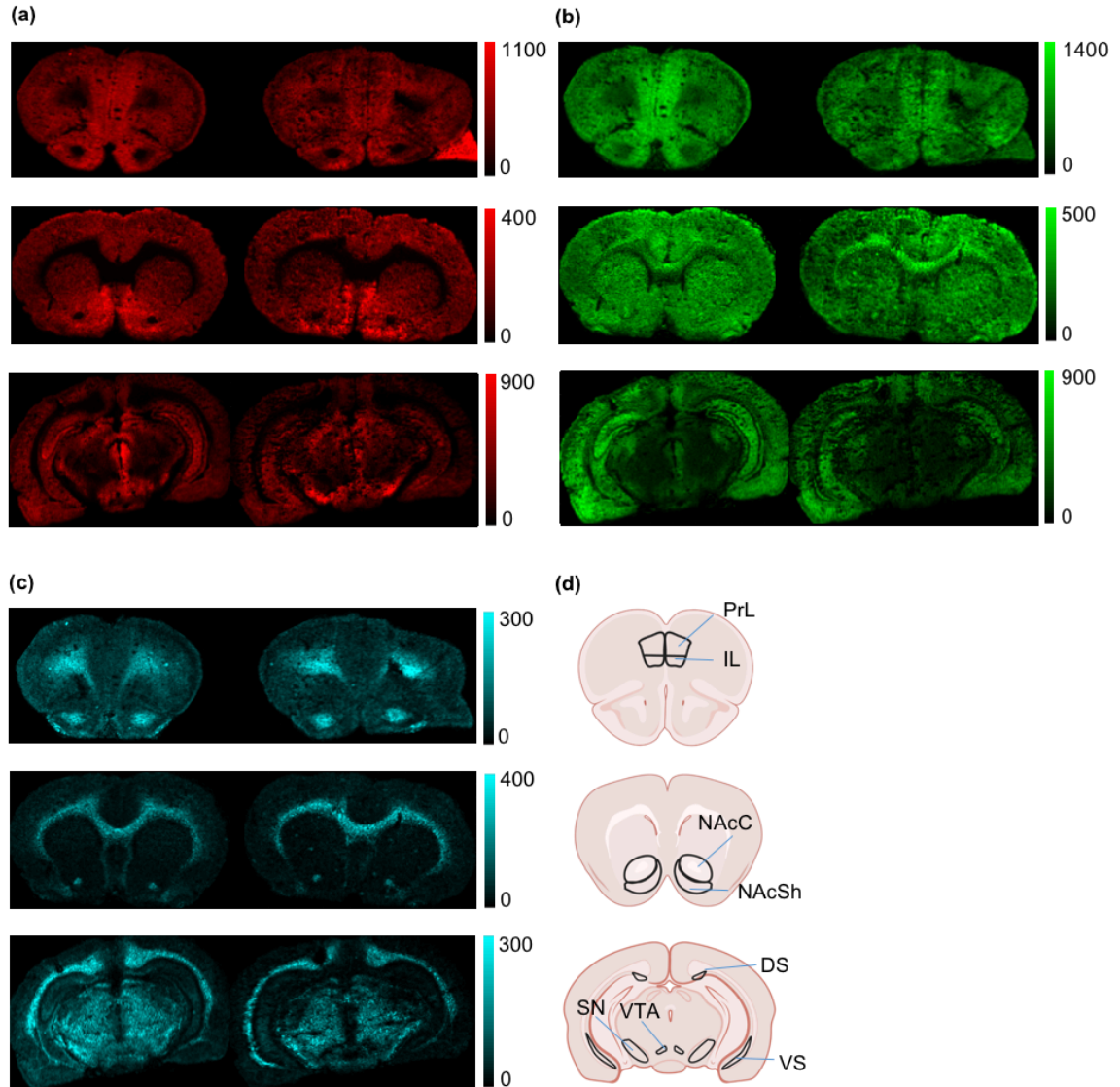


Figure 4.3. Ion images of **vehicle-treated (left)** or **THC-treated (right)** tissue sections from the adult rat brains acquired with ZnO NP-assisted LDI MSI. **(a)** $[\text{GABA} + \text{K}]^+$ at m/z 142.03, **(b)** $[\text{glutamate} + \text{K}]^+$ at m/z 186.02, and **(c)** the signal at m/z 192.04 and **(d)** schematic diagrams showing the ROI (PrL, IL, NAcC, NAcSh, DS, VS, VTA, and SN) are presented (top to bottom: Bregma +3.00 mm, PFC; +2.04 mm, NAc; -6.00 mm, HPC; Paxinos and Watson Atlas; raster size of 80 μm).

4.3.2 Relative Quantitation of Neurotransmitters between the THC-treated and Vehicle-treated Rat Brains

The aim of this study was to observe the changes of neurotransmitters in various ROI of the rat brains after the chronic THC treatment compared to the vehicle treatment during adolescence. Since the fluctuations between measurements can disrupt the analysis of biological samples, we put one sample of each group (vehicle-treated or THC-treated) on one slide and calculated the signal peak area ratio to detect the differences between the THC-treated and vehicle-treated rats. Biological replicates were continuously measured, and a number of peak area ratios from the biological replicates were obtained for every neurotransmitter in each ROI.

The individual peak area ratios of GABA at m/z 142.03, glutamate at m/z 186.02, and the signal at m/z 192.04 in various regions between the THC-treated and vehicle-treated brains from the adolescent and adult rats are shown in Figures 4.4 and 4.5. We also demonstrate the geometric means of the signal peak area ratios of $[\text{GABA} + \text{K}]^+$ at m/z 142.03, $[\text{Glutamate} + \text{K}]^+$ at m/z 186.02, and the signal at m/z 192.04, 95% CIs, and p-values from the Student t-test between the THC-treated and vehicle-treated brains from the adolescent and adult rats in each brain region, including the PrL, IL, NAcC, NAcSh, DS, VS, VTA, and SN, in Tables 4.1 and 4.2. The relative quantitation results will be discussed in detail in later sections.

4.3.3 Effects of Chronic Adolescent THC Exposure on the Neurotransmitter Abundance in the Adolescent Rat Brains

We first examined the short-term effects of chronic adolescent THC exposure on the neurotransmitters in the adolescent rat brains by looking at the peak area ratios of neurotransmitters between the THC-treated and vehicle-treated adolescent rat brains that were extracted two hours after the last injection of THC during adolescence, at PND 45, as shown in Figure 4.4. Compared to the GABA signals obtained from the vehicle-treated rats, significant differences ($p < 0.05$) were found in the NAcC, DS, VS, and SN (NAcC: $p = 0.0092$; DS: $p = 0.0019$; VS: $p = 0.00017$; SN: $p = 0.00026$) in the THC-treated adolescent rats. A decrease of around 20% in the NAcC and more than 30% reduction in the DS, VS, and SN were observed. No significant differences were detected in the PrL, IL, NAcSh, and VTA (PrL: $p = 0.061$; IL: $p = 0.15$; NAcSh: $p = 0.077$; VTA: $p = 0.063$).

In terms of glutamate, significant differences ($p < 0.05$) were found in the PrL and DS (PrL: $p = 0.020$; DS: $p = 0.0038$). Glutamate signal was found to increase by at least 1.4 fold in the PrL and to reduce by more than 30% in the DS of the THC-treated adolescent rats. However, no significant differences were detected in the IL, NAcC, NAcSh, VS, VTA, and SN (IL: $p = 0.061$; NAcC: $p = 0.22$; NAcSh: $p = 0.61$; VS: $p = 0.77$; VTA: $p = 0.24$; SN: $p = 0.43$).

Comparing GABA and glutamate signals, chronic adolescent THC exposure led to downregulated GABA and glutamate in the DS in the adolescent rat brains, but selective

decreases of GABA not glutamate in the NAcC, VS, and SN and a selective increase of glutamate not GABA in the PrL.

The signal at m/z 192.04 showed significant changes ($p < 0.05$) between the THC-treated and vehicle-treated adolescent rats in the NAcC, NAcSh, DS, and VTA (NAcC: $p = 0.015$; NAcSh: $p = 0.047$; DS: $p = 6.9E-5$; VTA: $p = 0.00014$). At least 20% decrease in the NAcC and NAcSh and more than 50% reduction in the DS and VTA were observed. No significant differences were detected in the PrL, IL, VS, and SN (PrL: $p = 0.13$; IL: $p = 0.13$; VS: $p = 0.41$; SN: $p = 0.10$).

When looking at the effects of chronic adolescent THC exposure on the neurotransmitter levels in the sub-regions of mPFC, NAc, and HPC in the adolescent rat brains, GABA was found to selectively decrease in the NAcC but not NAcSh, glutamate was found to selectively increase in the PrL but not IL, and glutamate and the signal at m/z 192.04 were found to selectively reduce in the DS but not VS. Downregulation of GABA in both DS and VS and the signal at m/z 192.04 in both NAcC and NAcSh were observed.

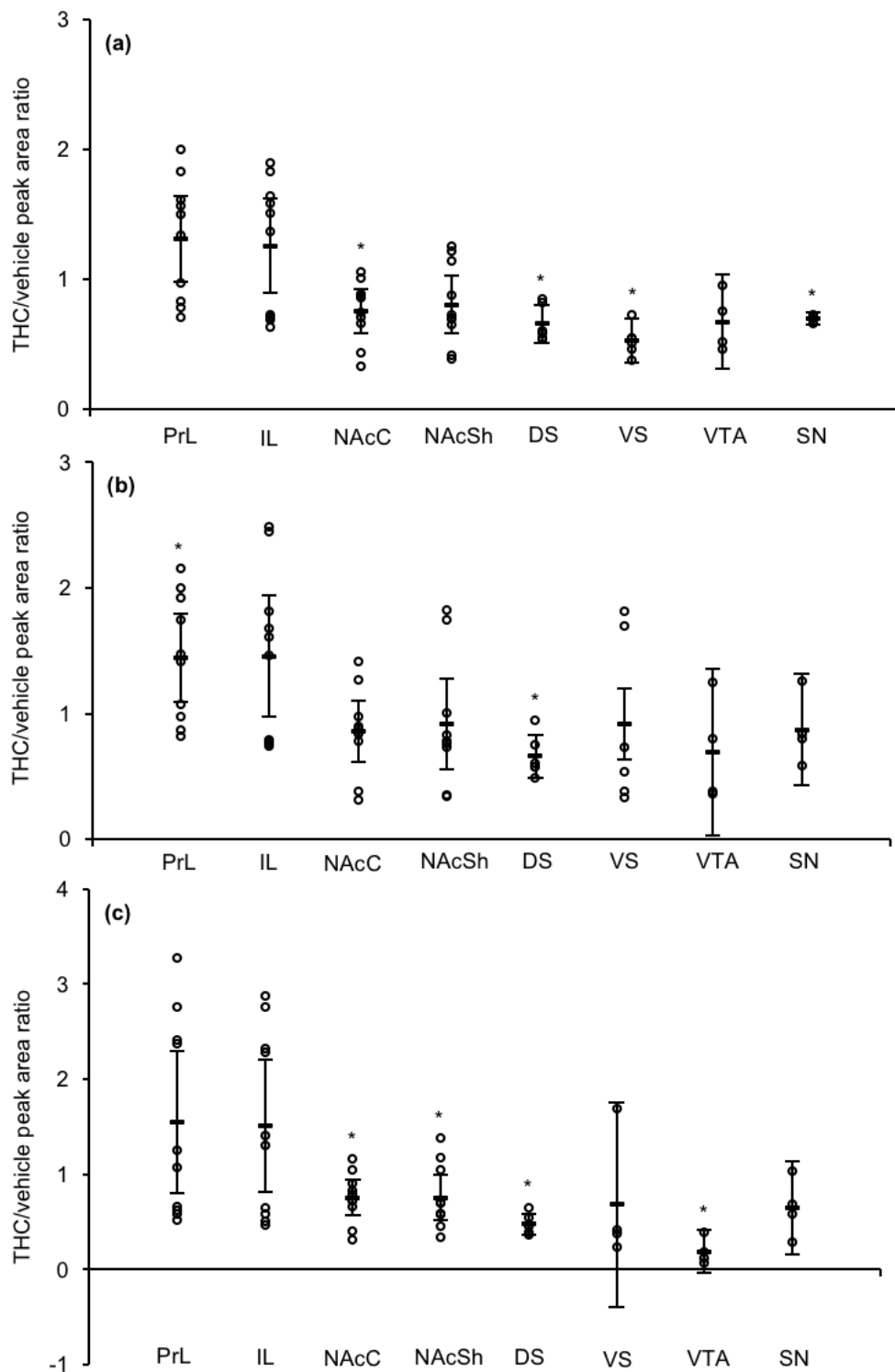


Figure 4.4. The peak area ratios of (a) $[GABA + K]^+$ at m/z 142.03, (b) $[glutamate + K]^+$ at m/z 186.02, and (c) the signal at m/z 192.04 between the THC-treated and vehicle-treated adolescent rat brains in various regions ($n = 10$, PrL, IL, NAcC, and NAcSh; $n = 6$, DS and VS; $n = 4$, VTA and SN). The arithmetic mean and 95% CI of THC/vehicle peak area ratios are displayed as a bar. Asterisks indicate the brain regions that featured significant differences using the peak area ratios between the THC-treated and vehicle-treated adolescent rat brains in the Student t-test ($*p < 0.05$).

Table 4.1. The Averaged Peak Area Ratios (Fold Changes) of [GABA + K]⁺ at *m/z* 142.03, [Glutamate + K]⁺ at *m/z* 186.02, and the Signal at *m/z* 192.04, Their 95% CIs, and P-values from the Student T-test between the THC-treated and Vehicle-treated Adolescent Rat Brains in Various ROI (n = 10, PrL, IL, NAcC, and NAcSh; n = 6, DS and VS; n = 4, VTA and SN) Are Presented. The Fold Change ± 95% CI Is Bolded When It Is Significantly Different than 1. P-value Is Bolded When It Is Less Than 0.05.

brain ROI	GABA		glutamate		signal at <i>m/z</i> 192.04	
	fold change	p-value	fold change	p-value	fold change	p-value
prelimbic cortex, PrL	1.31 ± 0.33	0.061	1.44 ± 0.36	0.020	1.55 ± 0.75	0.13
infralimbic cortex, IL	1.26 ± 0.37	0.15	1.46 ± 0.48	0.061	1.51 ± 0.69	0.13
nucleus accumbens core, NAcC	0.76 ± 0.17	0.0092	0.86 ± 0.24	0.22	0.75 ± 0.19	0.015
nucleus accumbens shell, NAcSh	0.80 ± 0.22	0.077	0.92 ± 0.36	0.61	0.75 ± 0.24	0.047
dorsal subiculum, DS	0.66 ± 0.15	0.0019	0.66 ± 0.17	0.0038	0.48 ± 0.11	6.9E-5
ventral subiculum, VS	0.53 ± 0.12	0.00017	0.92 ± 0.70	0.77	0.68 ± 1.08	0.41
ventral tegmental area, VTA	0.67 ± 0.36	0.063	0.70 ± 0.66	0.24	0.19 ± 0.22	0.0014
substantia nigra, SN	0.70 ± 0.05	0.00026	0.87 ± 0.28	0.45	0.65 ± 0.49	0.10

4.3.4 Effects of Chronic Adolescent THC Exposure on the Neurotransmitter Abundance in the Adult Rat Brains

We next examined the long-term effects of adolescent chronic THC exposure on the neurotransmitters in the adult rat brains. Specifically, after 30 days of the chronic administrations of THC during adolescence, at PND 75, the brains from the adult rats were extracted and imaged, and the peak area ratios of neurotransmitters between the THC-treated and vehicle-treated adult rats were calculated, as shown in Figure 4.5. Compared to the GABA signals obtained from the vehicle-treated rats, significant differences ($p < 0.05$) were found in the NAcC, NAcSh, DS, and VTA (NAcC: $p = 0.0014$; NAcSh: $p = 0.011$; DS: $p = 0.0019$; VTA: $p = 0.022$) in the THC-treated adult rats. A decrease of more than 40% in the DS and at least 20% reduction were observed in the NAcC, NAcSh, and VTA. No significant differences were detected in the PrL, IL, VS and SN (PrL: $p = 0.94$; IL: $p = 0.78$; VS: $p = 0.076$; SN: $p = 0.091$).

In terms of glutamate, significant differences ($p < 0.05$) were found in the NAcC and VTA (NAcC: $p = 0.014$; VTA: $p = 0.016$). Glutamate signal was found to decrease by 32% in the VTA and by around 20% in the NAcC in the THC-treated adult rats. However, no significant differences were detected in the PrL, IL, NAcSh, DS, VS, and SN (PrL: $p = 0.50$; IL: $p = 0.38$; NAcSh: $p = 0.059$; DS: $p = 0.10$; VS: $p = 0.28$; SN: $p = 0.65$).

Comparing GABA and glutamate signals, chronic adolescent THC exposure led to downregulated GABA and glutamate in the NAcC and VTA, but selective decreases of GABA not glutamate in the NAcSh and DS in the adult rat brains.

The signal at m/z 192.04 showed significant differences ($p < 0.05$) between the THC-treated and vehicle-treated adult rats in the DS and VS (DS: $p = 0.0019$; VS: $p = 0.017$), with around 40% decrease in those areas. No significant differences were detected in the PrL, IL, NAcC, NAcSh, VTA, and SN (PrL: $p = 0.53$; IL: $p = 0.86$; NAcC: $p = 0.92$; NAcSh: $p = 0.40$; VTA: $p = 0.061$; SN: $p = 0.22$).

When comparing the effects of chronic adolescent THC exposure on the neurotransmitter levels in the sub-regions of mPFC, NAc, and HPC in the adult rat brains, a selective decrease of GABA in the DS but not VS and a selective reduction of glutamate in the NAcC but not NAcSh were found. Downregulation of GABA in both NAcC and NAcSh and the signal at m/z 192.04 in both DS and VS were observed.

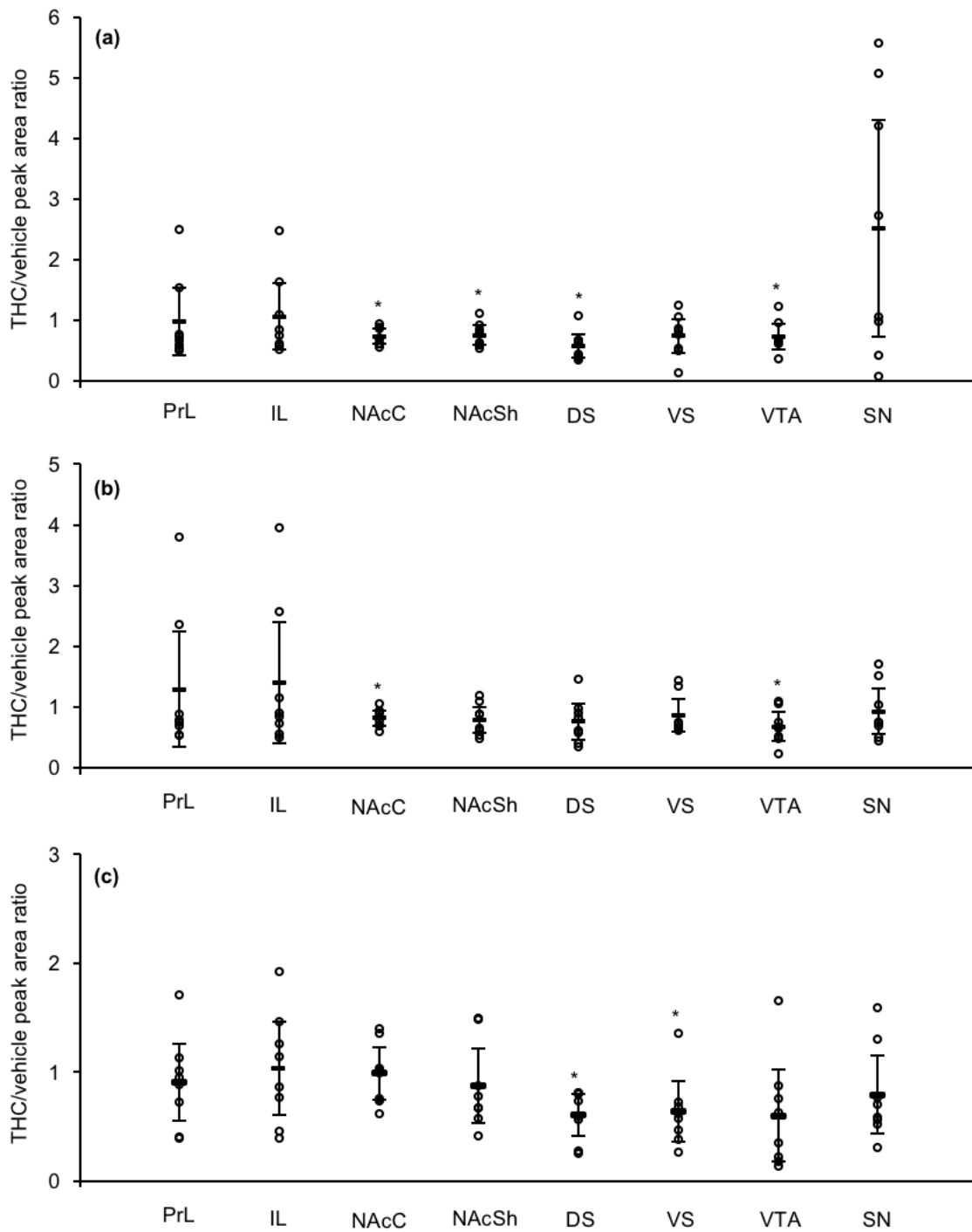


Figure 4.5. The peak area ratios of (a) $[GABA + K]^+$ at m/z 142.03, (b) $[glutamate + K]^+$ at m/z 186.02, and (c) the signal at m/z 192.04 between the THC-treated and vehicle-treated adult rat brains in various regions ($n = 8$). The arithmetic mean and 95% CI of THC/vehicle peak area ratios are displayed as a bar. Asterisks indicate the brain regions that featured significant differences using the peak area ratios between the THC-treated and vehicle-treated adult rat brains in the Student t-test (* $p < 0.05$).

Table 4.2. The Averaged Peak Area Ratios (Fold Changes) of [GABA + K]⁺ at *m/z* 142.03, [Glutamate + K]⁺ at *m/z* 186.02, and the Signal at *m/z* 192.04, Their 95% CIs, and P-values from the Student T-test between the THC-treated and Vehicle-treated Adult Rat Brains in Various ROI (n = 8) Are Presented. The Fold Change ± 95% CI Is Bolded When It Is Significantly Different than 1. P-value Is Bolded When It Is Less Than 0.05.

brain ROI	GABA		glutamate		signal at <i>m/z</i> 192.04	
	fold change	p-value	fold change	p-value	fold change	p-value
prelimbic cortex, PrL	0.98 ± 0.58	0.94	1.29 ± 0.98	0.50	0.90 ± 0.35	0.53
infralimbic cortex, IL	1.07 ± 0.57	0.78	1.40 ± 1.02	0.38	1.03 ± 0.43	0.86
nucleus accumbens core, NAcC	0.74 ± 0.12	0.0014	0.82 ± 0.13	0.014	0.99 ± 0.24	0.92
nucleus accumbens shell, NAcSh	0.76 ± 0.17	0.011	0.79 ± 0.22	0.059	0.87 ± 0.34	0.20
dorsal subiculum, DS	0.58 ± 0.20	0.0019	0.76 ± 0.30	0.10	0.60 ± 0.19	0.0019
ventral subiculum, VS	0.75 ± 0.29	0.076	0.86 ± 0.28	0.28	0.63 ± 0.28	0.017
ventral tegmental area, VTA	0.73 ± 0.22	0.022	0.68 ± 0.24	0.016	0.60 ± 0.42	0.061
substantia nigra, SN	2.52 ± 1.83	0.091	0.92 ± 0.39	0.65	0.79 ± 0.36	0.22

4.3.5 Comparison of Effects of Chronic Adolescent THC Exposure in the Adolescent and Adult Rat Brains

By comparing the short-term and long-term effects of chronic adolescent THC exposure, we found GABA, glutamate, and the signal at m/z 192.04 were affected differently in the two periods in various ROI, as shown in Figure 4.6. The effects of chronic adolescent THC on GABA level persisted in the NAcC and DS, where GABA showed decreases in both adolescent and adult THC rat brains. Similarly, the reduction of the signal at m/z 192.04 persisted in the DS. The increased level of glutamate in the PrL in the adolescent rat brains was rebalanced in the adult rat brains, where no significant difference was observed between the THC and vehicle groups. Chronic adolescent THC exposure was shown to affect GABA in the VS and SN, glutamate in the PrL and DS, and the signal at m/z 192.04 in the NAcC, NAcSh, and VTA in the short term, where all of them decreased in the adolescent THC rat brains. On the contrary, long-lasting effects of chronic adolescent THC were developed on GABA in the adult rat brains in the NAcSh and VTA, glutamate in the NAcC and VTA, and the signal at m/z 192.04 in the VS, where decreased levels of all three neurotransmitters were observed in the adult THC brains.

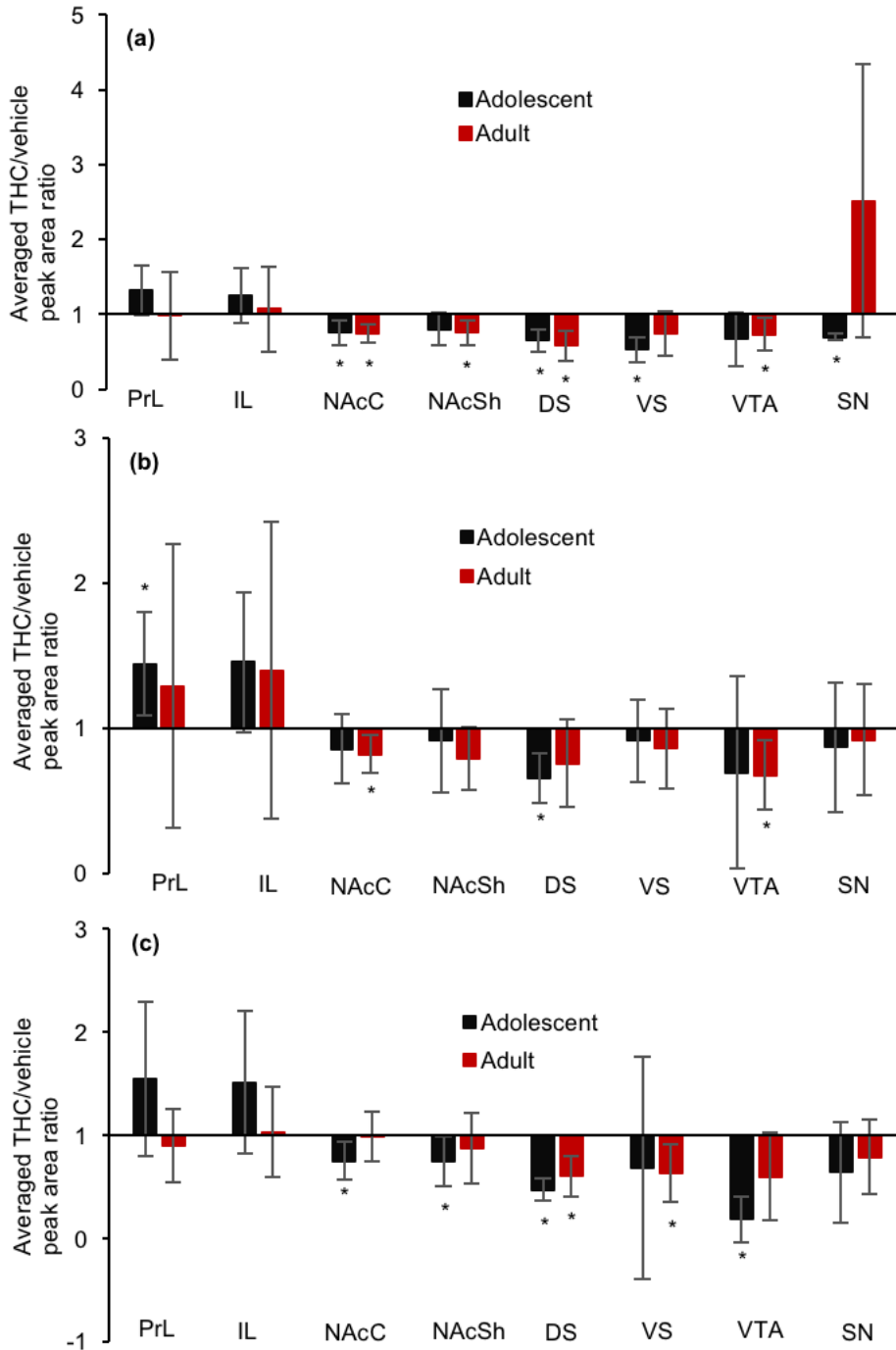


Figure 4.6. Comparison of the averaged signal ratios of (a) [GABA + K]⁺ at *m/z* 142.03, (b) [glutamate + K]⁺ at *m/z* 186.02, and (c) the signal at *m/z* 192.04 between the THC-treated and vehicle-treated brains in various brain ROI in the adolescent and adult rats (n = 10, PrL, IL, NAcC, and NAcSh; n = 6, DS and VS; n = 4, VTA and SN; adolescent rat brains; n = 8, adult rat brains). The averaged arithmetic mean of THC/vehicle peak area ratios is displayed as a bar. Each error bar represents a 95% CI of THC/vehicle peak area ratios. Asterisks indicate the brain regions that featured significant difference using the peak area ratios between the THC-treated and vehicle-treated rat brains in the Student t-test (*p < 0.05).

4.3.6 Comparison with Literature

4.3.6.1 Clinical Studies

Reductions in the glutamate [29] and GABA [30] levels in the ACC have been reported after chronic cannabis use in adolescent smokers. On the contrary, we have detected an increase of glutamate in the PrL, which is corresponding to a sub-region of the ACC in human brains, in the adolescent rat brains following chronic THC exposure during adolescence.

4.3.6.2 Preclinical Studies Using Animal Models

Preclinical studies have found that chronic adolescent THC exposure reduces the expression of GAD-67 and enhances the firing frequency of excitatory pyramidal cells in the mPFC of the adult rats as previously reported by Renard and colleagues from the Laviolette lab [6], indicating less GABA is synthesized and more glutamate is released in the mPFC, while no significant differences in the total GABA and glutamate levels were observed in the subdivisions of mPFC, the PrL and IL, between the THC-treated and vehicle-treated adult rat brains. The expression of several glutamate receptor subunits, including the subunit of NMDA subtype of glutamate receptors, GluN2B, and the subunits of α -amino-3-hydroxy-5-methyl-4-isoxazolepropionic acid (AMPA) subtype of glutamate receptors, GluA1 and GluA2, has been reported to significantly increase in hippocampal post-synaptic sites of the THC-treated adult rats, and no significant changes on NMDA and AMPA receptor subunits have been found in the PFC, as shown by Zamberletti et al. [42]. We did not observe any significant differences in the total glutamate levels in the PrL, IL,

DS, and VS between the THC-treated and vehicle-treated adult rats following adolescent exposure.

The total neurotransmitter levels could be affected by several processes including synthesis, release, binding to receptors, and degradation. For example, after the release of glutamate from the glutamatergic neurons, glutamate could bind to the receptors on the postsynaptic neurons or be rapidly transported from the synaptic cleft into astroglial cells where it is converted into glutamine. The discrepancies between the literature and this work could result from this work's focus on total neurotransmitter levels, while the reports above focused on neurotransmitter synthesis, release, and binding to receptors. The differences in the studied regions also lead to the discrepancies. In this work, we examined the total neurotransmitter levels in the sub-regions of HPC, the DS and VS, while it was not specified whether the sub-regions of HPC or HPC was studied in the work conducted by Zamberletti et al. [42]. Altogether, it is expected that we are seeing different results. The results on the neuron activity and protein expression levels from Laviolette's lab will help further explain the effects of chronic adolescent THC exposure on total neurotransmitter abundance.

Relevant studies have shown that the CB1R density is reduced in the PFC, NAc, HPC, and VTA of the adolescent rats but not the adult rats subjected to chronic adolescent THC exposure [43]. Besides, the coupling of CB1Rs to G-protein is reduced in the HPC and SN of the adolescent rats not the adult rats, making CB1Rs less sensitive to THC [43]. The changes in the expression of CB1Rs and coupling of CB1Rs to G-protein in the adolescent

brains but not in the adult brains following chronic adolescent THC exposure could partially result in the neurotransmitter abundance changes in some ROI only in the adolescent brains. For example, we observed reductions of GABA in the VS and SN, an increase of glutamate in the PrL, and a decrease of glutamate in the DS in the adolescent brains but not in the adult brains.

4.4 Conclusion

MALDI MSI allows direct visualizations of the distributions and abundances of GABA and glutamate in the brain. The relative quantitation of GABA and glutamate between the drug-treated and vehicle-treated animals in various brain sub-regions enables us to examine those brain regions separately to investigate the region-specific functions. The sub-regions of NAc, the NAcC and NAcSh, and the sub-regions of HPC, the DS and VS, has been found to be affected differently from chronic adolescent THC exposure, indicating the functional differences between the NAcC and NAcSh as well as the DS and VS. Chronic THC exposure during adolescence has also been shown to alter adolescent brains in the short term and adult brains in the long term differently in the examined brain regions. In addition, those results provide us with a direct way to compare THC studies from animal models with adolescent cannabis human studies using MRS.

4.5 Reference

- (1) Arain, M.; Haque, M.; Johal, L.; Mathur, P.; Nel, W.; Rais, A.; Sandhu, R.; Sharma, S. *Neuropsychiatric Disease and Treatment* **2013**, *9*, 449-460.
- (2) Gobbi, G.; Atkin, T.; Zytynski, T.; Wang, S. A.; Askari, S.; Boruff, J.; Ware, M.; Marmorstein, N.; Cipriani, A.; Dendukuri, N.; Mayo, N. *Jama Psychiatry* **2019**, *76*, 426-434.
- (3) Arseneault, L.; Cannon, M.; Poulton, R.; Murray, R.; Caspi, A.; Moffitt, T. E. *British Medical Journal* **2002**, *325*, 1212-1213.
- (4) Chye, Y.; Christensen, E.; Yucel, M. *Journal of Dual Diagnosis* **2020**, *16*, 83-105.
- (5) Opel, N.; Goltermann, J.; Hermesdorf, M.; Berger, K.; Baune, B. T.; Dannlowski, U. *Biological Psychiatry* **2020**, *88*, 678-686.
- (6) Renard, J.; Szkudlarek, H. J.; Kramar, C. P.; Jobson, C. E. L.; Moura, K.; Rushlow, W. J.; Laviolette, S. R. *Scientific Reports* **2017**, *7*.
- (7) Renard, J.; Rosen, L. G.; Loureiro, M.; De Oliveira, C.; Schmid, S.; Rushlow, W. J.; Laviolette, S. R. *Cerebral Cortex* **2017**, *27*, 1297-1310.
- (8) Banich, M. T.; Floresco, S. *Cognitive Affective & Behavioral Neuroscience* **2019**, *19*, 409-414.
- (9) Gogtay, N.; Giedd, J. N.; Lusk, L.; Hayashi, K. M.; Greenstein, D.; Vaituzis, A. C.; Nugent, T. F.; Herman, D. H.; Clasen, L. S.; Toga, A. W.; Rapoport, J. L.; Thompson, P. M. *Proceedings of the National Academy of Sciences of the United States of America* **2004**, *101*, 8174-8179.
- (10) Tye, K. M. *Neuron* **2012**, *76*, 671-673.
- (11) Zimmermann, K. S.; Richardson, R.; Baker, K. D. *Brain Sciences* **2019**, *9*.

- (12) Laviolette, S. R. *Psychological medicine* **2019**, 1-8.
- (13) Olive, M. F.; Tomek, S. E. *Animal Models for Examining Social Influences on Drug Addiction*; Academic press, 2018.
- (14) Herkenham, M.; Lynn, A. B.; Johnson, M. R.; Melvin, L. S.; Decosta, B. R.; Rice, K. C. *Journal of Neuroscience* **1991**, *11*, 563-583.
- (15) Mechoulam, R.; Parker, L. A. *Annual Review of Psychology, Vol 64* **2013**, *64*, 21-47.
- (16) Cass, D. K.; Flores-Barrera, E.; Thomases, D. R.; Vital, W. F.; Caballero, A.; Tseng, K. Y. *Molecular Psychiatry* **2014**, *19*, 536-543.
- (17) Hoffman, A. F.; Lupica, C. R. *Journal of Neurophysiology* **2001**, *85*, 72-83.
- (18) Katona, I.; Sperlagh, B.; Sik, A.; Kafalvi, A.; Vizi, E. S.; Mackie, K.; Freund, T. F. *Journal of Neuroscience* **1999**, *19*, 4544-4558.
- (19) Riegel, A. C.; Lupica, C. R. *Journal of Neuroscience* **2004**, *24*, 11070-11078.
- (20) Chan, P. K. Y.; Chan, S. C. Y.; Yung, W. H. *Neuroreport* **1998**, *9*, 671-675.
- (21) Auclair, N.; Otani, S.; Soubrie, P.; Crepel, F. *Journal of Neurophysiology* **2000**, *83*, 3287-3293.
- (22) Robbe, D.; Alonso, G.; Duchamp, F.; Bockaert, J.; Manzoni, O. J. *Journal of Neuroscience* **2001**, *21*, 109-116.
- (23) Misner, D. L.; Sullivan, J. M. *Journal of Neuroscience* **1999**, *19*, 6795-6805.
- (24) Han, J.; Kesner, P.; Metna-Laurent, M.; Duan, T. T.; Xu, L.; Georges, F.; Koehl, M.; Abrous, D. N.; Mendizabal-Zubiaga, J.; Grandes, P.; Liu, Q. S.; Bai, G.; Wang, W.; Xiong, L. Z.; Ren, W.; Marsicano, G.; Zhang, X. *Cell* **2012**, *148*, 1039-1050.
- (25) Cohen, K.; Weizman, A.; Weinstein, A. *European Journal of Neuroscience* **2019**, *50*, 2322-2345.

- (26) Hammarlund-Udenaes, M. *Aaps Journal* **2017**, *19*, 1294-1303.
- (27) Pistis, M.; Ferraro, L.; Pira, L.; Flore, G.; Tanganelli, S.; Gessa, G. L.; Devoto, P. *Brain Research* **2002**, *948*, 155-158.
- (28) Godlewska, B. P.; Clare, S.; Cowen, P. J.; Emir, U. E. *Frontiers in Psychiatry* **2017**, *8*.
- (29) Prescott, A. P.; Locatelli, A. E.; Renshaw, P. F.; Yurgelun-Todd, D. A. *Neuroimage* **2011**, *57*, 69-75.
- (30) Prescott, A. P.; Renshaw, P. F.; Yurgelun-Todd, D. A. *Drug and Alcohol Dependence* **2013**, *129*, 232-239.
- (31) Fanselow, M. S.; Dong, H. W. *Neuron* **2010**, *65*, 7-19.
- (32) Franklin, K. B. J.; Chudasama, Y. *Mouse Nervous System* **2012**, 727-735.
- (33) Pavuluri, M.; Volpe, K.; Yuen, A. *Aims Neuroscience* **2017**, *4*, 52-70.
- (34) Gonzalez, S.; Cebeira, M.; Fernandez-Ruiz, J. *Pharmacology Biochemistry and Behavior* **2005**, *81*, 300-318.
- (35) Rubino, T.; Realini, N.; Braidà, D.; Guidi, S.; Capurro, V.; Vigano, D.; Guidali, C.; Pinter, M.; Sala, M.; Bartesaghi, R.; Parolaro, D. *Hippocampus* **2009**, *19*, 763-772.
- (36) Spear, L. P. *Neuroscience and Biobehavioral Reviews* **2000**, *24*, 417-463.
- (37) Robichaud, G.; Garrard, K. P.; Barry, J. A.; Muddiman, D. C. *Journal of the American Society for Mass Spectrometry* **2013**, *24*, 718-721.
- (38) Butt, A. M.; Fern, R. F.; Matute, C. *Glia* **2014**, *62*, 1762-1779.
- (39) Shariatgorji, M.; Nilsson, A.; Goodwin, R. J. A.; Kallback, P.; Schintu, N.; Zhang, X. Q.; Crossman, A. R.; Bezard, E.; Svenningsson, P.; Andren, P. E. *Neuron* **2014**, *84*, 697-707.

- (40) Shariatgorji, M.; Nilsson, A.; Fridjonsdottir, E.; Vallianatou, T.; Kallback, P.; Katan, L.; Savmarker, J.; Mantas, I.; Zhang, X. Q.; Bezard, E.; Svenningsson, P.; Odell, L. R.; Andren, P. E. *Nature Methods* **2019**, *16*, 1021-1028.
- (41) Shariatgorji, R.; Nilsson, A.; Strittmatter, N.; Vallianatou, T.; Zhang, X.; Svenningsson, P.; Goodwin, R. J. A.; Andren, P. E. *Journal of the American Society for Mass Spectrometry* **2020**, *31*, 2553-2557.
- (42) Zamberletti, E.; Gabaglio, M.; Grilli, M.; Prini, P.; Catanese, A.; Pittaluga, A.; Marchi, M.; Rubino, T.; Parolaro, D. *Pharmacological Research* **2016**, *111*, 459-470.
- (43) Rubino, T.; Viganò, D.; Realini, N.; Guidali, C.; Braida, D.; Capurro, V.; Castiglioni, C.; Cherubino, F.; Romualdi, P.; Candeletti, S.; Sala, M.; Parolaro, D. *Neuropsychopharmacology* **2008**, *33*, 2760-2771.

Chapter 5: Conclusions & Future Work

5.1 Conclusions and Future Work

Mass spectrometry imaging (MSI) is an incredibly powerful technique for the detection and visualization of spatial distributions and abundances of small molecules within tissue sections. Unlike conventional molecular imaging techniques such as positron emission tomography (PET) and fluorescence imaging, where radioactive or fluorescent labelling is required to target specific compounds, MSI offers a means to perform the analysis of multiple analytes without labelling. Through the introduction of the matrix-assisted laser desorption ionization (MALDI) technique, MALDI MSI offers selective detection and imaging of small molecules in complex biological samples by applying various matrices. The superior spatial resolution from the use of pulsed laser beams is beneficial in visualizing molecular distributions and abundances in well-defined regions, which presents a great opportunity to understand biological systems.

The development of inorganic matrices in MALDI MSI provides opportunities for the detection and imaging of small molecules with higher sensitivity compared to traditional organic matrices. Commercially available ZnO nanoparticle (NP) dispersion has been found to be superior for assisting the LDI MS imaging of low molecular weight molecules (LMWM) in rodent brain tissues when compared to TiO₂ NP, one of the most commonly used inorganic matrices. Compared to TiO₂ NP, the low aggregation degree of ZnO NP and easy cleaning of the NP with dilute acid make it compatible with automated sprayers, which allows the generation of relatively high spatial resolution images. The low level of matrix background signals in the low mass range enables the excellent detection of LMWM, like TiO₂ NP.

However, the aggregation of metal oxide NP has been reported to cause signal decreases in MALDI MS of small molecules [1]. The surface modifications of NP have been found to stabilize the NP, promote the interaction between the NP and analytes, and enhance the ionization of molecules [2-4]. For instance, citric acid capped iron oxide NP have been shown to improve the ionization of polar or nonpolar polymers [3]. Dopamine-modified TiO₂ sub-micron particles have been found to enhance the detection sensitivity of small metabolites in brain tissues [2]. The surface of ZnO NP has been modified with monomeric ligands like citrate and polymer ligands such as poly(acrylic acid), poly-L-lysine hydrochloride, poly(vinylpyrrolidone), polymethacrylic acid, and polyethylene glycol [5-8], while its application in MALDI MSI is limited. Polymer ligands stabilize the NP through steric and electrostatic forces, while monomeric ligands stabilize the NP only through electrostatic repulsive forces. Therefore, polymer-coated NP produces more stable suspensions compared to monomeric ligand-coated NP [5]. Besides, the cleavage of ligands on the nanoparticle surface could occur during the ionization process, producing ligand-related peaks in the mass spectra [2]. The modifications of NP with polymers thus have the advantage over monomeric ligands because their molecular weight is beyond the mass range of interest (below 500 Da). Future work would thus focus more on applying the polymer-coated ZnO NP in MALDI MSI of small molecules.

ZnO NP-assisted LDI MSI was successfully applied in direct distribution visualization and relative quantitation of neurotransmitters such as GABA and glutamate between the drug-treated versus vehicle-treated animals in multiple various brain regions at once in this work. It allows the evaluation of their relative abundance changes from the drug treatment and

the investigation of biomarkers. Chronic adolescent drug exposure to nicotine and THC, respectively, has been shown to alter the total GABA and glutamate levels in multiple brain regions in both adolescent and adult rat brains, indicating chronic drug exposure during adolescence affects the adolescent brains in the short term and the adult brains in the long term differently. The examinations of well-defined regions, such as the prelimbic cortex (PrL) and infralimbic cortex (IL), the sub-regions of the prefrontal cortex (PFC), the nucleus accumbens core (NAcSh) and nucleus accumbens shell (NAcSh), the sub-regions of the nucleus accumbens (NAc), and the dorsal subiculum (DS) and ventral subiculum (VS), the sub-regions of the hippocampus (HPC), enable us to investigate the functional differences of those sub-regions in the brain. Moreover, MSI offers an excellent opportunity to directly compare the results from animal models to clinical results using magnetic resonance spectroscopy (MRS).

Regardless, the investigation of the drug effect was limited to GABA and glutamate in specific brain regions such as the prefrontal cortex, nucleus accumbens, and hippocampus. Since MSI offers the possibility of further analysis of the stored data to extract more information, more brain regions and molecules can be investigated to have a comprehensive examination of drugs on brain development in the future. In addition, the detection of dopamine requires further identification, ideally by MSI conducted on an instrument with high mass resolving power to acquire the accurate m/z for molecule identification while preserving the spatial distribution information at the same time.

Some important neurotransmitters like serotonin remain undetectable because of their low abundances, the suppression of other molecules in the brain tissues, and the detection sensitivity offered by ZnO NP. Derivatization targeting specific functional groups has been shown to improve the detection sensitivity of the target analytes from the generation of derivatized molecules with permanent charges [9, 10]. Recently, methylated 4-(anthracen-9-yl)-2-fluoro-1-alkylpyridin-1-ium (FMP-10) has successfully derivatized molecules containing primary or secondary amine and phenolic hydroxyl groups with permanent charges in the rodent brains [11]. The improvements in the ionization sensitivity allowed the detection and imaging of serotonin and other primary or secondary amine-containing and phenolic hydroxyl-containing compounds. However, primary neurotransmitters such as glutamate and molecules without those specific functional groups are undetectable. The applications of FMP-10 and ZnO NP could provide complementary and comprehensive information on brain neurotransmitters. Furthermore, it is promising to apply a hybrid matrix containing ZnO NP and FMP-10 to image a wider range of neurotransmitters in one experiment.

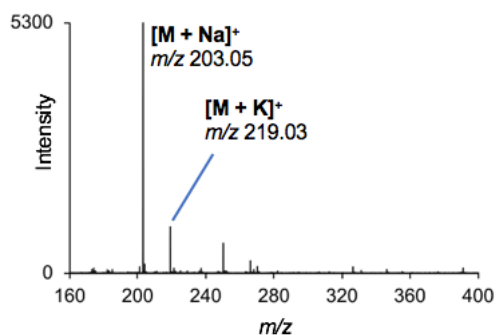
5.2 References

- (1) Yagnik, G. B.; Hansen, R. L.; Korte, A. R.; Reichert, M. D.; Vela, J.; Lee, Y. J. *Analytical Chemistry* **2016**, *88*, 8926-8930.
- (2) Wu, Q.; Chu, J. L.; Rubakhin, S. S.; Gillette, M. U.; Sweedler, J. V. *Chemical Science* **2017**, *8*, 3926-3938.
- (3) Liang, Q.; Sherwood, J.; Macher, T.; Wilson, J. M.; Bao, Y.; Cassady, C. J. *Journal of The American Society for Mass Spectrometry* **2016**, *28*, 409-418.
- (4) Watanabe, T.; Okumura, K.; Kawasaki, H.; Arakawa, R. *Journal of Mass Spectrometry* **2009**, *44*, 1443-1451.
- (5) Kwon, D.; Park, J.; Park, J.; Choi, S. Y.; Yoon, T. H. *International journal of nanomedicine* **2014**, *9*, 57-65.
- (6) Guo, L.; Yang, S.; Yang, C.; Yu, P.; Wang, J.; Ge, W.; Wong, G. K. *Chemistry of Materials* **2000**, *12*, 2268-2274.
- (7) Tang, E.; Cheng, G.; Ma, X.; Pang, X.; Zhao, Q. *Applied Surface Science* **2006**, *252*, 5227-5232.
- (8) Tachikawa, S.; Noguchi, A.; Tsuge, T.; Hara, M.; Odawara, O.; Wada, H. *Materials* **2011**, *4*, 1132-1143.
- (9) Shariatgorji, M.; Nilsson, A.; Goodwin, R. J. A.; Kallback, P.; Schintu, N.; Zhang, X. Q.; Crossman, A. R.; Bezard, E.; Svenningsson, P.; Andren, P. E. *Neuron* **2014**, *84*, 697-707.
- (10) Manier, M. L.; Spraggins, J. M.; Reyzer, M. L.; Norris, J. L.; Caprioli, R. M. *Journal of Mass Spectrometry* **2014**, *49*, 665-673.

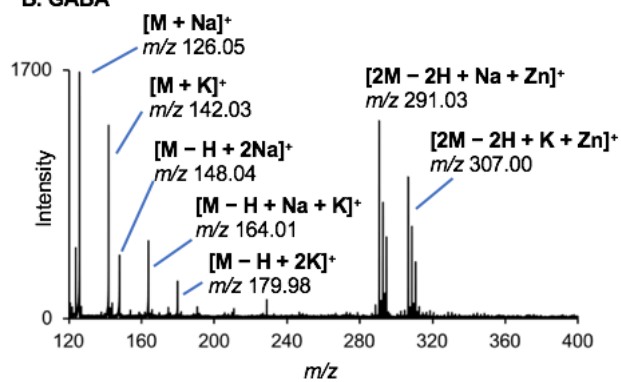
(11) Shariatgorji, M.; Nilsson, A.; Fridjonsdottir, E.; Vallianatou, T.; Kallback, P.; Katan, L.; Savmarker, J.; Mantas, I.; Zhang, X. Q.; Bezard, E.; Svenningsson, P.; Odell, L. R.; Andren, P. E. *Nature Methods* **2019**, *16*, 1021-1028.

Appendix I – Chapter 2 Supplementary

A. Myo-inositol



B. GABA



C. Palmitic acid

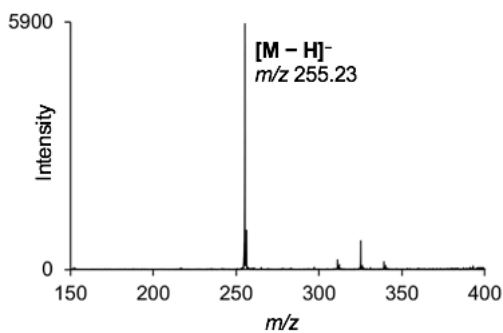


Figure 1. ZnO NP-assisted LDI mass spectra of standards: 30 ng of (A) myo-inositol and (B) GABA in the positive ion mode and (C) 300 ng of palmitic acid in the negative ion mode.

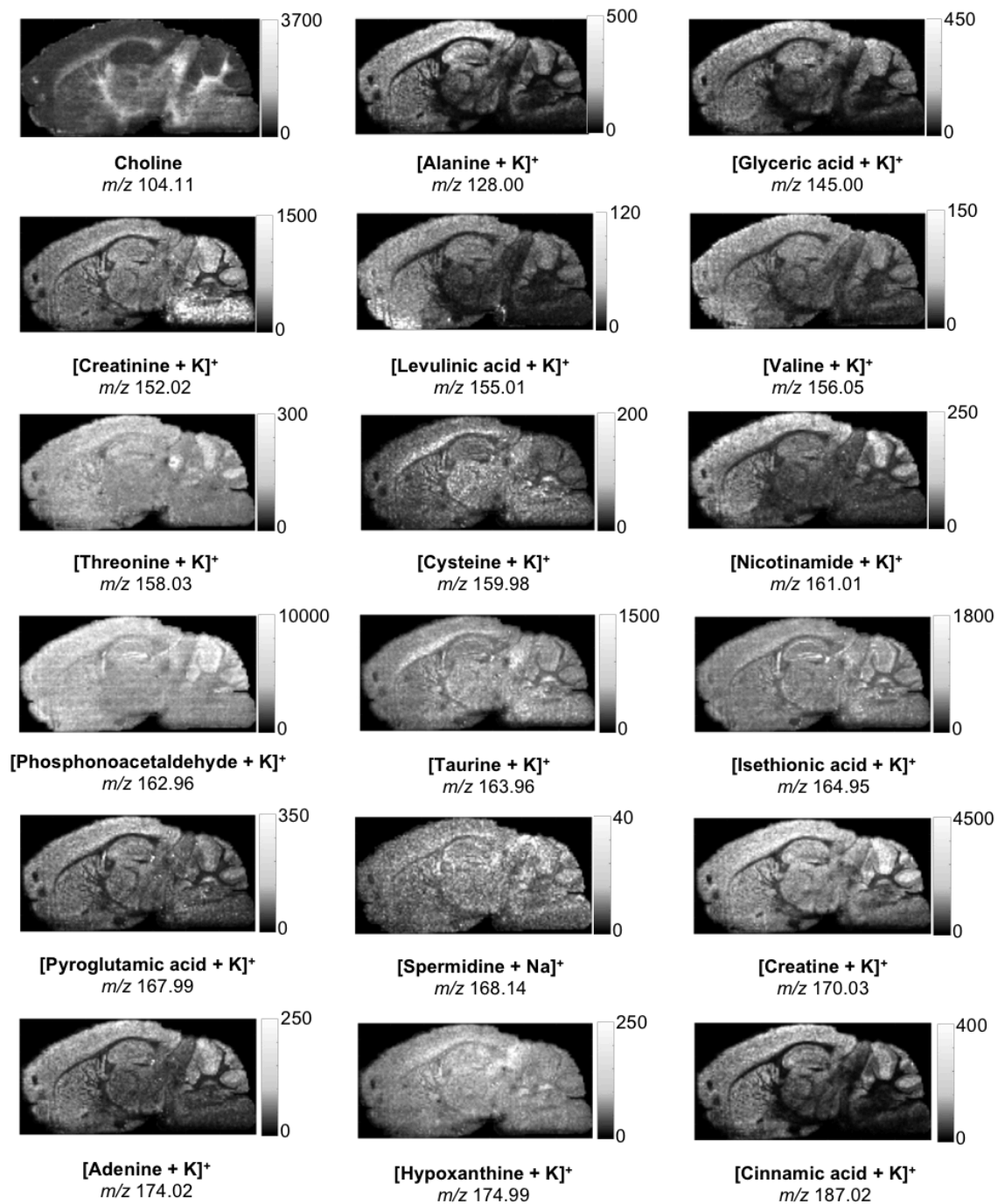
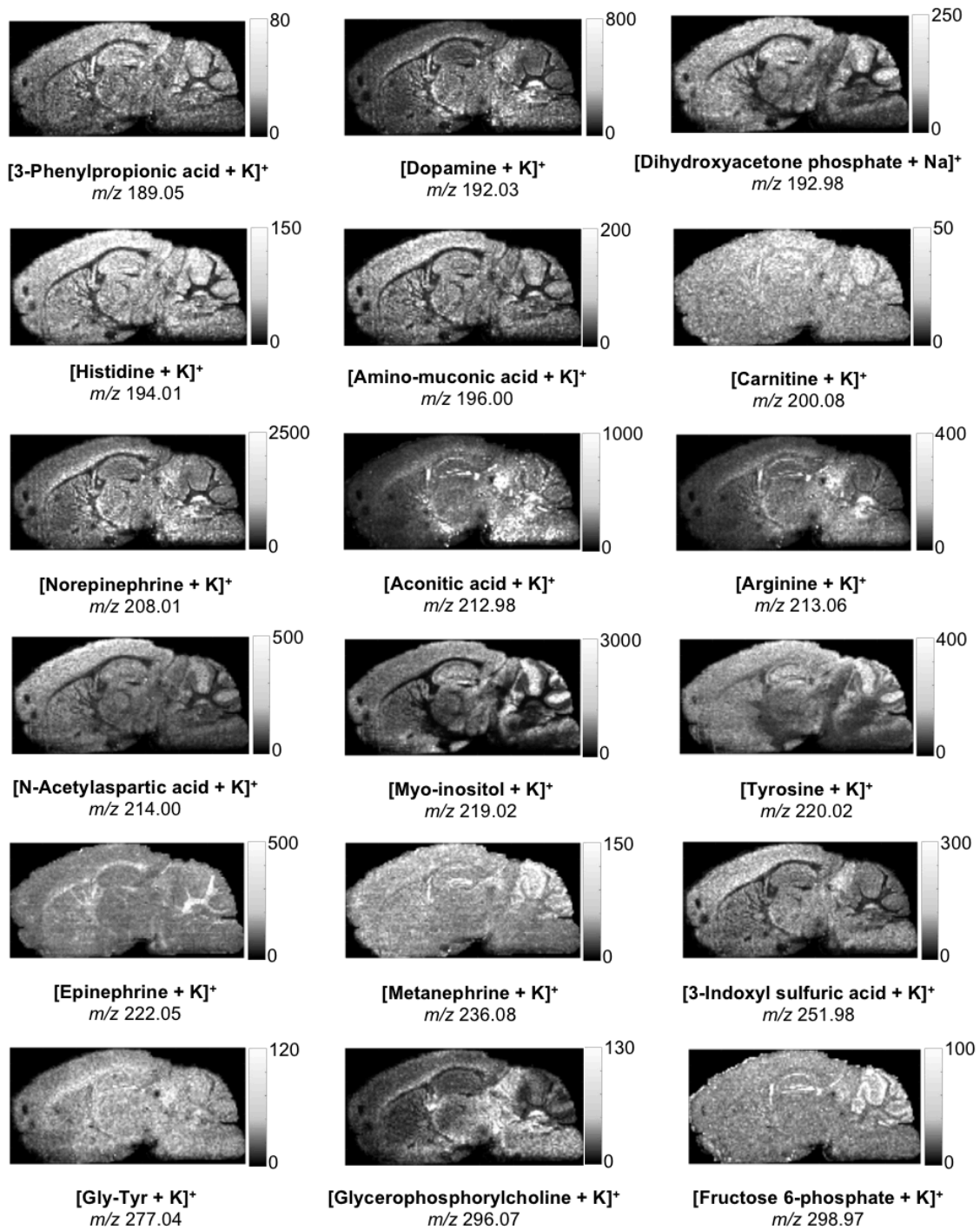
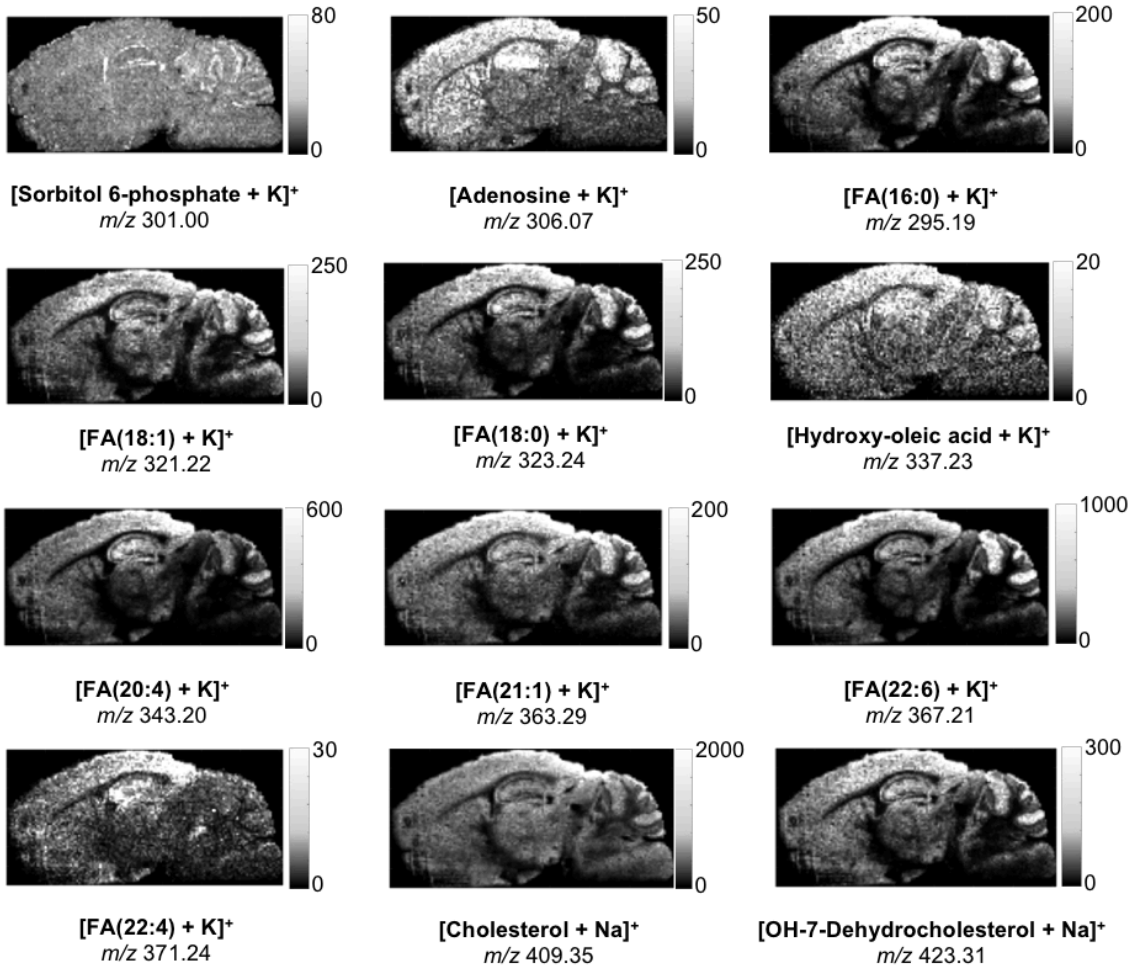


Figure 2. Ion images of the sagittal section of a mouse brain acquired with ZnO NP-assisted LDI MSI at a raster size of 70 μm in the positive ion mode (figure continued on next page).



(figure continued on next page)



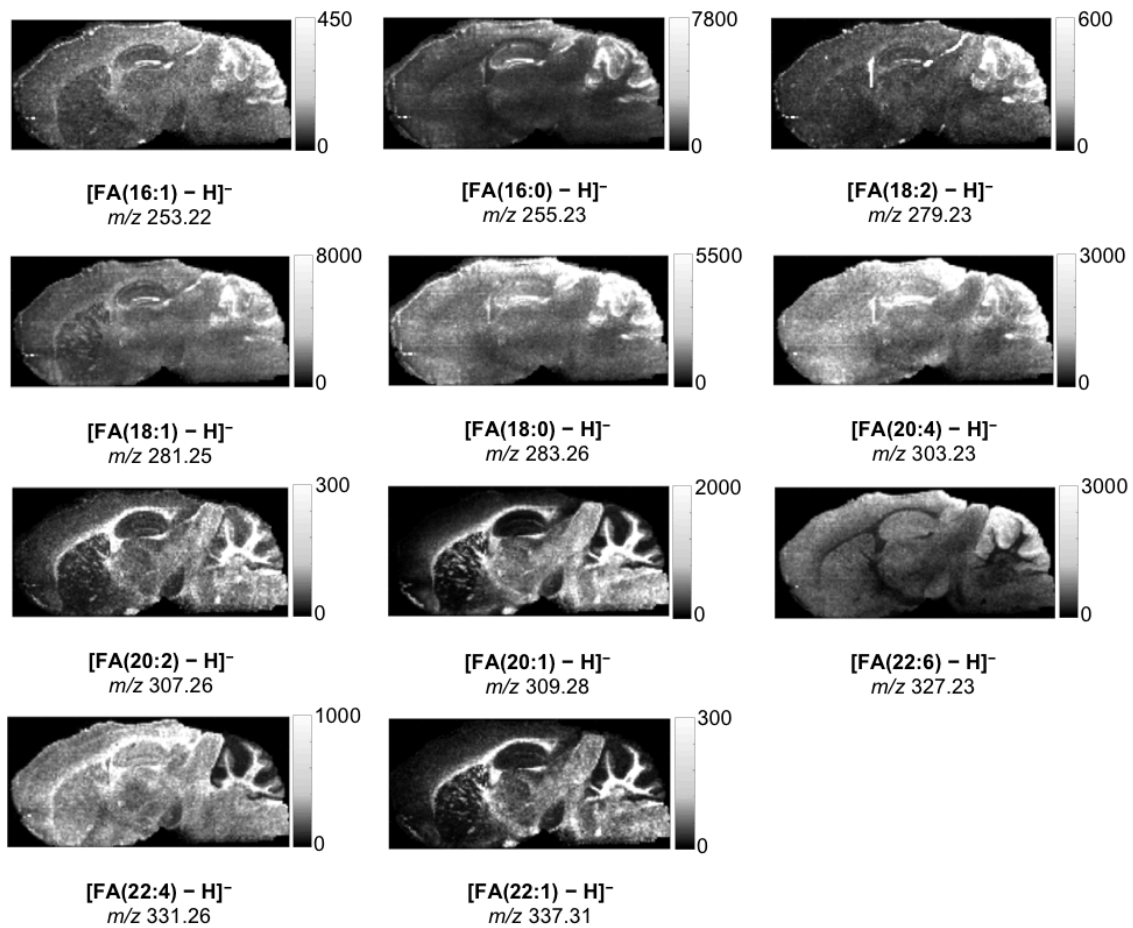


Figure 3. Ion images of the sagittal section of a mouse brain acquired with ZnO NP-assisted LDI MSI at a raster size of 70 μm in the negative ion mode.

Table 1. A List of the Small Molecules Detected in Mouse Brain Tissues by LDI MSI with TiO₂ NP or Dopamine-modified TiO₂ Monolith.

<i>m/z</i>	compound	detected ions			classification
		TiO ₂ in this work	TiO ₂ [1]	dopamine-modified TiO ₂ [2]	
99.00	glycine	[M + Na] ⁺			amino acids
113.97		[M + K] ⁺			
122.03	cysteine		[M + H] ⁺		amino acids
127.98	alanine	[M + K] ⁺			amino acids
133.08	ornithine		[M + H] ⁺		amino acids
134.05	aspartic acid		[M + H] ⁺		amino acids
172.01		[M + K] ⁺			
132.07	creatine		[M + H] ⁺		amino acids
170.03		[M + K] ⁺			
170.03				[M + K] ⁺	
143.99	serine	[M + K] ⁺			amino acids
154.00	proline	[M + K] ⁺			amino acids
154.02				[M + K] ⁺	
156.02	valine	[M + K] ⁺			amino acids
120.06	threonine		[M + H] ⁺		amino acids
158.01		[M + K] ⁺			
166.08	phenylalanine		[M + H] ⁺		amino acids
167.01	2-amino-4-cyano-butanoic acid	[M + K] ⁺			amino acids
167.02				[M + K] ⁺	
168.00	pyroglutamic acid	[M + K] ⁺			amino acids
168.01				[M + K] ⁺	
169.04	glutamine	[M + Na] ⁺			amino acids
169.06				[M + Na] ⁺	
185.02		[M + K] ⁺			
148.06	glutamic acid		[M + H] ⁺		amino acids
186.00		[M + K] ⁺			
186.02				[M+K] ⁺	
150.06	methionine		[M + H] ⁺		amino acids
188.00		[M + K] ⁺			
194.02	histidine	[M + K] ⁺			amino acids
196.00	amino-muconic acid			[M + K] ⁺	amino acids
196.01		[M + K] ⁺			
198.09	amino-octanoic acid			[M + K] ⁺	amino acids
204.03	phenylalanine	[M + K] ⁺			amino acids
175.11	arginine		[M + H] ⁺		amino acids
213.06		[M + K] ⁺			
234.07	methoxytyrosine			[M + Na] ⁺	amino acids
89.10	putrescine		[M + H] ⁺		alkaloids
111.09		[M + Na] ⁺			
123.06	nicotinamide		[M + H] ⁺		alkaloids
160.99		[M + K] ⁺			
168.13	spermidine	[M + Na] ⁺			alkaloids
184.09		[M + K] ⁺			
180.04	arecaidine			[M + K] ⁺	alkaloids
241.17	spermine	[M + K] ⁺			alkaloids
136.06	adenine		[M + H] ⁺		purine
174.01		[M + K] ⁺			
137.05	hypoxanthine		[M + H] ⁺		purine
159.00		[M + Na] ⁺			
174.98		[M + K] ⁺			
113.03	uracil		[M + H] ⁺		pyrimidine
150.96		[M + K] ⁺			

(table continued on next page)

m/z	compound	detected ions			classification
		TiO ₂ in this work	TiO ₂ [1]	dopamine-modified TiO ₂ [2]	
104.06	γ-aminobutyric acid (GABA)		[M + H] ⁺		neurotransmitters
126.02		[M + Na] ⁺			
142.00		[M + K] ⁺			
142.03				[M + K] ⁺	
191.03	dopamine	[M + K] ⁺			neurotransmitters
208.02	norepinephrine	[M + K] ⁺			neurotransmitters
222.05	epinephrine	[M + K] ⁺			neurotransmitters
306.06	adenosine	[M + K] ⁺			neurotransmitters
409.34	cholesterol			[M + Na] ⁺	sterol lipids
409.36		[M + Na] ⁺		[M + K] ⁺	
425.32					
425.34		[M + K] ⁺			
429.24	hydroxy-oxo-cholan-oic acid			[M + K] ⁺	sterol lipids
439.30	OH-7-dehydrocholesterol			[M + K] ⁺	sterol lipids
439.31		[M + K] ⁺			
465.33	cholesta-6,8(14)-dien-3β,5α-diol			[M + K] ⁺	sterol lipids
243.08	Met-Ala	[M + Na] ⁺			dipeptides
259.05				[M + K] ⁺	
277.06	Gly-Tyr			[M + Na] ⁺	dipeptides
283.07	Pro-Glu			[M + K] ⁺	dipeptides
413.12	Cys Gly Pro Val			[M + K] ⁺	peptides
453.17	Gly Glu Pro Ile			[M + K] ⁺	peptides
457.21	Met Leu Ala Thr			[M + Na] ⁺	peptides
459.22	Thr Leu Gly Phe			[M + Na] ⁺	peptides
469.15	Glu Trp Pro			[M + K] ⁺	peptides
481.21	Asp Val Leu Pro			[M + K] ⁺	peptides
495.16	Gly Phe Ala Tyr			[M + K] ⁺	peptides
497.18	Asn Asn Pro Met			[M + Na] ⁺	peptides
126.99	butyric acid	[M + K] ⁺			fatty acids
168.98	5-oxohexanoic acid	[M + K] ⁺			fatty acids
277.18	FA(16:1)	[M + Na] ⁺			fatty acids
293.19				[M + K] ⁺	
279.23	FA(16:0)			[M + Na] ⁺	fatty acids
295.20				[M + K] ⁺	
305.24	FA(18:1)			[M + Na] ⁺	fatty acids
321.23		[M + K] ⁺			
307.26	FA(18:0)			[M + Na] ⁺	fatty acids
323.23		[M + K] ⁺			
323.23				[M + K] ⁺	
327.23	FA(20:4)			[M + Na] ⁺	fatty acids
343.20				[M + K] ⁺	
343.21		[M + K] ⁺			
337.21	hydroxy-oleic acid			[M + K] ⁺	fatty acids
341.19	FA(20:5)			[M + K] ⁺	fatty acids
351.22	FA(22:6)	[M + Na] ⁺			fatty acids
351.23				[M + Na] ⁺	
367.20				[M + K] ⁺	
367.21		[M + K] ⁺			
355.26	docosatetraenoic acid (22:4)			[M + Na] ⁺	fatty acids
363.27	FA(21:1)			[M + K] ⁺	fatty acids

(table continued on next page)

m/z	compound	detected ions			classification
		TiO ₂ in this work	TiO ₂ [1]	dopamine-modified TiO ₂ [2]	
139.00	fumaric acid	[M + Na] ⁺			organic acids
144.98	glyceric acid	[M + K] ⁺			organic acids
153.00	citraconic acid	[M + Na] ⁺			organic acids
154.99	levulinic acid	[M + K] ⁺			organic acids
156.98	succinic acid	[M + K] ⁺			organic acids
159.00	threonic acid	[M + Na] ⁺			organic acids
187.01	cinnamic acid	[M + K] ⁺			organic acids
189.03	3-phenylpropionic acid	[M + K] ⁺			organic acids
212.97	aconitic acid	[M + K] ⁺			organic acids
217.02	glucuronic acid	[M + Na] ⁺			organic acids
104.09	choline	M ⁺			others
110.03	hypotaurine		[M + H] ⁺		others
112.01	oxamic acid	[M + Na] ⁺			others
112.06	cytosine		[M + H] ⁺		others
150.00		[M + K] ⁺			
130.08	pipecolic acid		[M + H] ⁺		others
136.04	creatinine			[M + Na] ⁺	others
152.01		[M + K] ⁺			
152.02				[M + K] ⁺	
139.08	aminopentanamide			[M+Na] ⁺	others
143.08	ectoine		[M + H] ⁺		others
146.98	phosphono-	[M + Na] ⁺			others
162.96	acetaldehyde	[M + K] ⁺			
164.07	S-methylmethionine		M ⁺		others
165.04	lumazine		[M + H] ⁺		others
184.07	phosphocholine		M ⁺		others
192.98	dihydroxyacetone phosphate	[M + Na] ⁺			others
203.04	myo-inositol	[M + Na] ⁺			others
219.01		[M + K] ⁺			
207.03	3-methoxy-4-	[M + Na] ⁺			others
223.01	hydroxyphenylglycol	[M + K] ⁺			
214.00	N-acetylaspartic acid	[M + K] ⁺			others
228.01	N-acetylglutamic acid	[M + K] ⁺			others
260.05	N-acetylglucosamine	[M + K] ⁺			others
266.05	cytidine	[M + Na] ⁺			others
307.05	guanosine	[M + K] ⁺			others
375.20	prostaglandin E2	[M + Na] ⁺			others
391.20		[M + K] ⁺			

Table 2. Summary of Common Neurotransmitters Detected Using MALDI MSI in the Literature and NP-assisted LDI MSI in this Work.

analyte	detection mode	derivatization	matrix	tissue type	spatial resolution	reference
adenosine	+	no	TiO ₂	mouse brain	70 μm	our work
			ZnO	mouse brain	70 μm	
				rat brain	80 μm	
alanine	+	yes	DHB	mouse brain	125 μm	[3]
		no	TiO ₂	mouse brain	70 μm	our work
			ZnO	mouse brain	70 μm	
aspartate	+	yes	DHB	mouse brain	125 μm	[3]
		no	TiO ₂	mouse brain	70 μm	[1]
			ZnO	mouse brain	70 μm	our work
			TiO ₂			
	-	no	9-AA	mouse brain	50 μm	[4]
		no	NEDC	mouse brain	100 μm	[5]
		no	PNA	rat brain	200 μm	[6]
		no	BNDM	rat brain	100 μm	[7]
cysteine	+	no	TiO ₂	mouse brain	70 μm	[1]
		no	ZnO	mouse brain	70 μm	our work
epinephrine	+	yes	CHCA	pig adrenal gland	200 μm	[8]
		yes	FMP-10	rat brain	80 μm	[9]
		no	TiO ₂ ZnO	mouse brain rat brain	70 μm 80 μm	our work
GABA	+	yes	DHB	mouse brain	125 μm	[3]
		yes	CHCA	rat brain	100 μm	[10]
		yes	CHCA	rat brain pig adrenal gland	50 μm 200 μm	[8]
		yes	TPP	rat brain	120 μm	[11]
		yes	FMP-10	rat brain	80 μm 100 μm	[9]
		no	TiO ₂	mouse brain	70 μm	[1]
		no	TiO ₂ ZnO	mouse brain mouse brain rat brain	70 μm 70 μm 80 μm	our work
		no	modified-TiO ₂	mouse brain	30 μm	[2]

(table continued on next page)

analyte	detection mode	derivatization	matrix	tissue type	spatial resolution	reference
glutamate	+	yes	DHB	mouse brain	125 μm	[3]
		yes	CHCA	brain	-	[10]
		yes	CHCA	rat brain	50 μm	[8]
		no	TiO ₂	mouse brain	70 μm	[1]
		no	TiO ₂ ZnO	mouse brain mouse brain rat brain	70 μm 70 μm 80 μm	our work
		no	modified-TiO ₂	mouse brain	30 μm	[2]
		no	9-AA	mouse brain	50 μm	[4]
	-	no	NEDC	mouse brain	100 μm	[5]
		no	PNA	rat brain	200 μm	[6]
		no	BNDM	rat brain	100 μm	[7]
glycine	+	yes	DHB	mouse brain	125 μm	[3]
		no	ZnO TiO ₂	mouse brain	70 μm	our work
norepinephrine	+	yes	CHCA	pig adrenal gland	200 μm	[8]
		yes	FMP-10	rat brain	80 μm	[9]
		no	TiO ₂ ZnO TiO ₂	mouse brain mouse brain rat brain	70 μm 70 μm 80 μm	our work
		yes	DHB	mouse brain	125 μm	[3]
serine	+	no	TiO ₂	mouse brain	70 μm	[1]
		no	TiO ₂ ZnO	mouse brain mouse brain Rat brain	70 μm 70 μm 80 μm	our work
		yes	DHB	mouse brain	125 μm	[3]
taurine	+	yes	DHB	mouse brain	125 μm	[3]
		yes	TPP	rat brain	120 μm	[11]
		no	ZnO	mouse brain rat brain	70 μm 80 μm	our work
	-	no	NEDC	mouse kidney	50 μm	[5]
		no	PNA	rat brain	200 μm	[6]

(table continued on next page)

analyte	detection mode	derivatization	matrix	tissue type	spatial resolution	reference
acetylcholine	+	yes	CHCA	rat brain mouse brain	15 μm 100 μm	[10]
dopamine	+	yes	DHB	mouse brain	125 μm	[3]
		yes	CHCA	rat brain	100 μm	[10]
		yes	CHCA	pig adrenal gland	200 μm	[8]
		yes	TPP	rat brain	120 μm	[11]
		yes	FMP-10	rat brain	20 μm 50 μm 80 μm 100 μm	[9]
		no	TiO ₂ ZnO	mouse brain mouse brain rat brain	70 μm 70 μm 80 μm	our work
serotonin	+	yes	CHCA	-	-	[10]
		yes	FMP-10	rat brain	20 μm 50 μm 80 μm 100 μm	[9]
tyramine	+	yes	CHCA	brain	-	[10]
tryptamine	+	yes	CHCA	brain	-	[10]

Reference

- (1) Shrivastava, K.; Hayasaka, T.; Sugiura, Y.; Setou, M. *Analytical Chemistry* **2011**, *83*, 7283-7289.
- (2) Wu, Q.; Chu, J. L.; Rubakhin, S. S.; Gillette, M. U.; Sweedler, J. V. *Chemical Science* **2017**, *8*, 3926-3938.
- (3) Esteve, C.; Tolner, E. A.; Shyti, R.; van den Maagdenberg, A.; McDonnell, L. A. *Metabolomics* **2016**, *12*, 9.
- (4) Miura, D.; Fujimura, Y.; Yamato, M.; Hyodo, F.; Utsumi, H.; Tachibana, H.; Wariishi, H. *Analytical Chemistry* **2010**, *82*, 9789-9796.
- (5) Wang, J. N.; Qiu, S. L.; Chen, S. M.; Xiong, C. Q.; Liu, H. H.; Wang, J. Y.; Zhang, N.; Hou, J.; He, Q.; Nie, Z. X. *Analytical Chemistry* **2015**, *87*, 422-430.
- (6) Liu, H. H.; Zhou, Y. M.; Wang, J. Y.; Xiong, C. Q.; Xue, J. J.; Zhan, L. P.; Nie, Z. X. *Analytical Chemistry* **2018**, *90*, 729-736.
- (7) Sun, C. L.; Liu, W.; Mu, Y.; Wang, X. *Talanta* **2020**, *209*, 9.
- (8) Manier, M. L.; Spraggins, J. M.; Reyzer, M. L.; Norris, J. L.; Caprioli, R. M. *Journal of Mass Spectrometry* **2014**, *49*, 665-673.
- (9) Shariatgorji, M.; Nilsson, A.; Fridjonsdottir, E.; Vallianatou, T.; Kallback, P.; Katan, L.; Savmarker, J.; Mantas, I.; Zhang, X. Q.; Bezard, E.; Svenningsson, P.; Odell, L. R.; Andren, P. E. *Nature Methods* **2019**, *16*, 1021-1028.
- (10) Shariatgorji, M.; Nilsson, A.; Goodwin, R. J. A.; Kallback, P.; Schintu, N.; Zhang, X. Q.; Crossman, A. R.; Bezard, E.; Svenningsson, P.; Andren, P. E. *Neuron* **2014**, *84*, 697-707.

(11) Shariatgorji, R.; Nilsson, A.; Strittmatter, N.; Vallianatou, T.; Zhang, X.; Svenningsson, P.; Goodwin, R. J. A.; Andren, P. E. *Journal of the American Society for Mass Spectrometry* **2020**.

Appendix II – Copyright Permission



Imaging of Neurotransmitters and Small Molecules in Brain Tissues Using Laser Desorption/Ionization Mass Spectrometry Assisted with Zinc Oxide Nanoparticles

Author: Chaochao Chen, Steven R. Laviolette, Shawn N. Whitehead, et al

Publication: Journal of the American Society for Mass Spectrometry

Publisher: American Chemical Society

Date: Apr 1, 2021

Copyright © 2021, American Society for Mass Spectrometry. Published by the American Chemical Society. All rights reserved.

PERMISSION/LICENSE IS GRANTED FOR YOUR ORDER AT NO CHARGE

This type of permission/license, instead of the standard Terms and Conditions, is sent to you because no fee is being charged for your order. Please note the following:

- Permission is granted for your request in both print and electronic formats, and translations.
- If figures and/or tables were requested, they may be adapted or used in part.
- Please print this page for your records and send a copy of it to your publisher/graduate school.
- Appropriate credit for the requested material should be given as follows: "Reprinted (adapted) with permission from {COMPLETE REFERENCE CITATION}. Copyright {YEAR} American Chemical Society." Insert appropriate information in place of the capitalized words.
- One-time permission is granted only for the use specified in your RightsLink request. No additional uses are granted (such as derivative works or other editions). For any uses, please submit a new request.

If credit is given to another source for the material you requested from RightsLink, permission must be obtained from that source.

[BACK](#)

[CLOSE WINDOW](#)

Curriculum Vitae

Education

Ph.D., Physical & Analytical Chemistry 09/2015-present
Western University, London, Canada
Supervisor: Dr. Ken Yeung

Research focus:

- ❖ Adapted and developed methods using inorganic matrices to assist laser desorption ionization mass spectrometry imaging (LDI MSI) of small molecules in rodent brains.
- ❖ Applied quantitative LDI MSI using inorganic matrices in neurobiology studies.

B.Sc., Applied Chemistry 09/2011-06/2015
Northeastern University, Shenyang, China

Research Experience

Graduate Research Assistant 09/2015-04/2021
Western University, London, Canada

- ❖ Developed methods for untargeted analysis of small molecules in tissues with LDI MSI.
- ❖ Applied quantitative MALDI MSI in collaborative neurobiology projects.
- ❖ Established standard operating procedures in sample preparations.
- ❖ Performed/facilitated troubleshooting and maintenance of laboratory equipment.
- ❖ Provided training on laboratory equipment and technical support to new colleagues.

Research Assistant 03/2013-05/2015
Northeastern University, Shenyang, China

- ❖ Facilitated in the construction of detection device.
- ❖ Applied column gel electrophoresis for online separation and detection of cations.

Work Experience

Undergraduate Laboratory Assistant 09/2021-present
Department of Chemistry, Western University, London, Canada

- ❖ Supervise laboratory sessions: provide technical assistance to TAs and undergraduates, maintain equipment and stocks, and deal with accidents and emergencies.

Graduate Teaching Assistant 09/2015-12/2020
Department of Chemistry, Western University, London, Canada

Organic Chemistry for Life Sciences & Organic Chemistry of Biological Molecules

- ❖ Presented pre-laboratory instructional talks on laboratory techniques and theories.
- ❖ Facilitated laboratory experiments and answered questions related to lab materials.
- ❖ Performed regular assessments to provide constructive feedback for students.

Intern 07/2014
Liaoning Disease Prevention and Control Center, Shenyang, China

- ❖ Carried out sample preparation, analysis, and reporting following the established protocols.

Volunteer Experience

Conference Volunteer 06/2019
102nd Canadian Chemistry Conference and Exhibition, Quebec City, Canada

- ❖ Facilitated oral presentation sessions to ensure they were in an organized manner.
- ❖ Managed the speaker ready room and provided technical support.

Science Rendezvous Event Volunteer 05/2018 & 05/2019
Western University, London, Canada

- ❖ Demonstrated scientific principles during the event where members of the public visit Western University and experience hands-on chemistry experiments.

Outreach Event Volunteer 04/2017-07/2018
Department of Chemistry, Western University, London, Canada

- ❖ Participated as a lab demonstrator during outreach events where participants engage in fun and educational experiments.

Publications

Chaochao Chen, Steven R. Laviolette, Shawn N. Whitehead, Justin B. Renaud, and Ken K.-C. Yeung. Imaging of Neurotransmitters and Small Molecules in Brain Tissues Using Laser Desorption/Ionization Mass Spectrometry Assisted with Zinc Oxide Nanoparticles. *Journal of the American Society for Mass Spectrometry* **2021**, 32 (4), 1065-1079.

Presentations

Marta De Felice, **Chaochao Chen**, Mar Rodríguez-Ruiz, Hanna J. Szkudlarek, Michael Lam, Selvi Sert, Shawn N. Whitehead, Ken K.-C. Yeung, Walter J. Rushlow, Steven R. Laviolette. Adolescent Δ -9-Tetrahydrocannabinol Exposure Induces Different Long-lasting Changes in the Dorsal and Ventral Portions of the Hippocampal Formation. *Annual Society of Neuroscience Conference* (November 2021). Poster.

Marta De Felice, Tya Vine, Roger M. Hudson, Mar Rodríguez-Ruiz, **Chaochao Chen**, Michael Lam, Shawn N. Whitehead, Ken K.-C. Yeung, Walter J. Rushlow, Steven R. Laviolette. Effects of Hippocampal Dysregulation on the Hyper-dopaminergic State Induced by Chronic Adolescent THC exposure. *Annual Society of Neuroscience Conference* (Chicago, USA, October 2019). Poster.

Chaochao Chen, Marta De Felice, Steven R. Laviolette, and Ken K.-C. Yeung. Relative Quantitation of Neurotransmitters in Brains from Adult Rats Subjected to Adolescent Tetrahydrocannabinol Exposure by MALDI Mass Spectrometry Imaging. *102nd Canadian Chemistry Conference and Exhibition* (Quebec City, Canada, June 2019). Poster.

Ken K.-C. Yeung and **Chaochao Chen**. Comprehensive Evaluation of Zinc Oxide Nanoparticles as Matrix for MALDI MS Tissue Imaging of Metabolites. *67th Annual American Society for Mass Spectrometry Conference* (Atlanta, USA, June 2019). Poster.

Chaochao Chen and Ken K.-C. Yeung. ZnO Nanoparticle-assisted Laser Desorption Ionization Mass Spectrometry Imaging for Small Molecules. *65th Annual American Society for Mass Spectrometry Conference* (Indianapolis, USA, June 2017). Poster.

Course Work

9522 Analytical Separations 81

9472 Advanced Analytical Chemistry 87

9544 Mass Spectrometry 93

9494 Biophysical Chemistry 93